REALISTIC MODELS FOR THEORETICAL STUDIES OF HETEROGENEOUS CATALYSIS

by

Eric D. Hermes

A dissertation submitted in partial fulfillment of
the requirements for the degree of

Doctor of Philosophy

(Chemistry)

at the

UNIVERSITY OF WISCONSIN–MADISON

2018

Date of final oral examination: 01/18/18

The dissertation is approved by the following members of the Final Oral Committee:

J.R. Schmidt, Associate Professor, Chemistry
Shannon Stahl, Professor, Chemistry
Manos Mavrikakis, Professor, Chemical and Biological Engineering
Dane Morgan, Professor, Materials Science and Engineering

ACKNOWLEDGMENTS

The work presented in this dissertation was made possible by financial support from the National Science Foundation through the Chemical Catalysis program under grant number CHE-1362136. The computational resources used in this work were provided by the University of Wisconsin – Madison Department of Chemistry, the UW–Madison Center for High-Throughput Computing (CHTC) through the Department of Computer Sciences, and the Extreme Science and Engineering Discovery Environment (XSEDE) through grant number TG-CHE120088.

I must first thank the Schmidt group members who joined before me for their guidance and mentorship. Dr. Kuang Yu has an excellent ability to present complex ideas in an understandable way, and he taught me a lot about his research and interesting new developments from the literature. I relied heavily on Professor Jesse McDaniel's keen chemical and physical intuition; it seemed as though Jesse could answer any question I could possibly come up with regarding physical chemistry. In addition to providing the foundations of my first research project in the group, Dr. Jeff Christianson was always willing to answer the many, many questions I had about programming, running calculations, and other topics on which I was clueless when I first began. Dr. Benjamin Dunnington took the time to painstakingly explain the principles of plane wave DFT, pseudopotentials, and various tricks for getting troublesome calculations to converge properly, and he spent the last few months of graduate school assisting me with one of my projects, for which I am very grateful. Dr. Glen Jenness taught me many things about programming, particularly in Python, and introduced me to ASE, a project to which I am now an active contributor.

The students who joined the group after me also deserve recognition. Dr. Mary Van Vleet has a lot of skill at organizing and presenting data in clear and understandable figures, and so I often relied on her advice when making figures for presentations or publications. I frequently asked Tingting Weng for her opinion on material I had written to ensure that I was presenting ideas in an understandable way, and the baked goods she occasionally brought into the office were always delicious. Dr. Chenyang Zhang helped me test and extend many of the tools I had developed for running and managing

calculations, and he was always willing to walk me through issues in great detail in order to figure out how to fix the problems we had with our computational resources. Aurora Janes continues to provide an immense amount of help in my own research, contributing extensively to the microkinetic modeling projects that I have focused on for the last part of my tenure as a graduate student. Though sometimes our conversations veer sharply off topic, Xinyi Li has always has interesting, insightful questions about thermodynamics and statistical mechanics, and I always enjoy the conversations we have. Tesia Janicki has become somewhat of a coordinator for group activities, and has taken on some of my responsibilities as my time with the group began to wind down. Dr. Nina Tyminska gave me advice when it came time to look for positions after graduate school, and I greatly appreciate the help she provided by sharing postdoc openings and other opportunities with me. We haven't been in the group together for that long, but I appreciate Kai Cui listening to me ramble about my research and the research of other group members when he was deciding on which group to join.

More than any other person, I must thank my advisor, Professor J.R. Schmidt. J.R. has been far and away the most valuable resource during my time in graduate school, answering every question I had spanning many different topics. I can't think of another person with such a broad range of expertise spanning all levels of physical chemistry, from electronic structure theory and statistical mechanics to spectroscopy and catalysis. In addition to providing guidance on the several research projects I was involved with, J.R. also allowed me the freedom to try my own ideas, and go down the paths which I thought were interesting and promising. Even though my ideas didn't always work, J.R. accepted my failures and helped guide me back onto the path to becoming a successful researcher. Needless to say, none of the things I have accomplished as a graduate student would have been possible without J.R.'s mentorship.

I also want to thank my committee for sharing their valuable input during my time as a graduate student. Though he is no longer on my committee due, the advice Professor Qiang Cui provided for my research was always very helpful, and I owe my current understanding of statistical mechanics to his teaching. For a long time, Professor Shannon Stahl was my one connection with "real" chemistry, and he helped keep me focused on the properties of real systems without getting bogged down in the details of simplified

computational models. Professor Manos Mavrikakis provided me with the information and motivation necessary to create my own microkinetic modeling code, Micki, and I have relied extensively on his publications for testing and developing this code. I am grateful for Professor Dane Morgan agreeing to join my committee, and I wish there had been more opportunities for discussion and collaboration through the ICG. Though he is not officially on my committee, my collaborations with Professor Song Jin provided me with the opportunity to extend my knowledge of electrochemistry, leading to new ideas for applying microkinetic modeling to electrocatalytic systems.

I must also thank my parents, Robb and Deb, for providing support over these six and a half years of graduate school. My brother Matt and I spent many holiday breaks together talking about science, and the information he shared about his experiences in graduate school helped provide context for the experiences I went though. I will not attempt to list the friends I made in graduate school for fear of accidental omission, but these friends helped me maintain my sanity through evening and weekend get-togethers. Eating dinner together, playing card games, and watching movies were a great escape from the occasionally very stressful life as a graduate student, and I am deeply grateful of everyone who made my life a little bit better.

CONTENTS

LIST OF TABLES

LIST OF FIGURES

LIST OF LISTINGS

PUBLISHED WORK AND WORK IN PREPARATION

1. Hermes, Eric D.; Jenness, Glen R.; Schmidt, J.R. Decoupling the Electronic, Geometric and Interfacial Contributions to Support Effects in Heterogeneous Catalysis. *Mol. Simul.* **2014**, 123–133.

2. Larsen, Ask H.; Mortensen, Jens J.; Blomqvist, Jakob; Castelli, Ivano E.; Christensen, Rune; Dułak, Marcin; Friis, Jesper; Groves, Michael N.; Hammer, Bjørk; Hargus, Cory; Hermes, Eric D.; Jennings, Paul C.; Jensen, Peter B.; Kermode, James; Kitchin, John R.; Kolsbjerg, Esben L.; Kubal, Joseph; Kaasbjerg, Kristen; Lysgaard, Steen; Maronsson, Jón B.; Maxson, Tristan; Olsen, Thomas; Pastewka, Lars; Peterson, Andrew; Rostgaard, Carsten; Schiøtz, Jakob; Schütt, Ole; Strange, Mikkel; Thygesen, Kristian S.; Vegge, Tejs; Vilhelmsen, Lasse; Walter, Michael; Zeng, Zhenhua; Jacobsen, Karsten W. The Atomic Simulation Environment – A Python Library for Working with Atoms. *J. Phys.: Condens. Matter.* **2017**, *29*, 273002.

3. Hermes, Eric D.; Janes, Aurora N.; Schmidt, J.R. Mechanistic Insights into Solution-Phase Oxidative Esterification of Primary Alcohols on Pd(111) from First-Principles Microkinetic Modeling. *ACS Catal.* **2018**, 272–282.

4. Yang, Xhiaohua; Hermes, Eric D.; Ying, Diwen; Li, Wenjie; Schmidt, J.R.; Jin, Song. Electrocatalytic Production of Hydrogen Peroxide by Selective Oxygen Reduction Using Earth-Abundant Cobalt Disulfide. In preparation.

5. Hermes, Eric D.; Janes, Aurora N.; Schmidt, J.R. Micki: A Microkinetic Modeling Package Written in Python. In preparation.

ABSTRACT

This thesis describes the development of a rigorous first-principles framework for microkinetic modeling and the investigation of several industrially relevant catalytic reactions using theory. First, we rigorously derive the partition function of a mean field lattice as commonly used in microkinetic modeling. We then improve upon this model through explicit consideration of lattice symmetry and the configurational degrees of freedom afforded to multidentate adsorbates. Lateral interactions are rigorously incorporated into this framework through a many-body expansion of the total lattice energy. The energetic and mass-transport effects of solvation are also incorporated into this model for the treatment of solution-phase species. A program, Micki, is developed to implement these techniques, and several examples illustrating common uses are shown.

We then investigate the role of support material in supported metal nanoparticle catalysis through comparison of Fischer–Tropsch reaction intermediate binding energies with different support materials under different conditions. Support affects catalysis through geometric perturbation of the nanoparticle, electron transfer to or from the metal, and direct participation of the support in catalysis. In another application, we develop a microkinetic model for the solution-phase esterification of 1-propanol to methyl propionate by Pd(111) to better understand the role of main group promoters. We find that the catalyst is heavily H-saturated under reaction conditions, which destabilizes all intermediates and slows the reaction considerably. Finally, we explain the observed activity of CoS_2 for the electrochemical oxygen reduction reaction by the favorable binding strength of intermediates using the computational hydrogen electrode. The observed selectivity to form H_2O_2 is explained by high barriers for O–O dissociation due to the lack of ensembles of catalyst binding sites.

1 INTRODUCTION

1.1 Heterogeneous catalysis

Scientific and technological advances in heterogeneous catalysis have been among the most important developments in history. Perhaps the most notable example is that of the Haber–Bosch process, a method for synthesizing ammonia from nitrogen gas using a heterogeneous osmium catalyst, which was developed in the early 20$^{\text{th}}$ century by Frizt Haber.[1,2] This process enabled the rapid, inexpensive production of agricultural fertilizer from non-organic sources.[3] It is thought that the Haber–Bosch process is directly responsible for the massive population growth that occurred in the early 20th century.[4] Even today, somewhere around half of all nitrogen atoms in the average human body originates from N_2 that has been reduced to ammonia through the Haber–Bosch process.[5] At the same time, this method accelerated the production of explosive weaponry, and lead to the development of new chemical weapons.[6]

While the Haber–Bosch process is perhaps an extreme example, there are many other applications of heterogeneous catalysis that illustrate its broad importance. The Fischer–Tropsch process was used in apartheid South Africa to create liquid hydrocarbons from natural gas and coal during a period in which liquid fuels were difficult to obtain due to trade embargo.[7–9] Catalytic converters, which are present in all vehicles relying on internal combustion engines for propulsion, fully converts partially-combusted hydrocarbon products to CO_2 and H_2O.[10,11] Nickel catalysts are widely used in hydrogenation reactions, such as in the hydrogenation of liquid vegetable oil to create margarine.[12] Titanium-based catalysts are commonly used in the polymerization of olefins, such as the polymerization of propylene to polypropylene.[13,14] These are just some examples of the many uses heterogeneous catalysts have in industrial applications.

In catalysis, a molecule or material participates in a chemical reaction through coordination or bonding to the reactants in such a way that the catalyst remains unchanged at the end of the reaction. Catalysts facilitate reactions without reacting themselves. For example, the catalytic converter in a vehicle strongly binds CO and oxygen atoms, thereby allowing these species to come in contact with one another and increasing the probability

of reaction to form CO_2, which then leaves the catalyst, as it only binds very weakly. This is a reaction that can and does occur in the gas phase during the combustion stage of the engine cycle, but the catalytic converter ensures that this reaction proceeds to completion by providing an alternate pathway, albeit one that does not convert chemical energy into thrust as in the internal combustion engine itself.

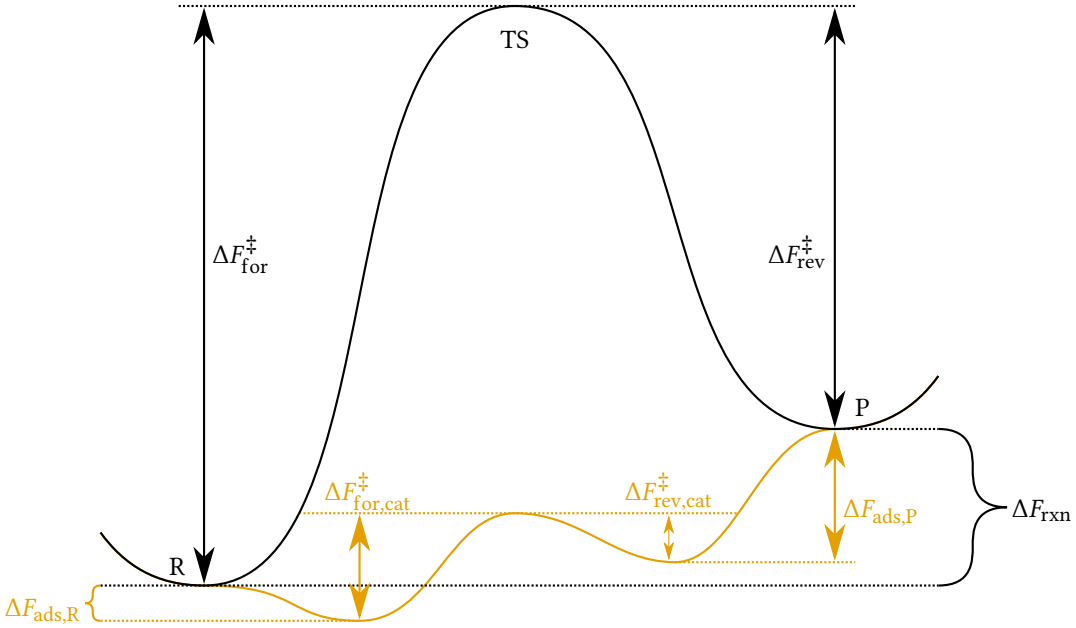

Figure 1.1: Schematic for the uncatalyzed (black) and catalyzed (orange) reaction R $\longleftrightarrow$ TS $\longrightarrow$ P. The uncatalyzed forwards and reverse free energy barriers are $\Delta F^{\ddagger}_{for}$ and $\Delta F^{\ddagger}_{rev}$. The free energy of adsorption for species R and P are labeled $\Delta F_{ads,R}$ and $\Delta F_{ads,P}$, respectively. The forwards and reverse free energy barriers on the catalyst are labeled $\Delta F^{\ddagger}_{for,cat}$ and $\Delta F^{\ddagger}_{rev,cat}$, respectively.

Heterogeneous catalysis refers to catalysis that occurs at the interface between two phases of matter, such as the solid-liquid or solid-gas interface. In contrast, homogeneous catalysis relies on the reaction between species in the same phase, such as in solution. Homogeneous catalysis is less commonly used for industrial applications, as separation and recovery of the catalyst following reaction is expensive and difficult.[15–17] In comparison,

heterogeneous catalysts are typically either fixed in place to the reactor or dispersed on solid material that can be easily separated from the reaction mixture by filtration.

There are still many issues with heterogeneous catalysts as well. One problem is that heterogeneous catalysts tend to degrade over time due to the catalyst leaching into reaction solution. This is not only costly, requiring that the catalyst material be periodically replenished, but also dangerous, as the catalyst material may be biologically or ecologically hazardous.[18,19]

In addition to leaching into solution, catalysts can undergo morphological changes over the course of reaction, thereby affecting catalyst performance. For example, metal catalysts that have been dispersed on a supporting material will frequently agglomerate through a process known as Ostwald ripening, particularly at elevated temperatures.[20] Some support materials may also migrate and begin to cover the metal, resulting in catalyst deactivation, a phenomenon known as the strong metal–support interaction.[21,22] Not only do these changes in morphology affect the activity of metal catalysts, they also make catalyst characterization more difficult, which complicates the development of new catalysts with better properties.

Transport limitations are of particular concern for heterogeneous catalysis. Heterogeneous catalysis occurs at the interface between two phases of matter and as such is inherently limited to two dimensions, while homogeneous catalysis can occur at any point in solution. This can result in a local depletion in the concentration of reactants in the vicinity of the heterogeneous catalyst, thereby slowing the reaction to the rate at which reactants can diffuse to the catalyst surface. While this may not be an issue for perfectly flat catalyst surfaces, most catalysts are dispersed on high-surface-area porous support material such as amorphous carbon.[23] This is done in order to maximize the catalyst concentration, and thereby catalytic activity, but this approach results in slower diffusion to and from the catalyst surface.

These and other complicating factors frustrate attempts to characterize existing heterogeneous catalysts and to design new catalysts with better properties. As a result, theory plays an important role for filling in the gaps of knowledge left by incomplete empirical measurements and for facilitating the discovery of catalytic mechanisms and new catalytic materials. Obtaining a full picture of the chemistry that occurs on heterogeneous catalysts

requires both experimental measurements and theoretical studies.

1.2 Studies of heterogeneous catalysts

The differences between the real catalytic systems used in industry and the simplified model systems used in surface science applications are commonly referred to as the "materials gap" and the "pressure gap." The materials gap refers to the fundamental differences the physical structure of the catalyst in real catalytic systems and in those of model systems. For example, while real catalytic systems are composed of highly irregular polydisperse nanoparticles on high-surface-area supports, model systems of catalysis are typically a single facet of a large, perfect crystal. These model systems often neglect the effects of the supporting material on catalysis, either through modulation of the catalyst's properties or through direct participation of the support in the reaction mechanism. Many real catalysts also employ promoters, the structure and activity of which are not well-known. The use of these simplified models enable the use of certain characterization techniques, as well as the unambiguous identification of the catalytically active site.[24–26] The pressure gap refers to the use of very low pressures for *in situ* experimental characterization of catalysts due to the difficulty of doing such measurements at high pressures or in solution, even though real catalytic systems are typically operated under such conditions.[27,28]

These terms typically are used to refer to the deficiencies of experimental model systems, but they can also be used to describe theoretical models. Despite continuous advances in computational methodology and the increasing availability of computer resources, sufficiently accurate electronic structure theory methods are still limited to small model systems due to computational expense. A consequence of this is that most theoretical studies of heterogeneous catalysis use periodic density functional theory calculations of perfect crystal facets with small unit cells. This can be thought of as the materials gap for theoretical models of heterogeneous catalysis. The pressure gap manifests as a simplification of catalyst environment, for example by neglecting the effect of adsorbate coverage on properties such as binding energies and reaction rates, or by neglecting solvent. Full treatment of solvation effects are prohibitively expensive, arising both from the additional computational expense incurred by the consideration of all

solvent electronic degrees of freedom and from the need to perform proper sampling of the solvent nuclear degrees of freedom.

Despite these issues, it is becoming possible to assess the properties of a catalyst *in silico*, without the need to perform any experimental measurements at all. This has led to the ability to screen catalysts computationally in order to narrow the scope of slower and much more expensive experimental screening studies.[29–34] Computational modeling is not only able to assess the thermodynamic feasibility and stability of proposed catalyst materials, but can also predict the activity and selectivity of catalysts for a particular reaction of interest through the use of kinetic modeling. However, the success of these computational screening studies have been largely qualitative in nature, and quantitative agreement with experiment still requires parameter fitting to experimental measurements.[35] Unfortunately, the fitting of kinetic model parameters to match experiment reduces the predictive ability of a first principles model, as it is known that very different kinetic model parametrizations can have quite similar results.[36] Developing more accurate theoretical models of heterogeneous catalysis without empirical parametrization requires theoretical models that not only represent the catalyst and its active sites accurately, but also afford an accurate treatment of elementary reaction kinetics and a comprehensive consideration of all plausible reaction pathways.

The current inability of purely theoretical models of catalysis to quantitatively reproduce experimental measurements indicate that the current methods used in those models are insufficiently realistic. These issues can arise in the physical model of the catalyst active site, in the treatment of environmental factors such as coverage-dependence or solvent, in the electronic structure theory methods used to calculate adsorbate geometries and binding energies, or in the kinetic models used to simulate catalyst activity. There are many possible ways that these theoretical models could be improved in order to achieve better agreement with experiment. For example, the step edges, kinks, and metal–support interfaces in metal catalysts are known to be more chemically active than the perfect crystal facets, which has led some studies to explicitly consider those sites in their model, though the number of chemically unique active sites in real catalysts are far too large for a comprehensive treatment.[37–39] Other studies have attempted to incorporate the presence of explicit solvent, either with full QM treatment but fixed solvent geometry, or

with continuum solvent methods.[40–42] Multiple improved models of the thermodynamic properties of adsorbates have been proposed.[43–45] More detailed models of the lateral interactions between adsorbates beyond the mean field have been suggested.[46–48] Despite all of these advances, quantitative agreement between purely theoretical models and experimental measurements has yet to be achieved.

The primary objective of the research presented in this work is to analyze how these structural and environmental complications affect catalytic properties through the use of more complex theoretical models. This work has required the development of new theoretical methodology, the creation of a new computer program that implements these techniques, and the investigation of particular catalytic applications which deviate significantly the simplified models that are traditionally used. These advances do not yet result in quantitative agreement with experiment, but they are a step towards that eventual goal.

1.3 Overview

This dissertation is presented in two parts. In the first part, some important background material is reviewed, and the theoretical and technical developments are described. In the second part, several applications of the techniques outlined in the first part are described.

Chapter 2 provides a brief summary of some relevant background knowledge. This chapter also introduces the terminology and symbols used throughout this dissertation. Chapter 3 goes through a rigorous derivation of the partition function for a mean field lattice in the context of microkinetic modeling. The thermodynamic and kinetic parameters necessary for development of a microkinetic model are derived from this partition function, as well as a many-body expansion description of lateral interactions and a capacitor model used to describe the adsorption of ionic species. Chapter 4 introduces the code Micki, which was developed to implement the methodology outlined in chapter 3. Some examples of how to use Micki for typical calculations are provided.

Chapter 5 discusses the impact of support material on heterogeneous metal nanoparticle catalysis. Chapter 6 discusses the esterification of 1-propanol by Pd(111) in liquid

methanol under basic conditions. Chapter 7 discusses the electrocatalytic ORR synthesis of H_2O_2 by CoS_2.

2 BACKGROUND

2.1 The canonical ensemble

In the canonical ensemble, we imagine a system of particles that are coupled to an infinite bath at a fixed temperature. For a single particle, the classical canonical partition function is

$$Q = \frac{1}{h^3} \int d\mathbf{q} d\mathbf{p} e^{-\beta H(\mathbf{q},\mathbf{p})}. \tag{2.1}$$

For a system containing many indistinguishable particles, the partition function is

$$Q = \frac{1}{N! h^{3N}} \int d\mathbf{q}_1 d\mathbf{q}_2 \ldots d\mathbf{p}_1 d\mathbf{p}_2 \ldots e^{-\beta H(\mathbf{q}_1,\mathbf{q}_2,\ldots,\mathbf{p}_1,\mathbf{p}_2,\ldots)}. \tag{2.2}$$

Without loss of generality, we can partition phase space into distinct spatial regions (or states) S_i, where each region has the dimensionality of the entire phase space. Then, each region has its own partition function Q_i,

$$Q_i = \frac{1}{N! h^{3N}} \int_{\mathrm{S}_i} d\mathbf{q}_1 d\mathbf{q}_2 \ldots d\mathbf{p}_1 d\mathbf{p}_2 \ldots e^{-\beta H(\mathbf{q}_1,\mathbf{q}_2,\ldots,\mathbf{p}_1,\mathbf{p}_2,\ldots)}, \tag{2.3}$$

and the full partition function is given by

$$Q = \sum_i Q_i \tag{2.4}$$

(S_i describes a *spatial* region, so the integral in equation 2.3 continues to span all of momentum-space). Given a particular configuration sampled from the classical canonical ensemble, the relative probability of the configuration lying in S_i as compared to S_j is

$$\frac{P(\mathrm{S}_j)}{P(\mathrm{S}_i)} = \frac{Q_j}{Q_i}. \tag{2.5}$$

One way to partition phase space is to consider all points that lie within a particular minimum energy well to be part of the same state (a minimum-nergy well may not have one particular minimum energy configuration, e.g. due to translational symmetry). In

this partitioning, the border between two adjacent regions of phase space S_i and S_j is the *dividing surface* corresponding to the reaction $\mathrm{S}_i \longrightarrow \mathrm{S}_j$. The equilibrium constant for this reaction is given by

$$K^{\mathrm{S}_i \to \mathrm{S}_j} = \frac{Q_j}{Q_i}. \tag{2.6}$$

Note that the equilibrium constant is typically defined for a particular choice of reference state, while the above definition does not suggest any particular reference. In this phase space partitioning scheme, every configuration separated by an energy barrier, no matter how small, will be considered a separate state. In most circumstances, states separated by small, thermally-accessible barriers can be combined and considered a single state.

This partitioning does not distinguish between chemical states separated only by barrierless reactions. In those cases, a judiciously chosen dividing surface must be introduced, for example through minimization of the recrossing probability predicted by molecular dynamics simulations. This approach, known as variational transition state theory, is commonly used to model reactions between radical species in the gas phase, for example in combustion chemistry[49].

In practice, one typically thinks about the *free energy* of particular states, rather than its partition function. The Helmholtz free energy of a system is defined as

$$F_i = -\frac{1}{\beta} \ln Q_i, \tag{2.7}$$

which gives an equilibrium condition of

$$K^{\mathrm{S}_i \to \mathrm{S}_j} = e^{-\beta\left(F_j - F_i\right)}. \tag{2.8}$$

2.2 Ideal gas partition function

In general, the partition function has no analytical expression. However, through the use of a series of simplifying approximations, it is possible to decompose the motion of a system into independent degrees of freedom, each of which has an analytical contribution to the partition function. For example, the motion of the atoms in a molecule in a vacuum

can be broken down into electronic, translational, rotational, and vibrational degrees of freedom,

$$Q \approx Q_{\text{elec}} Q_{\text{trans}} Q_{\text{rot}} Q_{\text{vib}}. \tag{2.9}$$

Under the adiabatic approximation, the electronic contribution to the partition function can be written as

$$Q_{\text{elec}} \approx \omega_0 e^{-\beta E_{\text{elec}}}, \tag{2.10}$$

where ω_0 is the degeneracy of the electronic ground state and E_{elec} is the electronic energy of the molecule in its minimum-energy conformation. This expression assumes that electronic excited states are thermally inaccessible under the conditions of interest.

The translational motion of a molecule in the gas phase at sufficiently low concentration can be approximated by that of an ideal gas, resulting in an approximate partition function of

$$Q_{\text{trans}} \approx \left(\frac{2\pi m}{\beta h^2} \right)^{3/2} V, \tag{2.11}$$

where m is the mass of the whole molecule and V is the system volume.

To separate the rotational and vibrational degrees of freedom of a molecule, we must separate those motions into uncorrelated contributions. This is done by treating the molecule as a rigid rotor with a well-defined inertia tensor, which results in a rotational partition function of the form

$$Q_{\text{rot}} \approx \frac{\sqrt{\pi}}{\sigma_{\text{rot}}} \left(\frac{8\pi^2}{\beta h^2} \right)^{3/2} \text{Tr}\left[\mathbf{I}\right] \tag{2.12}$$

for nonlinear molecules and

$$Q_{\text{rot}} \approx \frac{8\pi^2 I}{\sigma_{\text{rot}} \beta h^2} \tag{2.13}$$

for linear molecules, where σ_{rot} is the rotational symmetry number for the molecule, $\mathbf{I}$ is the inertia tensor for a nonlinear molecule, and I is the scalar moment of inertia for a linear molecule. In all cases, the moment of inertia corresponds to the molecule in its minimum-energy configuration.

Finally, the vibrational motions of the molecule can be approximated by the harmonic

oscillator model, which has a partition function of the form

$$Q_{\text{vib}} \approx \prod_{i}^{N_{\text{vib}}} \frac{e^{-\beta h \nu_i / 2}}{1 - e^{-\beta h \nu_i}}, \tag{2.14}$$

where ν_i are the frequencies of the vibrational normal modes of the molecule.

Not only do each of these contributions to the partition function involve their own approximations, but the assumption that the partition function can be factored into individual contributions in this way is also an approximation. In reality, all electronic and nuclear degrees of freedom are inexorably coupled to one another. Furthermore, while the expression for the partition function of a state described in the previous section involves an integral spanning the region of phase space belonging to a particular energy minimum, the expression derived here assumes infinite harmonic energy barriers for all intramolecular degrees of freedom. While this approach may be sufficient for the purposes of calculating free energy differences, it cannot accurately reproduce absolute free energies.

In the following work, we shall use equations 2.9 through 2.14 as an approximation for the partition function of gas-phase species. Additionally, equation 2.14 will be used to represent the vibrational motion of molecules adsorbed to the surface of heterogeneous catalysts. It is important to recognize that these expressions are approximations, and that the predictive power of models using these expressions are limited by the accuracy of the approximations.

An aside on units

Consider the reaction between ideal gases

$$\mathrm{A} + \mathrm{B} \longrightarrow \mathrm{C}. \tag{2.15}$$

The partition function for the entire system containing species A, B, and C is

$$Q = \left(\frac{Q_{\mathrm{A}}^{N_{\mathrm{A}}}}{N_{\mathrm{A}}!}\right)\left(\frac{Q_{\mathrm{B}}^{N_{\mathrm{B}}}}{N_{\mathrm{B}}!}\right)\left(\frac{Q_{\mathrm{C}}^{N_{\mathrm{C}}}}{N_{\mathrm{C}}!}\right). \tag{2.16}$$

The chemical potential for each species is given by

$$\mu_X = -\frac{1}{\beta}\frac{d\ln Q}{dN_X} = -\frac{1}{\beta}\ln\frac{Q_X}{N_X}. \tag{2.17}$$

By enforcing $\mu_A + \mu_B = \mu_C$, we obtain an expression for the equilibrium condition,

$$K^{A+B\to C} = \frac{Q_C}{Q_A Q_B} = \frac{N_C}{N_A N_B}. \tag{2.18}$$

Since N is an extensive property of the system, the equilibrium condition scales inversely with the system volume. This is consistent, as the partition function for each species also scales with system volume, but it is not particularly useful. It is possible to divide each term in this expression by the system volume V to obtain a properly intensive equilibrium condition,

$$K^{A+B\to C}_{\text{intensive}} = \frac{(Q_C/V)}{(Q_A/V)(Q_B/V)} = \frac{\rho_C}{\rho_A\rho_B}, \tag{2.19}$$

where $\rho = N/V$ is a number density or concentration. However, $K_{\text{intensive}}$ now has units of volume, rather than being unitless, as we expect for an equilibrium constant.

To solve this issue, we introduce a *reference state* for each component of a system, and divide each term in the above equilibrium expression by its reference concentration ρ°,

$$K^{A+B\to C}_{eq} = \left(\frac{(Q_C/V)}{(Q_A/V)(Q_B/V)}\right)\left(\frac{\rho^\circ_A\rho^\circ_B}{\rho^\circ_C}\right) = \left(\frac{\rho_C}{\rho_A\rho_B}\right)\left(\frac{\rho^\circ_A\rho^\circ_B}{\rho^\circ_C}\right) \tag{2.20}$$

$$= \frac{Q^\circ_C}{Q^\circ_A Q^\circ_B} = \frac{a_C}{a_A a_B}. \tag{2.21}$$

We have defined Q° to be the partition function of a species evaluated at its reference state and $a = \rho/\rho^\circ$ to be the *activity* of a species. This is also related to the standard free energy,

$$K^{A+B\to C}_{eq} = e^{-\beta\left(F^\circ_C - F^\circ_A - F^\circ_B\right)}, \tag{2.22}$$

where

$$F_i^\circ = -\frac{1}{\beta} \ln Q_i^\circ. \tag{2.23}$$

This is the standard definition of the equilibrium constant for a reaction, and it will be used throughout this work.

2.3 Transition state theory

Predicting the rate of a chemical reaction requires knowledge both of the thermodynamics of the reaction coordinate and of the dynamics of the molecules moving on the potential energy surface. In transition state theory, we decompose an elementary reaction into two steps,

$$\mathrm{A} + \mathrm{B} \longleftrightarrow \mathrm{AB}^\ddagger \longrightarrow \mathrm{C}, \tag{2.24}$$

where $\mathrm{AB}^\ddagger$ is the *transition state* connecting the reactants, A + B, to the product, C. As discussed in the previous section, this transition state corresponds to the boundary between the region of phase space corresponding to the state A + B and the state C, and consequently has one fewer degree of freedom than either of the two end states.

In traditional (non-variational) transition state theory, we then assume that any $\mathrm{AB}^\ddagger$ that forms is immediately transformed into C with a characteristic rate ν related to the curvature of the reaction coordinate at the transition state,

$$r_{\mathrm{A+B}\to\mathrm{C}} = \nu a_{\mathrm{AB}^\ddagger}. \tag{2.25}$$

Further assuming that the initial state A + B is in equilibrium with the transition state $\mathrm{AB}^\ddagger$, the forwards reaction rate is written as

$$r_{\mathrm{A+B}\to\mathrm{C}} = \nu K_{\mathrm{eq}}^{\mathrm{A+B}\to\mathrm{AB}^\ddagger} a_\mathrm{A} a_\mathrm{B}, \tag{2.26}$$

where

$$K_{\mathrm{eq}}^{\mathrm{A+B}\to\mathrm{AB}^\ddagger} = \frac{a_{\mathrm{AB}^\ddagger}}{a_\mathrm{A} a_\mathrm{B}} = \frac{Q^\circ_{\mathrm{AB}^\ddagger}}{Q^\circ_{\mathrm{A+B}}}. \tag{2.27}$$

In the interest of generality, the partition function for the reactants has not been separated

into contributions arising from species A and B. Here, $Q_{\mathrm{AB}^\ddagger}$ is the full $3N$-dimensional partition function of the transition state, including the motion in the direction of the reaction coordinate. If we consider this motion to be that of a classical harmonic oscillator with frequency ν, the rate can be rewritten as

$$r_{\mathrm{A+B}\to\mathrm{C}} = \frac{k_B T}{h} \frac{Q^{\circ\prime}_{\mathrm{AB}^\ddagger}}{Q^\circ_{\mathrm{A+B}}} a_{\mathrm{A}} a_{\mathrm{B}}, \tag{2.28}$$

where the accent in $Q^{\circ\prime}_{\mathrm{AB}^\ddagger}$ indicates that the motion in the direction of the reaction coordinate has been pulled out of the partition function. Similarly, the reverse rate is given by

$$r_{\mathrm{C}\to\mathrm{A+B}} = \frac{k_B T}{h} \frac{Q^{\circ\prime}_{\mathrm{AB}^\ddagger}}{Q^\circ_{\mathrm{C}}} a_{\mathrm{C}}. \tag{2.29}$$

In equilibrium, the forward and reverse rates should be equal to one another, giving the expression

$$\frac{r_{\mathrm{A+B}\to\mathrm{C}}}{r_{\mathrm{C}\to\mathrm{A+B}}} = \frac{Q^\circ_{\mathrm{C}}}{Q^\circ_{\mathrm{A+B}}} \frac{a_{\mathrm{A}} a_{\mathrm{B}}}{a_{\mathrm{C}}} = 1, \tag{2.30}$$

which correctly reproduces the equilibrium condition derived earlier,

$$\frac{Q^\circ_{\mathrm{C}}}{Q^\circ_{\mathrm{A+B}}} = \frac{a_{\mathrm{C}}}{a_{\mathrm{A}} a_{\mathrm{B}}} = K_{\mathrm{eq}}^{\mathrm{A+B}\to\mathrm{C}}. \tag{2.31}$$

This approach neglects the effect of dynamics that may lead the system to recross the transition state back into the reactant well. In variational transition state theory, recrossing is included through the use of a constant recrossing probability factor in the reaction rate. Throughout this work, we assume that no recrossing occurs.

2.4 Density functional theory

Density functional theory is a method for approximately solving Schrödinger's equation,

$$\left(-\frac{1}{2} \sum_i \nabla_i^2 - \sum_i \sum_\alpha \frac{Z_\alpha}{|\mathbf{r}_i - \mathbf{r}_\alpha|} + \frac{1}{2} \sum_i \sum_{j \neq i} \frac{1}{|\mathbf{r}_i - \mathbf{r}_j|} \right) \Psi = E\Psi. \tag{2.32}$$

Here, the indices i run over all electrons, the indices α run over all nuclei, ∇^2 is the Laplacian operator, and Z_α is the nuclear charge of atom α. In the Kohn-Sham formulation of density functional theory,[50] this is reformulated as a system of non-interacting electrons that has the same electron density due to the introduction of an effective external potential V_{eff},

$$\left(-\frac{1}{2} \sum_i \nabla_i^2 - \sum_i \sum_\alpha \frac{Z_\alpha}{|\mathbf{r}_i - \mathbf{r}_\alpha|} + V_{\text{eff}} \right) \Psi = E\Psi. \tag{2.33}$$

According to the Hohenberg–Kohn theorem, this DFT Hamiltonian will necessary yield the same energy as the true many-body Hamiltonian so long as both systems have the same ground state electron density.[51] The effective potential V_{eff} is normally broken into two parts,

$$V_{\text{eff}}(\mathbf{r}) = V_{\text{H}}(\mathbf{r}) + V_{\text{xc}}(\mathbf{r}), \tag{2.34}$$

where

$$V_{\text{H}}(\mathbf{r}) = \int d\mathbf{r}' \frac{n(\mathbf{r}')}{|\mathbf{r} - \mathbf{r}'|}, \tag{2.35}$$

is the Hartree potential,

$$n(\mathbf{r}) = |\Psi(\mathbf{r})|^2 \tag{2.36}$$

is the electron density, and V_{xc} is the unknown exchange-correlation potential.

Thus, in DFT, one approximates the true many-body interaction with an effective one-body exchange-correlation potential V_{xc}. Different DFT functionals differ in their approximations for V_{xc}, with most functionals representing V_{xc} in terms of a local expansion of the density around a particular region in space. The simplest functional is that of the local density approximation (LDA), which relates the contribution to the energy of each point in space to the energy of the homogeneous electron gas of the same density.[50] While this functional is (perhaps surprisingly) somewhat accurate for metals, it fails qualitatively at representing molecules or other systems with localized features in the electron density such as covalent bonds or lone pairs.[52,53] Slightly more complex approximations known as generalized gradient approximations (GGAs) treat the energy as a function of both the local density and its gradient.[54] Meta-GGAs further include the local density curvature or the local kinetic energy density gradient (which is derived from the DFT orbitals, rather than the electron density).[55] Hybrid functionals further include some fraction of

exact Hartree–Fock exchange, which at least partially alleviates the delocalization errors observed with other DFT methods.[56]

However, all of the approaches outlined above fail to account for long-range nonlocal interactions, such as dispersion. Since these interactions are long range, semi-local approximations such as LDAs, GGAs, and meta-GGAs cannot capture them. Hybrid functionals also fails to capture these interactions, as they are a form of non-local electron correlation, which is not accounted for in Hartree–Fock. One expects dispersion to play an important role in catalysis, particularly for metallic systems, owing to the high polarizability of metal atoms. Consequently, it is important to consider ways to account for this missing interaction in DFT.

One approach to incorporate dispersion in DFT is that of the vdW-DF family of functionals.[57] These functionals include an explicit nonlocal correlation energy through approximation of the formally exact adiabatic connection fluctuation and dissipation theorem formulation of the correlation energy. However, despite the success of such functionals for non-metallic layered systems and van der Waals complexes, vdW-DF functionals fail to accurately represent metallic systems, leading to among other issues lattice constants that are far too large.[58] An alternative approach is the use of a classical force field-like potential for long range interactions neglected by semilocal DFT functionals.[59] This approach also poses a problem for metallic systems, as pairwise additive dispersion corrections will over-bind metallic systems due to a lack of dielectric screening.[60] In a many-body expansion of the correlation energy, this screening would manifest as three-body and higher-order terms. The three-body DFT-D3(ABC) potential developed by Grimme partially captures the effect of this screening, thereby lowering the dispersion energy of the system relative to the simple pairwise-additive formulation, DFT-D3.[61–65] We find that DFT-D3(ABC), in conjunction with the GGA functional PBE results in accurate lattice constants for metals and binding energies of molecular adsorbates to metal surfaces. The dispersion-corrected range-separated hybrid functional HSE06-D3(BJ,ABC) further improves upon the results of PBE-D3(ABC), but at a much higher computational cost.[66–70] We have implemented the three-body D3(ABC) and D3(BJ,ABC) dispersion correction schemes into ASE and natively into VASP as a patch.[71] The above-mentioned functionals have been used extensively in this work.

3 MICROKINETIC MODELING OF HETEROGENEOUS CATALYST KINETICS

3.1 Motivation

Kinetic modeling is a powerful tool for both experimental and theoretical studies of complex reaction networks. It can be used both to extend experimental data to reaction conditions different from those used in experiment, and to predict the behavior of a reaction network starting from first principles calculations. Furthermore, a detailed analysis of kinetic models can elucidate ways in which a reaction can be improved, such as by identifying rate-limiting steps or rate-inhibiting side-pathways.

Modeling reaction kinetics exactly would require detailed knowledge about the positions and momenta of all particles in a system and a sufficient level of sampling to allow full convergence. Since this is intractable for all but the most simple systems, certain approximations must be made in order to study the kinetics of physically relevant systems. It is common to use the mean field approximation to represent the state of the catalyst, which reduces the distribution of adsorbates to an average coverage for each species. This approximation transforms a series of elementary reaction rate expressions into a system of differential algebraic expressions, which can then be solved for by various means.[72] As an alternative to the mean field approximation, some reaction networks can be analyzed by Monte Carlo methods, such as lattice kinetic Monte Carlo.[73] This approach allows one to incorporate the instantaneous environment of adsorbates on the thermodynamic and kinetic parameters of reactions involving those species.

In general, the differential algebraic expressions derived from a mean field approximation cannot be solved analytically. This is because there typically exists an interdependency of the rates of formation and depletion of all species in the reaction network on all other species. For certain systems, and under certain conditions, it may be possible to make specific approximations that render a reaction network analytically solvable (e.g., by approximating a particular reaction step as being irreversible, or as in equilibrium). However, even kinetic models for which such approximations are not amenable can be analyzed

using numerical techniques.

In this work, we present a rigorous theoretical motivation for construction of a mean-field microkinetic model informed primarily by first principles calculations. We also introduce Micki, a tool for construction and solution of *ab initio* microkinetic models. Using the definition of James Dumesic, a microkinetic model is a kind of kinetic model in which all unique species in the system are considered as separate entities, all reactions considered are elementary steps, and the kinetic parameters of each reaction are independent of one another.[72] Such models are commonly used to study the kinetics of heterogeneous catalysis.

In the following sections, we rigorously derive a partition function for a system comprising a mean field lattice representing a catalyst surface and a fluid phase that contains reactants and products. In particular, we account for the symmetry of multidentate adsorbates, resulting in a configurational entropy term that is neglected in common applications of microkinetic modeling. We further expand upon this model by incorporating the lateral interactions between adsorbates as a many-body expansion of the lattice free energy, resulting in a rigorous, flexible, and thermodynamically consistent model for lateral interactions. From the partition function, we derive reaction rate expressions for elementary steps and their corresponding equilibrium constants and rate constants. We then discuss the implementation of these expressions in Micki, and give an example of how to use Micki to predict catalytic properties such as turn over frequencies, rate orders, and sensitivities.

3.2 The partition function

In order to derive all thermodynamic and kinetic parameters that enter into a microkinetic model, we begin by defining the standard partition function for a system comprising a mean-field lattice and a mean-field fluid. Because these two phases are separate and do not interact in our model, the partition function for the full system can be factored into the mean-field lattice partition function and the mean-field fluid partition function.

Lattice

A lattice is characterized by its geometry (e.g. hexagonal, square) and the characteristic area of each site. For example, the (111) surface of an FCC metal has a hexagonal geometry, in which each site is adjacent to 6 other sites, and the area of each site is given by $\frac{\sqrt{3}}{4}a^2$, where a is the lattice constant of that metal. Given a lattice of M sites containing N_i many of each adsorbate i, each of which has a one-particle partition function Q_i, and assuming each adsorbate occupies only a single site, the full partition function for the lattice is

$$Q = \prod_i \prod_{n=1}^{N_i} \frac{\left(M - \sum_{j<i} N_j - (n-1)\right)}{n} Q_i \tag{3.1}$$

$$= \frac{M!}{\left(M - \sum_i N_i\right)!} \prod_i \frac{Q_i^{N_i}}{N_i!} \tag{3.2}$$

$$= \frac{M!}{N_*!} \prod_i \frac{Q_i^{N_i}}{N_i!}, \tag{3.3}$$

where we have defined $N_* \equiv M - \sum_i s_i N_i$ to be the number of vacant sites on the lattice, where s_i is equal to the number of sites occupied by each species i. The term inside the parentheses in equation 3.1 (the multiplicand) counts the number of vacant sites available to the n^{th} adsorbate of species i for binding. Equation 3.3 is the standard expression for a partition function used in mean-field models of heterogeneous catalysis, including microkinetic modeling studies. The one-particle partition function Q_i can be written as

$$Q_i \approx Q_i^{\text{elec}} Q_i^{\text{hind-trans}} Q_i^{\text{hind-rot}} Q_i^{\text{vib}}. \tag{3.4}$$

Q_i^{elec} and Q_i^{vib} have the same form as for the ideal gas as described in equations 2.10 and 2.14, while $Q_i^{\text{hind-trans}}$ and $Q_i^{\text{hind-rot}}$ correspond to hindered translation and hindered rotation on the surface. There are a number of ways to account for these hindered motions, but herein we shall treat all molecular degrees of freedom as vibrations. Note that the lattice partition function is very similar to that of the ideal gas, with the exception of the first term, $\frac{M!}{N_*!}$. This term enforces the indistinguishability of vacant sites, such that the partition function of an empty lattice is equal to 1.

To properly incorporate adsorbates that occupy multiple binding sites simultaneously,

i.e. multidentate adsorbates, the partition function must be modified to account for the number of different orientations possible for these adsorbates. If the lattice sites for an adsorbate that occupies multiple binding sites are assigned one at a time, then while the first site can be any of the N_* vacant sites, subsequent sites must be adjacent to the previously assigned site. For any given binding site, in the mean field approximation, the probability that the site is unoccupied and thus counts as a possible binding geometry is

$$p = \frac{N_*}{M}. \tag{3.5}$$

For an adsorbate that occupies multiple sites, given that we have assigned the first site, the number of possible choices for the second site is

$$\sum_{m=1}^{\sigma} m \binom{\sigma}{m} p^m (1-p)^{\sigma-m} = \sigma p, \tag{3.6}$$

where σ is the number of nearest neighbors for each lattice site.

In the mean field approximation, the probability p that a given site is free will be the same for all sites. For example, if we are considering the number of orientations available for the second site of a bidentate adsorbate, and we have already assigned N_x other adsorbates, then in the mean field approximation, p will be

$$p = \frac{M - 2N_x - 1}{M}. \tag{3.7}$$

The 1 in the numerator accounts for the site already occupied by the first part of the adsorbate.

For species occupying three or more sites, we can reuse the expression in equation 3.6 and replace σ with the number of possible orientations for the third and any subsequent binding site. We define $\sigma_{i,k}$ to be the number of different possible orientations for the kth site of species i, given that all sites $< k$ have already been assigned. In general, we can

write the partition function as

$$Q_{\text{latt}} = \prod_i \prod_{n=1}^{N_i} \left[Q_i \left(\frac{M - \sum_{j<i} s_j N_j - s_i (n-1)}{n} \right) \times \prod_{k=2}^{s_i} \sigma_{i,k} \left(\frac{M - \sum_{j<i} s_j N_j - s_i (n-1) - k + 1}{M} \right) \right] \tag{3.8}$$

$$= \frac{M!}{N_*!} \prod_i \left(\frac{\sigma_i Q_i}{M^{s_i - 1}} \right)^{N_i} \frac{1}{N_i!}, \tag{3.9}$$

where s_i is the number of sites to which species i binds, $\sigma_{i,k}$ is the number of possible orientations for the kth site of species i, and

$$\sigma_i = \prod_{k=2}^{s_i} \sigma_{i,k} \tag{3.10}$$

is the the "symmetry number" for adsorbate i. The multiplicand in the first line of equation 3.8 accounts for the number of vacant sites available to the first part of the n^{th} adsorbate of species i, analogous to equation 3.1. The multiplicand in the second line counts the number of sites available to the second part of that species. Note that in this formalism, $\sigma_{i,2} = \frac{\sigma}{2}$ if the adsorbate has end-to-end symmetry, and $\sigma_{i,2} = \sigma$ if it does not. This eliminates double-counting arising from the indistinguishability between orientations of a molecule when it is flipped end-to-end.

Thus, the full partition function for a system comprising a fluid and a lattice can be written as

$$Q = \frac{M!}{N_*!} \prod_i^{\text{fluid}} \frac{Q_i^{N_i}}{N_i!} \prod_j^{\text{adsorbate}} \left(\frac{\sigma_j Q_j}{M^{s_j - 1}} \right)^{N_j} \frac{1}{N_j!}. \tag{3.11}$$

While configurational symmetry has been incorporated in an *ad hoc* fashion in previous applications of microkinetic modeling, this is the first rigorous derivation of the lattice partition function for multidentate adsorbates with contributions arising from configurational degrees of freedom.

3.3 Thermodynamic and kinetic parameters

Thermodynamic parameters

The chemical potential of a species in the lattice is given as

$$\mu_i = -\frac{1}{\beta} \ln \left(\frac{\theta_*^{s_i} \sigma_i Q_i}{\theta_i} \right). \tag{3.12}$$

For example, the equilibrium condition for the on-lattice reaction

$$\mathrm{A}* + \mathrm{B}* \longrightarrow \mathrm{C}** \tag{3.13}$$

is

$$K_{\mathrm{eq}} = \frac{\theta_{\mathrm{C}}}{\theta_{\mathrm{A}} \theta_{\mathrm{B}}} = \frac{\sigma_{\mathrm{C}} Q_{\mathrm{C}}}{\sigma_{\mathrm{A}} Q_{\mathrm{A}} \sigma_{\mathrm{B}} Q_{\mathrm{B}}} = e^{-\beta \Delta F^\circ}. \tag{3.14}$$

This is the standard expression for the equilibrium constant for an on-surface reaction with the exception of the σ_{X} terms, which account for the configurational degrees of freedom of the adsorbate on the lattice. In general, $\sigma_{\mathrm{X}} = 1$ for adsorbates occupying only a single site. The free energy of this reaction is

$$\Delta F^\circ = F_{\mathrm{C}}^\circ - F_{\mathrm{A}}^\circ - F_{\mathrm{B}}^\circ \tag{3.15}$$

$$F_{\mathrm{X}}^\circ = -\frac{1}{\beta} \ln \left(\sigma_{\mathrm{X}} Q_{\mathrm{X}} \right) \tag{3.16}$$

where the σ term in equation 3.16 corresponds to the configurational contribution to the free energy. Note that while we use the symbol F° when referring to the free energy of adsorbates for consistency with the fluid phase, the absolute free energy of an adsorbate is not dependent on the choice of reference state in this formalism. This is because the adsorbate entropy does not scale with the size of the system, as they are considered constrained to a set of lattice sites.

If the number of sites occupied by the reactants is different from the number of sites occupied by the products, the equilibrium condition changes slightly. For example, for a

reaction of the form

$$\mathrm{A}* + \mathrm{B}* \longleftrightarrow \mathrm{C}* + *, \tag{3.17}$$

the equilibrium constant is given by

$$K_{\mathrm{eq}} = \frac{\theta_{\mathrm{C}}\theta_*}{\theta_{\mathrm{A}}\theta_{\mathrm{B}}} = \frac{\sigma_{\mathrm{C}}Q_{\mathrm{C}}}{\sigma_{\mathrm{A}}Q_{\mathrm{A}}\sigma_{\mathrm{B}}Q_{\mathrm{B}}} = e^{-\beta\Delta F^\circ}. \tag{3.18}$$

In general, we can consider a reaction of the form

$$\sum_{i=1}^{N_{\mathrm{R}}} n_{\mathrm{R}_i}\mathrm{R}_i\,(*)^{s_{\mathrm{R}_i}} + \left(\sum_{j=1}^{N_{\mathrm{P}}} n_{\mathrm{P}_j}s_{\mathrm{P}_j}\right)* \longleftrightarrow \sum_{j=1}^{N_{\mathrm{P}}} n_{\mathrm{P}_j}\mathrm{P}_j\,(*)^{s_{\mathrm{P}_j}} + \left(\sum_{i=1}^{N_{\mathrm{R}}} n_{\mathrm{R}_i}s_{\mathrm{R}_i}\right)*, \tag{3.19}$$

where i runs over unique reactants, j runs over unique products, n_{X} is the stoichiometric coefficient for species X, and s_{X} is the number of lattice sites occupied by species X. The second terms in both the left and right sides of this reaction account for conservation of the total number of lattice sites. The equilibrium constant for this reaction is

$$K_{\mathrm{eq}} = \prod_i^{N_{\mathrm{R}}}\left(\theta_{\mathrm{R}_i}\theta_*^{-s_{\mathrm{R}_i}}\right)^{-n_{\mathrm{R}_i}}\prod_j^{N_{\mathrm{P}}}\left(\theta_{\mathrm{P}_j}\theta_*^{-s_{\mathrm{P}_j}}\right)^{n_{\mathrm{P}_j}} = \prod_i^{N_{\mathrm{R}}}\left(\sigma_{\mathrm{R}_i}Q_{\mathrm{R}_i}\right)^{-n_{\mathrm{R}_i}}\prod_j^{N_{\mathrm{P}}}\left(\sigma_{\mathrm{P}_j}Q_{\mathrm{P}_j}\right)^{n_{\mathrm{P}_j}} = e^{-\beta\Delta F^\circ}, \tag{3.20}$$

and the free energy of reaction is

$$\Delta F^\circ = \sum_{j=1}^{N_{\mathrm{P}}} n_{\mathrm{P}_j}F^\circ_{\mathrm{P}_j} - \sum_{i=1}^{N_{\mathrm{R}}} n_{\mathrm{R}_i}F^\circ_{\mathrm{R}_i}. \tag{3.21}$$

For an adsorption reaction of the form

$$\mathrm{A} + * \longleftrightarrow \mathrm{A}*, \tag{3.22}$$

the equilibrium constant is

$$K_{\mathrm{eq}} = \frac{\theta_{\mathrm{A}}}{a_{\mathrm{A}}\theta_*} = \frac{\sigma_{\mathrm{A}}Q^\circ_{\mathrm{A,ads}}}{Q^\circ_{\mathrm{A,fluid}}} = e^{-\beta\Delta F^\circ} \tag{3.23}$$

where Q_{ads} is the partition function for the adsorbate and Q_{fluid} is the partition function for the fluid-phase species. This is again the standard expression for the equilibrium constant

of adsorption, with the exception of the σ_A term that accounts for the configurational entropy of adsorbed species A. The free energy of reaction is

$$\Delta F^\circ = F^\circ_{A,ads} - F^\circ_{A,fluid}, \tag{3.24}$$

where the free energy of fluids is described by equation 2.23 and the free energy of adsorbates is described by equation 3.16.

Kinetic parameters

For a diffusion-controlled reaction in the fluid phase of the form

$$A + B \longleftrightarrow C, \tag{3.25}$$

the rate expression is

$$r = k_{for} a_A a_B - k_{rev} a_C, \tag{3.26}$$

where

$$k_{for} = 4\pi D R \rho^\circ_C \tag{3.27}$$

$$k_{rev} = \frac{k_{for}}{K_{eq}}, \tag{3.28}$$

where $D = D_A + D_B$ is the relative diffusion constant between species A and B and $R = R_A + R_B$ is the sum of the effective radii of species A and B. k_{rev} is determined from k_{for} and K_{eq} to enforce that the reaction obeys detailed balance. This expression assumes that reaction is fast and barrierless upon collision of species A with B. We approximate the radius of a species by the average center-of-mass radius of the molecule as determined using the van der Waals radii of its atoms.[74] This approximation results in reasonable reaction rate constants, on the order of 10^{10} M/s for solution-phase diffusion-limited reactions. The rate of a non-diffusion-limited fluid-phase reaction of this form can be described with transition state theory.

Next, we derive the rate for an on-lattice reaction of the form

$$\mathrm{A}* + \mathrm{B}* \longleftrightarrow \mathrm{AB}^{\ddagger}** \longrightarrow \mathrm{C}**, \tag{3.29}$$

where $\mathrm{AB}^{\ddagger}$ is the transition state connecting the reactants A + B to the product C. The rate expression for this reaction is

$$r = k_{\mathrm{for}}\theta_{\mathrm{A}}\theta_{\mathrm{B}} - k_{\mathrm{rev}}\theta_{\mathrm{C}}. \tag{3.30}$$

The rate constants for this reaction are

$$k_{\mathrm{for}} = \frac{1}{\beta h}\frac{\sigma_{\mathrm{AB}^{\ddagger}}Q'_{\mathrm{AB}^{\ddagger}}}{\sigma_{\mathrm{A}}Q_{\mathrm{A}}\sigma_{\mathrm{B}}Q_{\mathrm{B}}} = \frac{1}{\beta h}e^{-\beta\Delta F^{\circ\ddagger}_{\mathrm{for}}} \tag{3.31}$$

$$k_{\mathrm{rev}} = \frac{1}{\beta h}\frac{\sigma_{\mathrm{AB}^{\ddagger}}Q'_{\mathrm{AB}^{\ddagger}}}{\sigma_{\mathrm{C}}Q_{\mathrm{C}}} = \frac{1}{\beta h}e^{-\beta\Delta F^{\circ\ddagger}_{\mathrm{rev}}}, \tag{3.32}$$

which is analogous to the transition state theory result presented in section 2.3. These expressions for the rate constant are valid regardless of the number of lattice sites occupied by species A, B, $\mathrm{AB}^{\ddagger}$, or C.

For a general reaction of the form

$$\sum_{i=1}^{N_{\mathrm{R}}} n_{\mathrm{R}_i}\mathrm{R}_i\,(*)^{s_{\mathrm{R}_i}} + \left(\sum_{j=1}^{N_{\mathrm{P}}} n_{\mathrm{P}_j}s_{\mathrm{P}_j}\right)* \longleftrightarrow \mathrm{TS}^{\ddagger} \longrightarrow \sum_{j=1}^{N_{\mathrm{P}}} n_{\mathrm{P}_j}\mathrm{P}_j\,(*)^{s_{\mathrm{P}_j}} + \left(\sum_{i=1}^{N_{\mathrm{R}}} n_{\mathrm{R}_i}s_{\mathrm{R}_i}\right)*, \tag{3.33}$$

the rate constants are

$$k_{\mathrm{for}} = \frac{1}{\beta h}\sigma_{\mathrm{TS}^{\ddagger}}Q'_{\mathrm{TS}^{\ddagger}}\prod_{i}^{N_{\mathrm{R}}}\left(\sigma_{\mathrm{R}_i}Q_{\mathrm{R}_i}\right)^{-n_{\mathrm{R}_i}} = \frac{1}{\beta h}e^{-\beta\Delta F^{\circ\ddagger}_{\mathrm{for}}} \tag{3.34}$$

$$k_{\mathrm{rev}} = \frac{1}{\beta h}\sigma_{\mathrm{TS}^{\ddagger}}Q'_{\mathrm{TS}^{\ddagger}}\prod_{j}^{N_{\mathrm{P}}}\left(\sigma_{\mathrm{P}_j}Q_{\mathrm{P}_j}\right)^{-n_{\mathrm{P}_j}} = \frac{1}{\beta h}e^{-\beta\Delta F^{\circ\ddagger}_{\mathrm{rev}}}. \tag{3.35}$$

For adsorption reactions of gas-phase species of the form,

$$\mathrm{A} + * \longleftrightarrow \mathrm{A}*, \tag{3.36}$$

the rate constant is described by collision theory,

$$r = k_{\text{ads}} a_{\text{A}} \theta_* - k_{\text{des}} \theta_{\text{A}} \tag{3.37}$$

$$k_{\text{ads}} = S_0 N_{\text{av}} A_{\text{site}} \left(2\pi m_{\text{A}} \beta\right)^{-1/2} \rho_{\text{A}}^{\circ} \tag{3.38}$$

$$k_{\text{des}} = \frac{k_{\text{ads}}}{K_{\text{eq}}}, \tag{3.39}$$

where S_0 is the sticking coefficient, N_{av} is Avogadro's number, A_{site} is the area of a single adsorption site on the lattice, and m_{A} is the mass of species A. Here, k_{des} is defined such that the overall reaction obeys detailed balance. This expression can be derived both from the kinetic theory of gasses and from transition state theory, in which the transition state is considered to be the gas-phase reactant confined to a two-dimensional box with area A_{site}.

For solution-phase reactions, adsorption of molecules to the catalyst surface tends to be diffusion-limited. The diffusion of particles in solution is governed by Brownian dynamics, which makes solution-phase mass transport both towards and away from the catalyst surface considerably slower than in the gas phase.

To solve this issue, we develop a model for diffusion-limited adsorption to the catalyst surface. In this model, we assume that surface adsorbates are in equilibrium with the thin layer of solution that is in direct contact with the catalyst surface. In order for an adsorbate to leave the catalyst, it must then diffuse through a layer of stationary solvent, beyond which we assume the solution becomes well mixed. As an example, for a reaction of the form

$$\text{A}_{(\text{sol'n})} + * \longleftrightarrow \text{A}*, \tag{3.40}$$

the flux of species A towards the surface is given by Fick's first law of diffusion:

$$J = D_{\text{A}} \left(\frac{\rho_{\text{A}}(\infty) - \rho_{\text{A}}(0)}{L} \right), \tag{3.41}$$

where D_{A} is the diffusion constant of species A, $\rho_{\text{A}}(\infty)$ is the concentration of species A in bulk solution, $\rho_{\text{A}}(0)$ is the concentration of species A in the thin layer that is in direct contact with the catalyst surface, and L is the thickness of the stationary layer. In the

steady state, any net flux of a species from solution towards the surface must result in adsorption. Similarly, any net flux of a species away from the surface into solution must be due to desorption. Therefore, we relate the rate of change of the adsorbed species concentration to this diffusion,

$$\frac{d\theta_{\mathrm{A}}}{dt} = JA_{\mathrm{site}} = D_{\mathrm{A}}A_{\mathrm{site}}\left(\frac{\rho_{\mathrm{A}}(\infty) - \rho_{\mathrm{A}}(0)}{L}\right). \tag{3.42}$$

$\rho_{\mathrm{A}}(0)$ can be calculated from the Langmuir adsorption model

$$\rho_{\mathrm{A}}(0) = \frac{\theta_A \rho_{\mathrm{A}}^{\circ}}{K_{\mathrm{eq}}\theta_*}, \tag{3.43}$$

where K_{eq} is the equilibrium constant for adsorption,

$$K_{\mathrm{eq}} = e^{-\beta F_{\mathrm{ads}}^{\circ}}. \tag{3.44}$$

Then, the overall rate of change of species A on the surface due to adsorption and desorption is

$$\frac{d\theta_{\mathrm{A}}}{dt} = JA_{\mathrm{site}} = D_{\mathrm{A}}A_{\mathrm{site}}\left(\frac{\rho_{\mathrm{A}}(\infty) - \frac{\theta_A\rho_{\mathrm{A}}^{\circ}}{K_{\mathrm{eq}}\theta_*}}{L}\right) \tag{3.45}$$

$$= \left(\frac{D_{\mathrm{A}}A_{\mathrm{site}}\rho_{\mathrm{A}}^{\circ}}{L}\right)a_{\mathrm{A}} - \left(\frac{D_{\mathrm{A}}A_{\mathrm{site}}\rho_{\mathrm{A}}^{\circ}}{K_{\mathrm{eq}}\theta_* L}\right)\theta_{\mathrm{A}}, \tag{3.46}$$

where we have defined $a_{\mathrm{A}} = \rho_{\mathrm{A}}(\infty)/\rho_{\mathrm{A}}^{\circ}$. From this, we define a rate expression of the form

$$r_{\mathrm{ads}} = k_{\mathrm{ads}}a_{\mathrm{A}}\theta_* - k_{\mathrm{rev}}\theta_{\mathrm{A}}, \tag{3.47}$$

where

$$k_{\mathrm{ads}} = \frac{D_{\mathrm{A}}A_{\mathrm{site}}\rho_{\mathrm{A}}^{\circ}}{\theta_* L} \tag{3.48}$$

$$k_{\mathrm{des}} = \frac{D_{\mathrm{A}}A_{\mathrm{site}}\rho_{\mathrm{A}}^{\circ}}{K_{\mathrm{eq}}\theta_* L}. \tag{3.49}$$

An illustration of this model can be seen in figure 3.1.

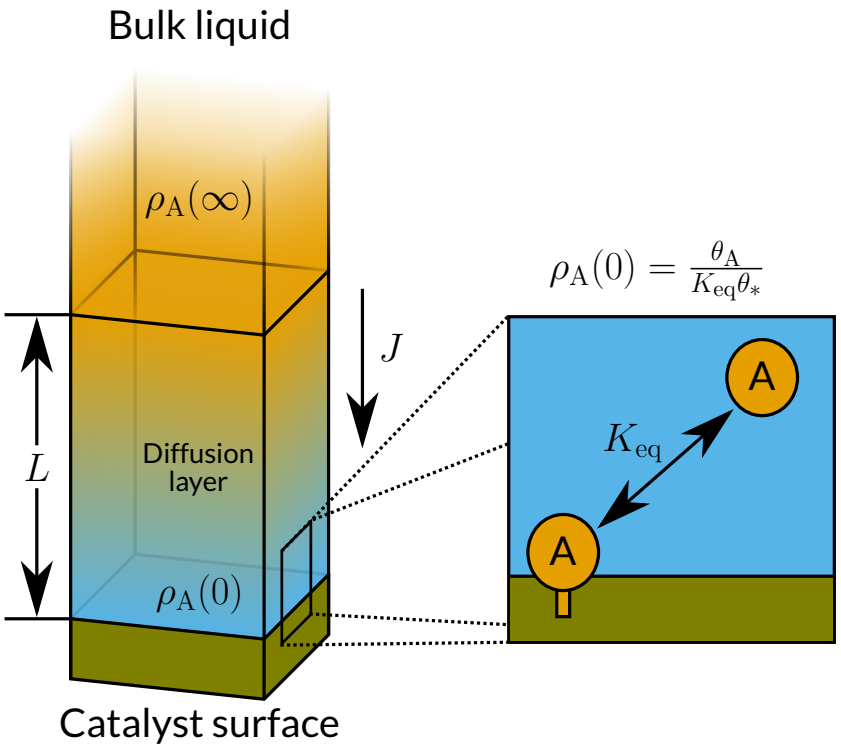

Figure 3.1: Schematic illustration of diffusion-limited adsorption model. Species A is represented by the color orange, and solvent (i.e. methanol) is represented by the color blue. L is the diffusive layer thickness, $\rho_A(\infty)$ is the concentration of species A in the bulk solution, $\rho_A(0)$ is the concentration of species A in the layer of solution that is in direct contact with the catalyst surface, J is the net flux of species A towards the catalyst surface, K_{eq} is the equilibrium constant for the adsorption of species A to the catalyst surface, θ_A is the coverage of species A on the catalyst surface, and θ_* is the fractional number of unoccupied sites on the catalyst surface.

Practically, due to the factors of θ_* and K_{eq} in the denominator of equations 3.48 and 3.49, these expressions can occasionally result in unphysically fast adsorption and desorption rates. In those cases, the adsorption and desorption process is no longer diffusion-limited, and the original assumption that an infinitely thin layer of solution is in equilibrium with the catalyst surface no longer holds. In that case, it becomes necessary

to approximate the rate at which the adsorbate detaches from the catalyst surface using transition state theory. If no desorption transition state can be found, the rate constant can be approximated as $\frac{1}{\beta h}$.

This model is similar to but distinct from one developed by Hansen, Viswanathan, and Nørskov for investigation of the electrocatalytic reduction of oxygen.[75] In their model, the rate of adsorption of O_2 is chosen to match experimental diffusion-limited electrode currents, and the reverse rate is chosen to obey detailed balance. In our model, we provide an approximate value for the diffusion layer thickness L (in their work, δ), and we assume that species in solution near the catalyst surface are in equilibrium with their adsorbed state.

3.4 Lateral interactions

The mean field approximation used in microkinetic modeling typically fails to accurately represent realistic catalyst surfaces due to the inability to represent interactions between adsorbates. It is therefore common to include an effective description of these lateral interactions within the mean field approximation.

Lateral interactions can be incorporated into the Helmholtz free energy through a many-body expansion,

$$F = F^{\circ} + \sum_i \sum_{j>i} \frac{N_i N_j}{M} E_{ij} + \dots, \tag{3.50}$$

where F° is the free energy of the system without consideration of lateral interactions and E_{ij} is the second-order lateral interaction energy between species i and j. This gives rise to a chemical potential of the form

$$\mu_i = \frac{dF}{dN_i} = \mu_i^{\circ} + 2\theta_i E_{ii} + \sum_{j \neq i} \theta_j E_{ij} + \dots \tag{3.51}$$

In this expression, μ_i^0 is the chemical potential of species i neglecting lateral interactions. Note that this expression is not consistent with the partition function described by equation 3.11, which contains no energetic cross-terms between adsorbates. Consequently, we introduce terms to the partition function that correspond to the terms of the many body

expansion of the free energy,

$$Q_{ij\ldots} = e^{-\beta E_{ij\ldots}}. \tag{3.52}$$

This allows us to write the partition function as

$$Q = \frac{M!}{N_*!}\left(\prod_i^{\text{fluid}} \frac{Q_i^{N_i}}{N_i!}\right)\left(\prod_i^{\text{adsorbate}} \left(\frac{\sigma_i Q_i}{M^{s_i-1}}\right)^{N_i} \frac{1}{N_i!}\right)\left(\prod_i^{\text{adsorbate}} \prod_{j>i}^{\text{adsorbate}} Q_{ij}^{N_i N_j/M}\right)\ldots \tag{3.53}$$

We obtain from this partition function an expression of the chemical potential that is identical to equation 3.51, where

$$\mu_i^\circ = -\frac{1}{\beta}\ln\left(\frac{\theta_*^{s_i}\sigma_i Q_i}{\theta_i}\right), \tag{3.54}$$

which is identical to the expression for the chemical potential without lateral interactions as presented in equation 3.12.

One important implication of this result is that lateral interactions must be symmetric to ensure thermodynamic consistency. For example, if species i is destabilized by species j,

$$\mu_i = \mu_i^0 + \theta_j E_{ij}, \tag{3.55}$$

then species j must also be destabilized by species i,

$$\mu_j = \mu_j^0 + \theta_i E_{ij}. \tag{3.56}$$

In practice, only a few species will typically dominate the bulk of the catalyst surface, so binding energy dependence on the coverage of minority species can frequently be ignored.

These coverage-dependent interaction energies can be obtained from a series of electronic structure theory calculations at varying coverages of the coadsorbates. However, this approach is not feasible for transition states due to the technical difficulty of optimizing to saddle points on the potential energy surface and the large number of calculations that must be performed to calculate lateral interaction energies. One approach to determining the lateral interaction energies of transition states is to use the Brønsted-Evans-Polanyi

(BEP) principle and estimate the lateral interactions of the transition state from the lateral interactions of the minima it connects. The BEP principle states that the free energy barrier of a class of similar reactions is correlated to the free energy of the reaction,

$$\Delta F^{\ddagger} = \alpha \Delta F + \beta, \tag{3.57}$$

where $\Delta F^{\ddagger}$ is the reaction activation free energy, α is a parameter that characterizes the lateness of the reaction, and β is the activation free energy corresponding to a thermoneutral reaction. If α is known, it can be used to approximate the lateral interactions of the transition state as a linear combination of the reactant and product lateral interactions,

$$\Delta E^{\ddagger} = (1 - \alpha)\Delta E_R + \alpha \Delta E_P, \tag{3.58}$$

where

$$\Delta E_i = 2\theta_i E_{ii} + \sum_{j \neq i} \theta_j E_{ij} + \ldots \tag{3.59}$$

is the the correction to the energy of species i due to lateral interactions.

In catalyst screening studies, the BEP principle is used to bypass the need to perform costly transition state searches for every potential catalyst of interest by fitting α and β to explicitly determined free energy barriers and reaction free energies for a small number of catalysts. This approach is not feasible for our use case, as α needs to be known for every reaction with a transition state in the model, which means that many such fits must be performed. Instead, α can be approximated by the forward and reverse activation free energy barriers,

$$\alpha \approx \frac{\Delta F^{\ddagger}_{\text{for}}}{\Delta F^{\ddagger}_{\text{for}} + \Delta F^{\ddagger}_{\text{rev}}}. \tag{3.60}$$

Note that the lateness α depends on the forward and reverse free energy barriers, which in turn depend on α. Therefore, equations 3.58 and 3.60 must be solved self-consistently.

3.5 Adsorption of charged species

Adsorption of ions to the catalyst surface will result in a buildup of charge that is screened by counterions in solution. For metal catalysts, anions will typically deposit their excess electron into the catalyst, depending on the relative energetics of the catalyst's Fermi level and the electron affinity of the adsorbed neutral species. The resulting charge will be delocalized over the entire catalyst, which can be treated as an electrolytic capacitor.

The differential energy of charging a capacitor is

$$dE_{\text{cap}} = V dq \tag{3.61}$$

$$= \left(\frac{q}{C} - \frac{\Phi}{e} \right) dq, \tag{3.62}$$

where V is the voltage between the catalyst surface and the vacuum, C is the absolute capacitance, q is the *excess* charge on the capacitor, Φ is the work function of the catalyst, and e is the elementary electron charge. We choose the reference of potential to be the vacuum to allow for easier comparison to the electron affinities and ionization energies of molecules, which are easily calculated with respect to the vacuum level in electronic structure theory. The term $\frac{q}{C}$ gives the voltage difference between the charged catalyst and an uncharged but otherwise identical catalyst, while Φ is the work required to remove an electron from the catalyst and put it in the vacuum.

From equation 3.62, we can derive the chemical potential of an electron on the catalyst as

$$\mu_{\text{e}^-} = \frac{dF}{dN_{\text{e}^-}} \tag{3.63}$$

$$= \frac{dE_{\text{cap}}}{dN_{\text{e}^-}} - T\frac{dS}{dN_{\text{e}^-}} \tag{3.64}$$

$$= \left(\frac{q}{C} - \frac{\Phi}{e} \right) \frac{dq}{dN_{\text{e}^-}} \tag{3.65}$$

$$= \frac{e^2}{C} N_{\text{e}^-} - \Phi, \tag{3.66}$$

where $\frac{dS}{dN_{\text{e}^-}} = 0$, as charging and discharging an ideal capacitor releases no heat. Here, C

refers to the capacitance of the entire catalyst. In experimental studies, the capacitance of an electrode is typically reported in the areal capacitance

$$C_a = \frac{C}{A}, \tag{3.67}$$

where A is the area of the entire catalyst. Using our previously defined terminology, $A = MA_{\text{site}}$, where M is the total number of adsorption sites on the catalyst and A_{site} is the area of a single site. This allows chemical potential of the electron to be rewritten as

$$\mu_{e^-} = \frac{e^2}{C_a A_{\text{site}}} \theta_{e^-} - \Phi \tag{3.68}$$

$$= \Delta E_{\text{cap}} \theta_{e^-} - \Phi, \tag{3.69}$$

where $\theta_{e^-} = N_{e^-}/M$ is the number of excess electrons on the catalyst per adsorption site.

4 MICKI: A MICROKINETIC MODELING PACKAGE WRITTEN IN PYTHON

4.1 Motivation

Microkinetic modeling has become a common tool used by experimentalists and theorists to help explain the underlying mechanistic origin of experimental observations. Microkinetic models also have the ability to access reaction conditions beyond those measured experimentally. The experimental approach to microkinetic modeling was detailed in the seminal book "The Microkinetics of Heterogeneous Catalysis" by James Dumesic.[72] As originally conceived, plausible catalytic reaction mechanisms must be proposed ahead of time, and the thermodynamic and kinetic parameters of the model are then fitted to experimental measurements, such as reaction rates and rate orders. Over time, the improvement of theoretical methods such as DFT and the increase in access to computational resources have made it possible to identify plausible mechanisms and to estimate thermodynamic and kinetic model parameters without the need to perform any experimental measurements at all.

While theory has found extensive use in conjunction with experimental measurements to study the properties of heterogeneous catalysts, microkinetic models using only theoretical calculations without semi-empirical parameter fitting typically fail to accurately reproduce experimental findings. Furthermore, the scope of theoretically motivated microkinetic models has largely been limited to high-temperature catalysis at solid–vacuum interfaces, where standard approaches such as the ideal gas approximation and collision theory are most accurate. In particular, microkinetic modeling at the solid-liquid interface is little-explored, with only a few theoretical studies addressing the complications of solution-phase catalysis arising from slow mass transport and the thermodynamics of solvation.

Even more troubling is the low number of publicly-available code to perform microkinetic modeling simulations. Of the publicly-available microkinetic modeling packages, most are designed with a particular application such as catalyst screening in mind, and

are therefore insufficiently general for the purpose of studying complex systems and developing novel methodology.[76] As solution of a microkinetic model can be ultimately reduced to the problem of solving a system of differential equations, many studies forgo the use of microkinetic modeling packages altogether, instead relying on custom-written Matlab or Python scripts which explicitly invoke the underlying differential equation solver. This approach, while perfectly sound mathematically, fails to create a clear distinction between the high-level view of a microkinetic model — as comprising reactions between chemical species — from the low-level view — as merely a system of differential equations. This unfortunate conceptual entanglement between the chemistry and the math makes it difficult to develop, use, modify, and teach microkinetic modeling.

The lack of a high-level general program for microkinetic modeling motivated us to develop our own code, named Micki. Micki is designed to be general, easy to use, powerful, and efficient. Micki is an object-oriented code that is designed around analogies to chemical concepts such as reactants, reactions, energies, entropies, and so on. The code is modular, which allows new methods to be easily prototyped and added to the program by modifying only the relevant parts. Because Micki uses symbolic expressions to represent reaction rates, it is possible to introduce lateral interactions and other modifications to model parameters of arbitrary functional form. Since Micki is fast, it is capable of performing many simulations under varying initial conditions or with varying model parameters. This enables Micki to rapidly perform sensitivity analysis on all parameters of a model, which can be used to fit these parameters to experimental observations.

Throughout the rest of this chapter, we will use the water-gas shift (WGS) reaction on Pt(111) as an example of how to use Micki. The model developed in this chapter parallels that of Grabow et. al., using a subset of the plausible elementary steps proposed in their work.[77]

4.2 Creating the input file

As it is currently designed, Micki expects the user to have prepared electronic structure calculations and vibrational frequency analysis for all minima and transition states. Currently, Micki is only capable of reading the `vasprun.xml` or `OUTCAR` files generated

by VASP. However, as Micki relies on the Python environment ASE to read and store the results of electronic structure theory calculations, in theory any format supported by ASE can be made compatible with Micki.

```
#!/usr/bin/env python

from micki import Adsorbate, Gas
from ase.io import read
from ase.db import connect

sp = {}
sp['co_g'] = Gas('co_g/freq/vasprun.xml', label='co_g', freqs=None, symm=1, spin=0., eref=None, rhoref=1., dE=0.)
sp['h2o_g'] = Gas('h2o_g/freq/vasprun.xml', label='h2o_g', symm=2)
sp['co2_g'] = Gas('co2_g/freq/vasprun.xml', label='co2_g', symm=2)
sp['h2_g'] = Gas('h2_g/freq/vasprun.xml', label='h2_g', symm=2)


sp['slab'] = Adsorbate(read('pt/vasprun.xml'), label='slab', freqs=[], ts=False, spin=0., sites=[], lattice=None, eref=None, dE=0., symm=1)
sp['co'] = Adsorbate('co/freq/vasprun.xml', label='co', freqs=None, ts=False, spin=0., sites=[sp['slab']], lattice=None, eref=None, dE=0., symm=1)
sp['h2o'] = Adsorbate('h2o/freq/vasprun.xml', label='h2o', sites=[sp['slab']])
sp['oh'] = Adsorbate('oh/freq/vasprun.xml', label='oh', sites=[sp['slab']])
sp['o'] = Adsorbate('o/freq/vasprun.xml', label='o', sites=[sp['slab']])
sp['h'] = Adsorbate('h/freq/vasprun.xml', label='h', sites=[sp['slab']])
sp['cooh'] = Adsorbate('cooh/freq/vasprun.xml', label='cooh', sites=[sp['slab']])

sp['ho-h'] = Adsorbate('ho-h/freq/vasprun.xml', label='ho-h', sites=[sp['slab'], sp['slab']], symm=2, ts=True)
```

```
23 sp['o-h'] = Adsorbate('o-h/freq/vasprun.xml', label='o-h',
   ↪  sites=[sp['slab'], sp['slab']], ts=True)
24 sp['o-co'] = Adsorbate('o-co/freq/vasprun.xml', label='o-co',
   ↪  sites=[sp['slab'], sp['slab']], ts=True)
25 sp['co-oh'] = Adsorbate('co-oh/freq/vasprun.xml', label='co-oh',
   ↪  sites=[sp['slab'], sp['slab']], ts=True)
26 sp['oco-h'] = Adsorbate('oco-h/freq/vasprun.xml', label='oco-h',
   ↪  sites=[sp['slab'], sp['slab']], ts=True)
27
28 with connect('my_micki_db.json') as con:
29     for name, species in sp.items():
30         species.save_to_db(con)
```

Listing 4.1: An example of how to read in the output files from VASP frequency calculations.

Listing 4.1 illustrates how to read in the output files from VASP frequency calculations. Line 8 illustrates all options available to the `Gas` class, which calculates the free energy of a species under the ideal gas approximation. For lines 9 through 11, arguments corresponding to the default settings have been omitted. Rather than explicitly passing the vibrational frequencies to the `Gas` class, these vibrational frequencies are automatically determined by diagonalizing the Hessian matrix contained within the `vasprun.xml` output file.

Beginning on line 14, species corresponding to adsorbates on the surface are read in, starting with the bare slab itself. The `Adsorbate` class treats all adsorbate degrees of freedom under the harmonic oscillator approximation. For the bare slab, we use the `read` method from ASE and explicitly pass an empty list of frequencies, as we do not consider the motion of metal atoms in our vibrational frequency analysis. The `Adsorbate` class takes an additional argument, `sites`, which is used to ensure proper site balancing when writing reactions by specifying the object or objects corresponding to the bare site or sites to which the adsorbate is bound. Lines 22 through 26 read in the frequency calculations for transition states. Other than the `ts=True` argument, this is identical to how reaction intermediates are read in.

On lines 28 through 30, the thermodynamic objects that have been created are saved

to an ASE database file. The database file can be read in with a later script that runs the microkinetic model. With the exception of the `dE` argument, all other settings are saved in the `data` field of the ASE database. Using an ASE database to store the species of a microkinetic model not only speeds up the process of running the microkinetic model itself, it also allows one to quickly inspect and analyze the species themselves using normal ASE utilities.

```
#!/usr/bin/env python

from micki.db import read_from_db
from micki import Reaction, Model
from ase.units import m, _k, _Nav

sp = read_from_db('my_micki_db.json', eref=['slab', 'co_g', 'h2o_g',
↪  'h2_g'])

sp['co'].dE = 0.09496182099234107  # Shift to match experiment binding
↪  enthalpy
sp['oh'].dE = -0.225  # Shift to match experimental TOFs

sp['co'].coverage = 2*0.784423808 * sp['co'].symbol

sp['o'].coverage = 1.147079243 * sp['co'].symbol + 2*1.11913902 *
↪  sp['o'].symbol
sp['o'].dE = -0.12434878
sp['co'].coverage += 1.147079243 * sp['o'].symbol

sp['h'].coverage = 0.237728186 * sp['co'].symbol
sp['co'].coverage += 0.237728186 * sp['h'].symbol

sp['h2o'].coverage = 0.10555879 * sp['co'].symbol
sp['co'].coverage += 0.10555879 * sp['h2o'].symbol

sp['oh'].coverage = 0.263160274 * sp['co'].symbol
sp['co'].coverage += 0.263160274 * sp['oh'].symbol

```

```
27 sp['cooh'].coverage = 1.901900269 * sp['co'].symbol
28 sp['co'].coverage += 1.901900269 * sp['cooh'].symbol
```

Listing 4.2: An example script showing how to read in the database and set lateral interaction parameters.

Listing 4.2 illustrates the beginning of a new script in which the previously-created database is read in. On line 7, the dictionary of thermodynamic objects is recreated from the database, and the energies of all species are shifted so as to set the energies of the defined species to 0 while maintaining all relative energies. The `eref` argument must have as many species as there are unique atom types. If `eref` is passed the elemental form of each atom (e.g. graphite for carbon, dioxygen gas for oxygen, etc.), then the energy of each species in `sp` is its *formation* energy.

On lines 9 and 10, the energy of adsorbed CO and OH are shifted to match experiment. Starting on line 12, the lateral interaction energies between adsorbates are defined. Each thermodynamic object has a corresponding `symbol` attribute, which is a `sympy` symbol object corresponding to the coverage of that species in the model. Lateral interactions are defined as symbolic expressions which modulate the energy according to the instantaneous coverage of the species in the model. Here, lateral interactions are all linear functions of species coverages, but in general this can be any well-behaved expression. Thermodynamic balance is ensured by making all lateral interactions symmetric between species (for example, compare lines 18 and 19). The constant shift in energy of adsorbed O on line 15 reflects the zero-coverage limit arising from lateral O-O self-interactions.

```
1 rxns = {'co_ads': Reaction(sp['co_g'], sp['co'], method='CT'),
2         'h2o_ads': Reaction(sp['h2o_g'], sp['h2o'], method='CT'),
3         'h2_ads': Reaction(sp['h2_g'], 2*sp['h'], method='CT'),
4         'ho-h': Reaction(sp['h2o'], sp['oh'] + sp['h'], ts=sp['ho-h']),
5         'o-h': Reaction(sp['oh'], sp['o'] + sp['h'], ts=sp['o-h']),
6         'o-h-oh': Reaction(2*sp['oh'], sp['o'] + sp['h2o'],
          ↪  method='DIEQUIL'),
7         'o-co': Reaction(sp['o'] + sp['co'], sp['co2_g'],
          ↪  ts=sp['o-co']),
8         'co-oh': Reaction(sp['cooh'], sp['co'] + sp['oh'],
          ↪  ts=sp['co-oh']),
```

```
9           'oco-h': Reaction(sp['cooh'] + sp['slab'], sp['co2_g'] +
            ↪  sp['h'], ts=sp['oco-h']),
10          'oco-h-o': Reaction(sp['cooh'] + sp['o'], sp['co2_g'] +
            ↪  sp['oh'], method='EQUIL'),
11          'oco-h-oh': Reaction(sp['cooh'] + sp['oh'], sp['co2_g'] +
            ↪  sp['h2o'], method='EQUIL'),
12          }
13
14  Asite = np.sqrt(3) * 3.8966**2 / (4 * m**2)  # area per site, in m^2
15  T = 548  # temperature, in Kelvin
16  atm2molar = 101325 / _k / T / _Nav / 1000.
17
18  model = Model(T, Asite, reactor='CSTR')
19  model.lattice = {sp['slab']: {sp['slab']: 6}}
20  model.add_reactions(rxns)
21  model.set_fixed(['co_g', 'h2o_g', 'h2_g', 'co2_g'])
22
23  U0 = {'co_g': 0.145 * atm2molar,
24        'h2o_g': 0.208 * atm2molar,
25        }
26
27  model.set_initial_conditions(U0)
28  t1, U1, r1 = model.find_steady_state()
```

Listing 4.3: An example script illustrating how to set up and run a simple CSTR reactor model.

Listing 4.3 contains the second half of the script beginning with listing 4.2. It begins by defining all reactions considered in this model. The rate of adsorption reactions are approximated using collision theory, which is selected with the `method='CT'` flag. The rates of reactions for which a transition state is known are approximated using transition state theory, which is selected by passing the thermodynamic object corresponding to the transition state to the `Reaction` class. For reactions that do not have a transition state, the argument `method='EQUIL'` will cause Micki to approximate the rate constant in the exothermic direction as $(\beta h)^{-1}$, which is equivalent to transition state theory where the side of the reaction with the higher energy is the transition state. For some reactions,

lateral interactions can cause the reaction to change between exothermic and endothermic depending on reaction conditions. In that case, `method='DIEQUIL'` can be used, which calculates the rate constants as

$$k_{\text{for}} = \frac{1}{\beta h}\left(\frac{K_{\text{eq}}}{1 + K_{\text{eq}}}\right) \tag{4.1}$$

$$k_{\text{rev}} = \frac{1}{\beta h}\left(\frac{1}{1 + K_{\text{eq}}}\right). \tag{4.2}$$

When $K_{\text{eq}} \ll 1$ or $K_{\text{eq}} \gg 1$, this expression reduces to the same approximation as used with `method='EQUIL'`, and this prevents unphysically fast rate constants from arising due to changes in reaction conditions.

On lines 14 and 15, some model parameters are defined. The area per adsorption site is necessary to determine the rate of adsorption under collision theory, while the temperature is needed to calculate equilibrium constants and rate constants. The model is created on line 18. On line 19, the geometry of the catalyst surface is defined by specifying the number of nearest neighbors for each kind of site included in the model. The first `sp['slab']` term identifies the site for which we are interested in determining its nearest neighbors, while the second `sp['slab']` indicates the type of sites that are neighboring the initial site. Since this example considers a simple FCC(111) surface, there is only one type of site, each of which has 6 nearest neighbors. The reactions are added to the model on line 20, and the concentrations of gas-phase species are fixed on line 21 in order to model a simplified continuous stirred tank reactor (CSTR).

The initial conditions of the reactor are defined on line 23. Any species whose initial concentration is not specified is assumed to have an initial concentration of 0, with the exception of lattice empty sites, which is chosen such that the sum of all adsorbates and empty sites is equal to 1. Upon setting the initial conditions in line 27, Micki sets up, compiles, and imports the Fortran module for solving the differential equations. The `find_steady_state` method called on line 28 then runs this code in order to find the steady state concentrations, which it returns along with the time to reach the steady state and the steady state rates for each reaction in the model.

In addition to the `find_steady_state` method, Micki provides a `solve` method

for explicitly integrating the microkinetic model for a specified time range. This method returns a list of concentrations and reaction rates at the requested number of time points over the requested time range.

```
tfinal = 3600  # target time, in seconds
nt = 100  # number of time points to return results
U, r = model.solve(tfinal, nt)
```

4.3 Output and analysis

The `find_steady_state method` returns three results, `t1`, `U1`, and `r1`. The first result, `t1`, contains the time at which the concentrations were found to no longer change, which is the approximate time to reach the steady state condition. The steady state concentrations are contained in the dictionary `U1`. The keys of `U1` are the string labels assigned to each species, and the values are the coverages for adsorbates and the concentration in M for fluids.

```
>>> U1
{'co_g': 0.0032245566792141493,
 'h2o_g': 0.004625570960527883,
 'co2_g': 0.0,
 'h2_g': 0.0,
 'co': 0.43947084233850309,
 'h2o': 2.1928718244395932e-05,
 'oh': 7.2657882494752563e-09,
 'o': 1.1358480191111262e-13,
 'h': 0.00012449998908308475,
 'cooh': 7.3517941630753175e-11,
 'slab': 0.56038272161474967}
```

The final result, `r1`, contains the rates of each reaction under steady state conditions. The keys of `r1` are the string labels assigned to each reaction, and the values are the net reaction rates under steady state conditions.

```
>>> r1
{'co_ads': 2.8439046815037727,
```

```
'h2o_ads': 2.843904685229063,
'ho-h': 2.8439457909648813,
'co-oh': -2.843869614901338,
'oco-h': 2.8438635154533385,
'h2_ads': -2.8439046807493704,
'o-h-oh': 3.5010862861137296e-05,
'o-co': 3.5065848033855484e-05,
'o-h': 5.5080522835581964e-08,
'oco-h-o': 9.535011737847916e-11,
'oco-h-oh': 6.0993526491052549e-06}
```

The `U` returned by the `solve` method is a list containing the concentrations of the species in the model at each requested time point. Each entry in the list is formatted identically to the `U1` result returned by the `find_steady_state` method. Analogously, `r` is a list containing the instantaneous reaction rates at each requested time point.

One frequently wishes to know which parameters of a microkinetic model are most important for the properties of interest, such as turnover frequency or selectivity. Sensitivity analysis is a commonly used technique for determining the relative importance of a model's parameters.[78–80] The degree of rate control is a metric originally formulated by Campbell which measures the sensitivity of some output parameter to the rate constants of a particular reaction step,

$$\chi_{\mathrm{RC},i} = \frac{k_i}{P} \left.\frac{dP}{dk_i}\right|_{k_{j\neq i},K_{\mathrm{eq}}}, \tag{4.3}$$

where P is some output of the model such as a turnover frequency, and k_i refers to both the forwards and reverse rate constants for step i. Similarly, the degree of thermodynamic rate control measures the sensitivity of some model output to the energy of a reaction intermediate,

$$\chi_{\mathrm{TRC},n} = -\frac{1}{\beta P} \left.\frac{dP}{dF_n^\circ}\right|_{F_{m\neq n}^\circ,F_i^{\ddagger\circ}}, \tag{4.4}$$

where F_n° is the free energy of species n, and $F_i^{\ddagger\circ}$ refers to the free energy of the transition state corresponding to reaction step i.

Micki provides the user the ability to explicitly perturb the binding energies of reaction intermediates and transition states. Furthermore, Micki provides an interface for

scaling the rates of individual reaction steps and the energy, entropy, or free energy of intermediates and transition states by a constant factor. This flexibility allows the user to quickly and easily perform the numerical derivatives necessary to calculates χ_{RC} or χ_{TRC}.

```
chi_rc = {}
rmid = r1['co_ads']  # as a proxy for CO2 production
scale = 0.001
for rname, rxn in rxns.items():
    rxn.set_scale('kfor', 1 - scale)
    rxn.set_scale('krev', 1 - scale)
    model.set_initial_conditions(U1)
    t2, U2, r2 = model.find_steady_state()
    rlow = r2['co_ads']

    rxn.set_scale('kfor', 1 + scale)
    rxn.set_scale('krev', 1 + scale)
    model.set_initial_conditions(U1)
    t3, U3, r3 = model.find_steady_state()
    rhigh = r3['co_ads']

    rxn.set_scale('kfor', 1)
    rxn.set_scale('krev', 1)

    chi_rc[rname] = (rhigh - rlow) / (2 * scale * rmid)
```

Listing 4.4: An example script illustrating how to calculate Campbell's degree of rate control.

As an example, consider the target property of interest to be the rate of formation of CO_2 under steady state conditions in the water–gas shift reaction we have used as an example. The degree of rate control for each reaction can be easily calculated, as illustrated in listing 4.4. Similarly, a script illustrating how to calculate the degree of thermodynamic rate control for each species in the model is illustrated in listing 4.5.

Note that as implemented in listing 4.5, the degree of thermodynamic rate control that is calculated is not identical to its original definition as formulated by Campbell. Specifically, Micki explicitly accounts for the correlation between the energy of a transition state with its adjoining minima through an approximate Brønsted–Evans–Polanyi-type relationship as outlined in section 3.4. Consequently, perturbations to adsorbate energies

```
from ase.units import kB
from micki import Adsorbate

chi_trc = {}
rmid = r1['co_ads']  # as a proxy for CO2 production
scale = 0.001
dE = scale * kB * T
for name, species in sp.items()
    # only calculate chi_trc for adsorbed minima
    if (not isinstance(species, Adsorbate)
            or species.ts
            or name == 'slab'):
        continue

    species.dE -= dE
    for _, rxn in rxns.items():
        rxn.update(T=T, Asite=Asite, force=True)
    model.set_initial_conditions(U1)
    t2, U2, r2 = model.find_steady_state()
    rlow = r2['co_ads']

    species.dE += 2*dE
    for _, rxn in rxns.items():
        rxn.update(T=T, Asite=Asite, force=True)
    model.set_initial_conditions(U1)
    t3, U3, r3 = model.find_steady_state()
    rhigh = r3['co_ads']

    species.dE -= dE

    chi_trc[name] = (rlow - rhigh) / (rmid * scale)
```

Listing 4.5: An example script illustrating how to calculate Campbell's degree of thermodynamic rate control.

will also affect the binding energy of transition states, and thereby the forward and reverse rates of reactions involving that adsorbate.

```
rate_order = {}
rmid = r1['co_ads']  # as a proxy for CO2 production
drho = 5e-5
for name in ['co_g', 'h2o_g']:
```

```
    species = sp[name]
    rhomid = U0[name]

    U0_new = U0.copy()
    U0_new[name] -= drho
    model.set_initial_conditions(U0_new)
    t2, U2, r2 = model.find_steady_state()
    rlow = r2['co_ads']

    U0_new[name] += 2*drho
    model.set_initial_conditions(U0_new)
    t3, U3, r3 = model.find_steady_state()
    rhigh = r3['co_ads']

    rate_order[name] = rhomid * (rhigh - rlow) / (2 * drho * rmid)
```

Listing 4.6: An example script illustrating how to calculate the rate order of reactants.

```
from ase.units import kB

rmid = r1['co_ads']  # as a proxy for CO2 production
dT = 0.01

model.T = T - dT
model.set_initial_conditions(U1)
t2, U2, r2 = model.find_steady_state()
rlow = r2['co_ads']

model.T = T + dT
model.set_initial_conditions(U1)
t3, U3, r3 = model.find_steady_state()
rhigh = r3['co_ads']

model.T = T
Ea = kB * T**2 * (rhigh - rlow) / (2 * rmid * dT)
```

Listing 4.7: An example script illustrating how to calculate the effective activation energy of a model.

It is also possible to calculate the rate order of a particular reactant by numerically perturbing its initial concentration. An example script illustrating how this can be done is presented in listing 4.6. As a final example, the effective activation energy for the formation of a particular product can be calculated by numerically perturbing the temperature of the model, as illustrated in listing 4.7.

4.4 More advanced techniques

As Micki is designed to be fully scriptable in an object oriented fashion, it is possible to perform complex simulations of the reaction network. For example, it is possible to simulate simplified CSTR and batch reactors by fixing particular species in the model prior to solution. A more complex type of reactor to simulate is the plug flow reactor (PFR), which has both spatial and temporal dimensions. For a PFR, one is typically most interested in the steady state solution, which is achieved after a sufficient amount of time has passed. It is possible to reduce the two-dimensional PFR to a one-dimensional system of differential algebraic equations in the steady state by assigning the coverages of adsorbates as algebraic variables and using the steady state of a CSTR as the initial conditions.

```
nsites = 47e-6 * 0.1501  # number of active sites, in moles
flow = 101.4  # flow rate, in mL/min
dt = 60 * 1000 * nsites / flow

pfr = Model(T, Asite, reactor='PFR')
pfr.lattice = model.lattice
pfr.add_reactions(rxns)
pfr.set_initial_condition(U1)
U1pfr, r1pfr = pfr.solve(dt, 1000)
tof = (U1pfr[-1]['co2_g'] - U1['co2_g']) * flow / (1000 * nsites)
```

Listing 4.8: An example script illustrating how to simulate a PFR. This script continues from 4.2 and 4.3.

Listing 4.8 is an illustration of how to simulate a PFR for a reaction with a known number of catalytically active sites and a predetermined flow rate. The argument `reactor='PFR'` indicates to Micki that the variables in the DAE corresponding to adsorbate coverages are to be treated algebraically. Algebraic variables are solved according to the traditional ODE expression

$$\frac{dX}{dt} = f(X), \tag{4.5}$$

whereas algebraic equations are rigorously enforced to be equal to 0 at all time points,

$$0 = f(X). \tag{4.6}$$

By starting from the steady-state solution of the CSTR and assigning adsorbate variables as algebraic, we ensure that the surface and its adsorbate coverages are in equilibrium for all time points. We then explicitly solve over a time `dt`, which depends on the number of active sites and the flow rate.

The integration time is related to the volume of the reactor and the flow rate,

$$\Delta t = \frac{V}{Q}, \tag{4.7}$$

where Q is the volumetric flow rate. As the volume of the reactor is not well defined, we must make an arbitrary choice. Internally, Micki stores all variables in terms of number of molecules relative to the number of active sites. This is equivalent to having a concentration of 1 M active sites, as fluid-phase concentrations are stored in units of M. This results in a reactor volume of

$$V = \frac{M}{\rho_*}, \tag{4.8}$$

where M is the number of active sites and $\rho_* = 1\,\mathrm{M}$ is the concentration of active sites. This results in an integration time of

$$\Delta t = \frac{M}{Q\rho_*}. \tag{4.9}$$

The concentration of solution-phase species at the end of the simulation is its concentration

flowing out of the reactor.

5 DECOUPLING THE ELECTRONIC, GEOMETRIC, AND INTERFACIAL CONTRIBUTIONS TO SUPPORT EFFECTS IN HETEROGENEOUS CATALYSIS

This chapter is adapted from Hermes, E. D.; Jenness, G. R.; Schmidt, J.R. Decoupling the Electronic, Geometric, and Interfacial Contributions to Support Effects in Heterogeneous Catalysis. *Mol. Simul.* **2015**, *41*, 123–133.[81]

5.1 Motivation

As discussed in chapter 1, real heterogeneous catalysts typically comprise polydisperse transition metal particles supported on inexpensive high-surface-area material. It is commonly assumed that the role of the support is merely to disperse the catalyst itself, however the choice of support material can have a large impact on catalytic activity. For example, noble metal catalysts supported on mesoporous titania are known to become deactivated at high temperatures due to migration of support over the top of the metal catalyst.[82–95] This effect has been termed the strong metal–support interaction (SMSI).[21,22] The support can affect catalytic activity in more subtle ways as well, through electronic interactions with the metal catalyst,[82,83] by inducing geometrical or morphological changes in the metal catalyst, or through the creation of new kinds of active sites at the metal–support interface. The chemical properties of these new active sites may be modulated though ligand effects induced by the support,[32,34,96,97] or through simultaneous bonding of adsorbates to the metal and the support at the interface.[98–102] In some cases, it is known that the support material directly participates in catalytic activity itself, for example through hydrogen spillover or Mars–van Krevelen oxidation. The sum total of these effects (excluding the SMSI) have recently been termed the "electronic metal–support interaction".[82]

It is therefore important to consider the impact of support in theoretical studies of heterogeneous catalysis. Most computational investigations of heterogeneous catalysis

neglect support by modeling the catalyst with a small unit cell of a perfect crystal facet. This is due not only to the added computational expense arising from consideration of explicit support atoms, but also because supported catalyst systems have many chemically unique active sites. In a previous work, Jenness and Schmidt examined the thermodynamics of several Fischer–Tropsch reaction intermediates on a silica- and titania-supported Rh metal catalyst.[7,103,104] The computational model used in this work was based on existing experimental characterization of Rh metal catalysts, and this was used to deconvolute the effect of support on the geometric and electronic properties of the catalyst.[105–113] Reactions of this type may play a role in future green liquid fuel applications, as biomass gasification creates the chemical feedstock necessary to perform Fischer–Tropsch.[114] The primary difficulty with Fischer–Tropsch is the thermodynamic drive to form methane, while oxygenates such as ethanol or larger hydrocarbons such as octane are more valuable products. It has been shown that the selectivity of Fischer–Tropsch catalysts is affected by the choice of support material, with titania typically producing more valuable products than silica.[115–123]

In the previous work, Jenness and Schmidt did not consider adsorbate binding to the metal–support interface itself, nor did they consider simultaneous adsorbate binding to the metal and the support. This is particularly important for titania, which is known to form oxygen vacancies under typical synthetic conditions. These oxygen vacancies may strongly bind oxygen-containing adsorbates, particularly if they occur near the metal nanoparticle. There is experimental evidence that these metal–oxide interface sites do in fact play an important role in some catalytic applications.[98] As an example, Somorjai et. al. showed that the activity of Rh metal catalysts to the CO hydrogenation reaction was enhanced by the presence of sub-monolayer quantities of oxide material.[124] Another example that illustrates the importance of these interfacial sites is the oxidation of CO on Au metal catalysts supported on TiO_2. For this reaction, it was shown that dissociation of O_2 occurs primarily at the metal–support interface, as the Au catalyst itself is not able effect this reaction by itself. CO molecules adsorbed near to the interface further facilitate the cleavage of O_2, which in turn results in the formation of CO_2.[99]

In this work, we investigate the importance of the interfacial and dual-binding sites for the same system as was considered in our previous work. We begin by reviewing

the results presented in that work by comparing the geometric and electronic effects of silica and titania supports on the binding of Fischer–Tropsch intermediates, as well as the hydrogenated or hydroxylated variants of those supports. We then consider the effect of oxygen vacancies in the titania support on these thermodynamic properties, as the presence of oxygen vacancies affects the electronic properties of the support. We then investigate adsorbate binding geometries at the metal–support interface itself, and show that oxygen-containing species can become very strongly stabilized in these geometries, particularly when interacting with oxygen vacancies in the support. While the energetics of binding to interfacial sites will depend on the particular geometry of the metal–support system, we believe that the results present in this work illustrate a general phenomenon in which these interfacial sites provide unique chemical environments which may strongly impact overall catalyst activity.

5.2 Methods

We examined several models of oxide-supported Rh nanoparticles on either silica (SiO_2) or titania (TiO_2), two oxides frequently utilized as catalyst supports.[117,125–128] The nanoparticle was modeled as a hemispherical cluster of 37 Rh atoms arranged in a cuboctahedral shape (≈1.5 × 1.0 nm), with alternating (100) and (111) facets (see Figure 5.1). This shape is consistent with the corresponding experimentally observed oxide-supported Rh nanoparticles and the size lies within the measured distribution.[105–113,120,127,129–133] The SiO_2 surface was modeled as the (001) face of α-quartz, as this is the most energetically favorable surface of the most common silica polymorph.[134–136] The model consisted of 6 layers of a 4x4 supercell of the primitive unit cell. We also considered hydroxylated surface variants as may occur under reaction conditions due to water dissociation.[115,137] The hydroxylated (OH)(H)SiO_2 variant was generated by dissociatively adsorbing a monolayer of water onto the surface.[135,138,139] Although this is certainly a simplified model of a potentially complex hydroxylated silica surface, it provides a contrast to its bare (unhydroxylated) counterpart. The TiO_2 surface was modeled as the stable (110) face of rutile titania,[140] with 4 layers of a 3x7 supercell. The hydroxylated (H)TiO_2 variant, resulting from potential hydrogen spillover (under reaction conditions), was then generated by saturating all

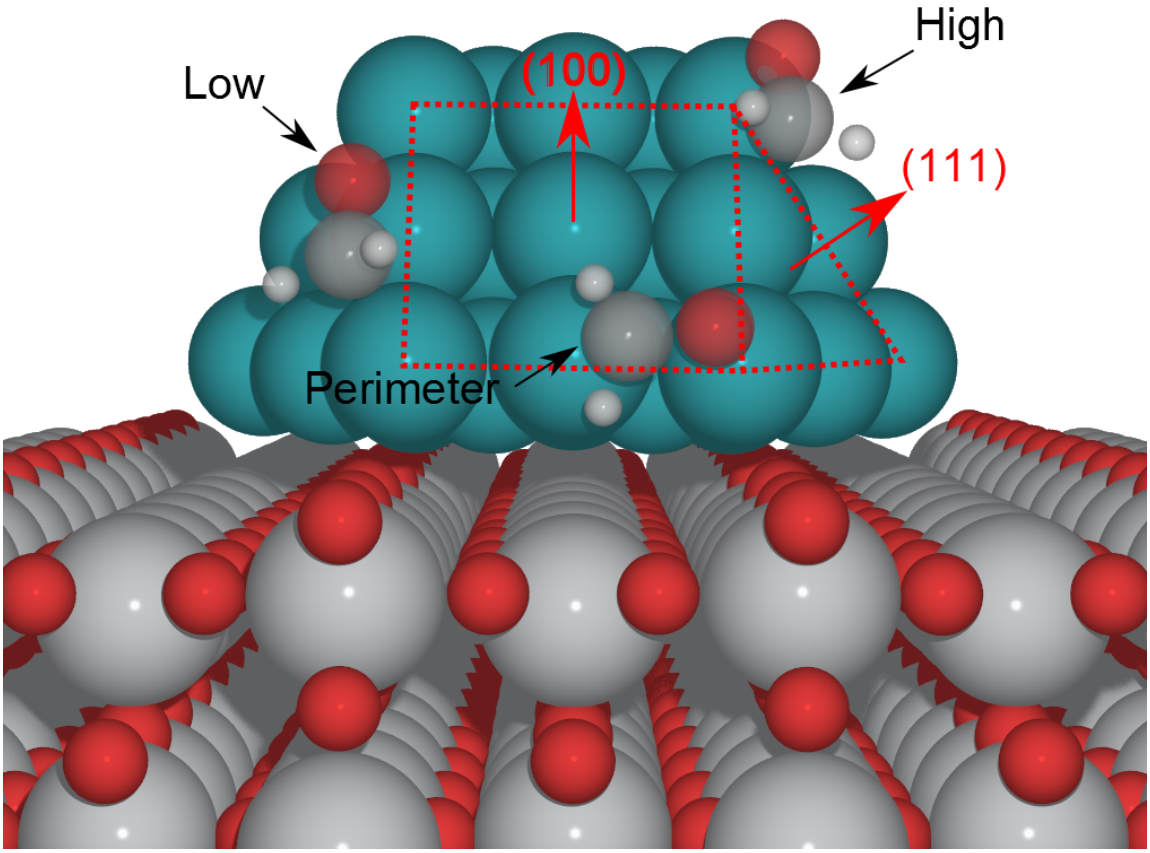

Figure 5.1: A schematic illustration showing three of the different binding sites examined in this study, as well as the nanoparticle's alternating (100) and (111) facets.

bridging oxygen atoms with hydrogen atoms.[92,140–144]

Unless otherwise noted we utilize 'rigid' nanoparticle geometries, where the nanoparticle is first fully relaxed in the gas phase and then deposited in a fixed geometry on the silica and titania surfaces to produce a supported nanoparticle system. The adsorbate and upper layer of the support were relaxed to yield the reported binding energies. Where specifically noted, the Rh_{37} nanoparticle itself was allowed to further relax under the influence of the oxide, yielding relaxed binding energies. This two-fold approach allows us to decouple the geometric relaxation-induced support effects from the remaining aspects of the metal–support interaction. Note that in both cases the nanoparticle Rh-Rh distances

have been relaxed from their bulk Rh via the gas-phase optimization, and the rigid and relaxed models differ only via the additional relaxation induced by the support.

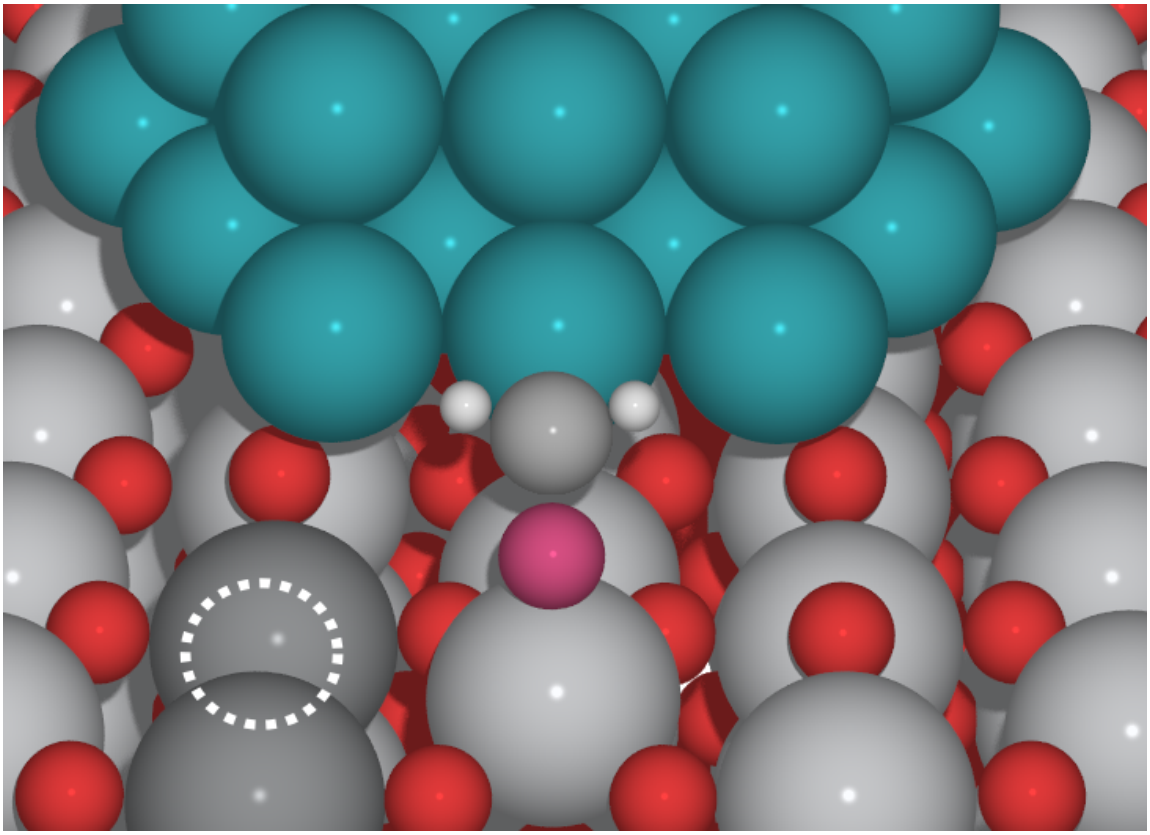

Figure 5.2: A schematic illustration showing one 'dual' binding geometry, with oxygen vacancy and undercoordinated Ti atoms highlighted.

Titania is a reducible oxide that is well-known to possess surface and subsurface oxygen vacancies.[145] We thus also studied defected variants of the TiO_2 and (H)TiO_2 supports in order to measure the effect of partial surface reduction on adsorbate binding and reactivity. The bridging oxygen atom (TiO_2) or OH group ((H)TiO_2) nearest the adsorbate (but not directly under the nanoparticle) was removed, and the upper layer of the support was allowed to relax. Although description of such oxygen vacancies can be challenging within the context of DFT, it has been shown the DFT+U formalism is able to qualitatively describe the process of oxygen vacancy formation.[146] For so-called

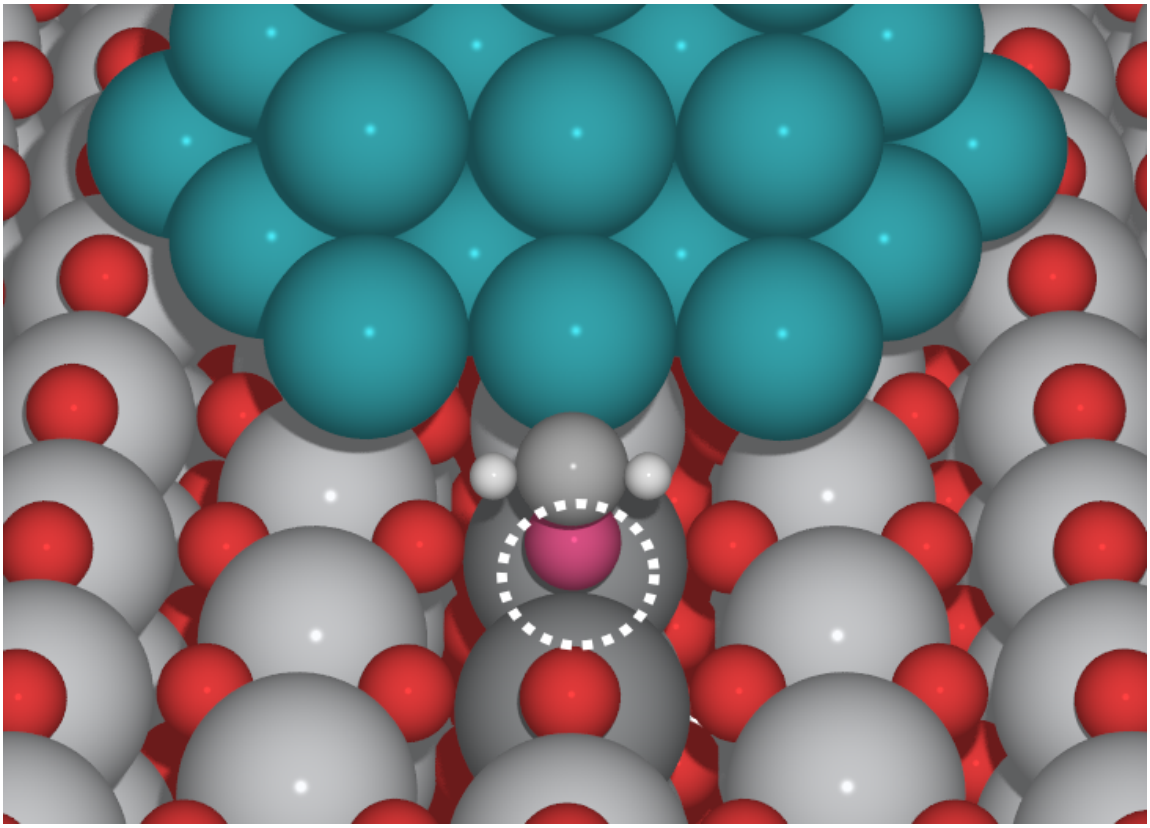

Figure 5.3: A schematic illustration showing one 'dual catalytic' binding geometry, with the adsorbate binding directly into oxygen vacancy. Oxygen vacancy and undercoordinated Ti atoms are highlighted.

'dual' binding sites, the adsorbate was allowed coordinate directly to the underlying TiO_2 support (Figure 5.2). To examine the influence of direct interaction between an adsorbate and a vacancy, we also considered an alternate geometry where the nanoparticle was positioned directly over a row of bridging oxygen atoms, thus facilitating intimate contact between adsorbate and vacancy (Figure 5.3).

Computational Methods

All DFT calculations were performed using the Atomistic Simulation Environment (ASE)[147] with the Vienna Ab Initio Software Package 5.3.3 (VASP)[148–151] and the Perdew–Burke–

Ernzerhof (PBE)[152,153] exchange–correlation functional. Core electrons were treated using the Projector Augmented Wave (PAW) approach.[154,155] The Brillouin zone was sampled at the Γ point only due to the large dimensions of the simulation cell. Geometry optimizations employed a 300 eV plane wave cutoff with 0.05 eV Gaussian smearing, and a tight SCF energy convergence criterion of 10^{-6} eV. Minimizations were performed using the fast inertial relaxation engine (FIRE)[156] algorithm as implemented in VASP[157] with a force convergence criterion of 0.05 eV $Å^{-1}$. Spin polarization was not taken into account for these initial optimizations. Subsequent accurate spin-polarized single-point calculations were used to evaluate all energy differences and utilized an increased plane wave cutoff of 400 eV, a 0.05 eV or 0.08 eV Gaussian smearing, and an SCF energy convergence criterion of 10^{-5} eV. The DFT+U formalism of Dudarev et al.[158] was used with a U_{eff} parameter of 2.5 eV for titanium, consistent with our previous work.[104,159] Testing shows that the reduced plane-wave cutoff and neglect of spin polarization in the initial optimizations has only a trivial impact (< 0.02 eV) on the resulting calculated energetics.

5.3 Electronic effect

The electronic character of metal nanoparticles are affected by the presence and nature of supporting material. This can arise either from electron transfer between metal and support, or through support-induced polarization of the nanoparticle electron density. Chemically reactive support materials are expected to have a greater impact on the electronic character of supported metal nanoparticles than inert support materials.

To measure the effect of this electronic interaction, we calculate the binding energy of various adsorbates to the metal nanoparticle both on support (E_{BE}(rig)) and in the gas phase (E_{BE}(bare)). In both cases, the metal nanoparticle is fixed to its gas-phase geometry in order to decouple the electronic interactions between the metal and support from the geometric perturbations to the nanoparticle induced by the presence of support. A summary of these results are presented in Figure 5.4. A complete list of all binding energies to the unsupported, TiO_2-supported, and (H)TiO_2-supported Rh_{37} nanoparticle, as well as defected variants of those support materials are presented in Tables 5.1 and 5.2.

We find that the presence of a pristine titania support has a strong stabilizing effect

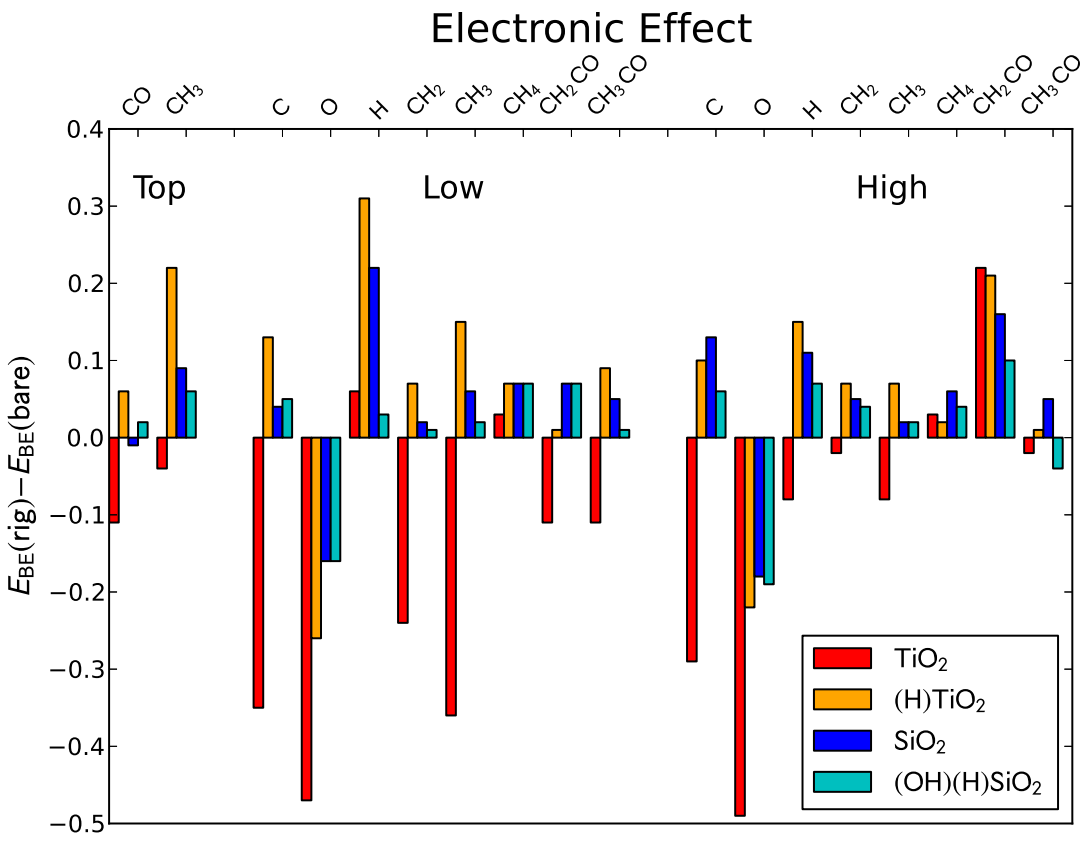

Figure 5.4: The 'electronic effect' observed in this study. Bars show the binding energy of the adsorbate onto a rigid oxide-supported nanoparticle relative to binding energy onto a nanoparticle in the gas phase, E_{BE}(rig) – E_{BE}(bare). The colors indicate which oxide the nanoparticle is supported on, with red indicating TiO_2, orange indicating (H)TiO_2, blue indicating SiO_2, and cyan indicating (OH)(H)SiO_2.

on the binding energy of adsorbates to the rigid nanoparticle. In comparison, the hydrogenated titania surface and both pristine and hydroxylated silica surfaces have a much smaller destabilizing effect. Using Bader analysis, we find that this effect is correlated to electron transfer between the nanoparticle and the support. While pristine titania support accepts around 2 to 3 electrons are transferred from the metal nanoparticle, the hydrogenated titania support *donates* around 1 electron to the metal nanoparticle.[160]

Full reduction of the titania support through hydrogenation of all undersaturated

Adsorbate	Rh_{37}	Rh_{37}/TiO_2		$Rh_{37}/(H)TiO_2$	
		Perfect	Defected	Perfect	Defected
			Top		
CO	−2.10	−2.10	−2.03	−1.92	−1.83
CHO	−2.75	−2.64	−2.66	−2.40	−2.39
CH_3O	−2.47	−2.40	−2.34	−2.13	−1.94
CH_3	−2.08	−1.99	−1.92	−1.76	−1.77
			Low		
Carbon	−7.70	−7.94	−7.98	−7.47	−7.43
Oxygen	−5.36	−5.28	−5.37	−5.26	−5.18
Hydrogen	−2.70	−2.77	−2.73	−2.33	−2.31
CH_2O	−1.30	−1.46	−1.41	−1.19	−1.13
CH	−6.84	−7.17	−7.14	−6.70	−6.61
CH_2	−4.52	−4.71	−4.65	−4.40	−4.44
CH_3	−2.15	−2.40	−2.34	−1.93	−1.77
CH_2CO	−1.74	−1.83	−1.78	−1.69	−1.63
CH_3CO	−2.47	−2.67	−2.60	−2.39	−2.23
			High		
Carbon	−7.72	−7.91	−7.88	−7.53	−7.43
Oxygen	−5.54	−5.53	−5.53	−5.42	−5.35
Hydrogen	−2.70	−2.68	−2.63	−2.48	−2.27
CH_2O	−1.22	−1.06	−1.07	−1.14	−1.12
CH	−6.80	−6.98	−6.95	−6.52	−6.45
CH_2	−4.40	−4.37	−4.32	−4.26	−4.20
CH_3	−2.18	−2.18	−2.15	−2.03	−1.95
CH_2CO	−1.45	−1.45	−1.42	−1.50	−1.42
CH_3CO	−2.81	−2.80	−2.78	−2.74	−2.67

Table 5.1: Binding energies of adsorbates to facets of the Rh_{37} nanoparticle.

surface oxygen atoms reverses the direction of charge transfer between the support and the metal nanoparticle. It is also possible to partially reduce titania through the introduction of oxygen vacancies into the surface of the support. As with many other metal oxides, oxygen vacancies are prevalent in titania, though the exact concentration and distribution of these vacancies depends on preparation procedure. To investigate the effect of oxygen vacancies in the underlying titania support on support metal nanoparticle

Adsorbate	Rh_{37}	Rh_{37}/TiO_2		$Rh_{37}/(H)TiO_2$	
		Perfect	Defected	Perfect	Defected
(1 0 0) Facet					
CO	−1.95	−1.81	−1.82	−2.15	−1.87
Carbon	−7.70	−8.00	−8.00	−7.51	−7.51
Oxygen	−5.15	−5.71	−5.69	−5.18	−5.23
Hydrogen	−2.68	−2.91	−2.85	−2.67	−2.65
CHO	−2.91	−2.48	−2.43	−2.90	−2.75
CH_2O	−1.38	−0.85	−0.81	−1.49	−1.40
CH_3O	−2.48	−2.20	−2.16	−2.28	−2.31
CH	−6.84	−7.17	−7.15	−6.69	−6.76
CH_2	−4.35	−4.32	−4.30	−4.29	−4.29
CH_3	−2.04	−1.94	−1.91	−1.82	−1.83
CH_2CO	−1.59	−1.19	−1.15	−1.64	−1.64
CH_3CO	−2.84	−2.54	−2.47	−2.70	−2.68
(1 1 1) Facet					
CO	−2.03	−1.83	−1.85	−2.01	−2.05
Carbon	−7.58	−7.74	−7.77	−7.50	−7.57
Oxygen	−5.36	−5.57	−5.56	−5.32	−5.39
Hydrogen	−2.62	−2.59	−2.58	−2.44	−2.33
CHO	−2.77	−2.35	−2.29	−2.82	−2.65
CH_2O	−1.16	−0.42	−0.37	−1.23	−1.23
CH_3O	−2.54	−2.13	−2.06	−2.03	−2.33
CH	−6.55	−6.81	−6.80	−6.48	−6.56
CH_2	−3.99	−4.18	−4.11	−3.88	−3.98
CH_3	−2.06	−1.96	−1.92	−1.75	−1.85
CH_2CO	−1.48	−1.02	−0.94	−1.43	−1.59
CH_3CO	−2.67	−2.28	−2.23	−2.41	−2.49

Table 5.2: Binding energies of adsorbates to the perimeter of the Rh_{37} nanoparticle.

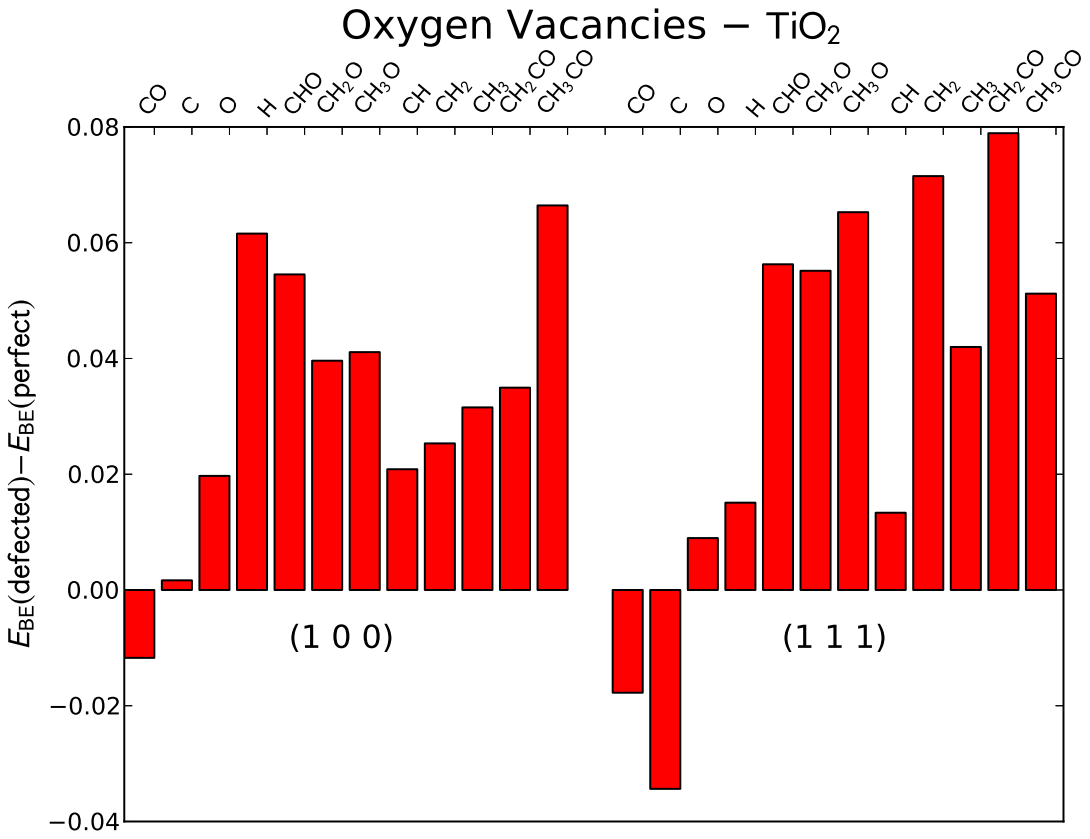

Figure 5.5: The effect on binding energies to the nanoparticle in the perimeter position (see Figure 5.1) of an oxygen vacancy in the TiO_2 support, E_{BE}(defected) – E_{BE}(perfect).

catalysis, we perform a series of calculations comparing the binding strength of Fischer Tropsch reaction intermediates to the metal nanoparticle supported on both pristine and defected titania surfaces. A summary of the results are presented in Figure 5.5.

We find that the presence of oxygen vacancies tends to *lower* the binding energy of adsorbates to the metal nanoparticle, even when the vacancy is located far from the metal itself. Furthermore, the presence of oxygen vacancies lowers the ability of the support to oxidize the nanoparticle, with around 0.2 fewer electrons being accepted by the defected titania support relative to the perfect titania support according to Bader analysis. When three oxygen vacancies are present in the titania support, we find that around 0.6 fewer electrons are accepted by the support relative to the perfect titania support.

The ability of the support to reduce the metal nanoparticle appears to depend linearly on the concentration of oxygen vacancies for supports with only a few vacancies. This is consistent with our view that the oxidation state of the underlying support directly affects catalyst activity through electron transfer between the support and the metal nanoparticle.

In a previous work, we showed that the electronic states near the metal-adsorbate bond were primarily anti-bonding in character at the Fermi level using COOP analysis.[104] This is consistent with the observation that *oxidation* of the metal nanoparticle *increases* adsorbate binding energy, while *reduction* of the nanoparticle *decreases* adsorbate binding energy. Previous work has also observed charge transfer between metal and support, highlighting the catalytic relevance of this effect on systems similar to ours.[83,161–164]

5.4 Geometric effect

Atoms in the bulk of a metal have symmetric interactions with neighboring atoms in all directions, while the lower symmetry of the metal surface typically causes the inter-layer spacing to shrink relative to its bulk values. Similarly, nanoparticles in the gas phase exhibit shorter nearest neighbor distances than what is observed for the bulk system. However, when a metal nanoparticle is placed on the surface of a support, even relatively weak metal–support interactions will result in longer metal–metal bond distances at the metal–support interface. Stronger interactions may result in substantial morphological changes, such as flattening of the nanoparticle into a 'pancake', or covering of the nanoparticle by migrating support material (the strong metal–support interaction)[21,22].

In order to measure the impact of the small geometric perturbations that arise from weak metal–support interactions on catalysis, we perform a series of DFT calculations designed to disentangle the effect of nanoparticle relaxation induced by support from other catalyst-support or adsorbate-support interactions. First, we place the rigid gas-phase-geometry nanoparticle on each support, and calculate the binding energy of each adsorbate to the nanoparticle, $E_{\mathrm{BE}}(\mathrm{rig})$. Then, we allow all nanoparticle degrees of freedom to relax, and recalculate the binding energy of each adsorbate, $E_{\mathrm{BE}}(\mathrm{rel})$. A summary of the differences between these two energies are presented in figure 5.6.

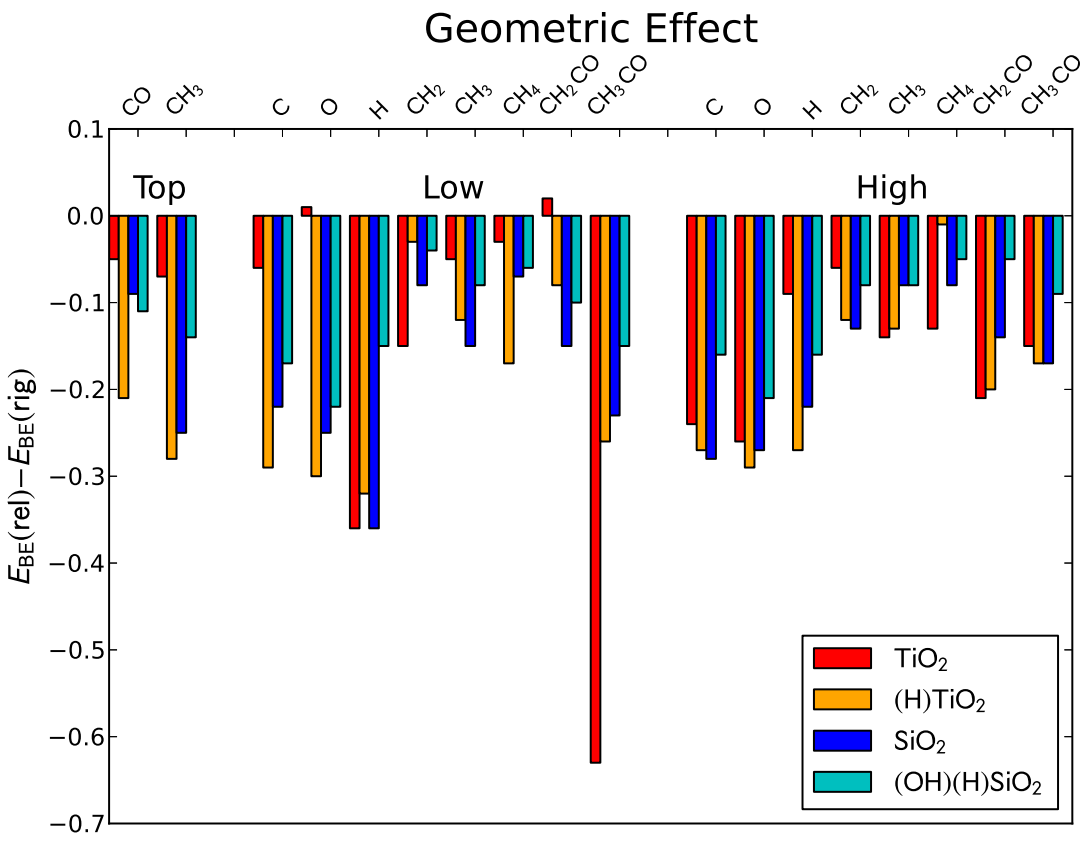

Figure 5.6: The 'geometric effect' observed in this study. Bars show the binding energy of the adsorbate onto a fully relaxed nanoparticle relative to the binding energy onto a nanoparticle in its fixed gas-phase geometry, E_{BE}(rel) – E_{BE}(rig). The colors indicate which oxide the nanoparticle is supported on, with red indicating TiO_2, orange indicating (H)TiO_2, blue indicating SiO_2, and cyan indicating (OH)(H)SiO_2.

It is clear from this figure that relaxation of the nanoparticle tends to *increase* the strength with which adsorbates bind to the metal nanoparticle, even when bound to regions of the nanoparticle that are far from the metal–support interface. Due to the systematic nature of this effect, supported nanoparticles will shift the equilibrium for bond-breaking steps towards the dissociated state relative to unsupported metal catalysts.

Moreover, this effect is largely independent of the exact nature of the support, requiring only that the support is present in some form. This effect is seen even for the chemically

inert silica, suggesting that chemical activity is not a prerequisite for metal–support interactions to be observed. Indeed, we observed in a previous work a net shift in the reaction energy of CO dissociation of around 0.5 eV favoring the dissociated state due the presence of an underlying silica support.[104]

5.5 Dual-site adsorption

The presence of a metal–support interface creates the possibility of adsorbate binding to both the metal and the support at the same time. While many support materials such as silica or amorphous carbon are considered chemically inert, other materials such as titania or alumina are known to be chemically active and can participate in catalysis through a variety of means, such as hydrogen spillover. To measure this effect, we investigate the binding geometries of carbonyl-group-containing adsorbates which interact with the support and the metal nanoparticle simultaneously, and compare the energy of these geometries to the most favorable metal-only binding geometries.

Figure 5.7 summarizes the difference in binding energy between the interfacial binding geometry and the most stable metal-only binding geometry on pristine and defected TiO_2 support; a complete list of binding energies are also presented in table 5.3. We find that binding to these interfacial sites is generally more favorable than the metal-only binding geometry. On the pristine TiO_2 surface, the carbonyl oxygen binds to one of the undercoordinated bridging Ti atoms, while the carbon atom binds to the metal nanoparticle. We investigate the same binding geometry on the defected TiO_2 surface by introducing a nearby oxygen vacancy. Binding to the defected TiO_2 surface tends to be somewhat stronger than to the pristine surface, but not by a substantial amount. However, when an adsorbate binds directly to a surface oxygen vacancy, the binding strength becomes much stronger, in some cases almost 1.2 eV stronger than the most stable metal-only binding geometry.

Figure 5.8 shows the same data as 5.7, but for the fully hydrogenated (H)TiO_2 support. As with the metal-only binding geometries, we see generally weaker binding in the dual metal–support binding geometry with (H)TiO_2 as compared to the pristine TiO_2 support. However, several adsorbates bind to vacancies in the (H)TiO_2 support much more strongly

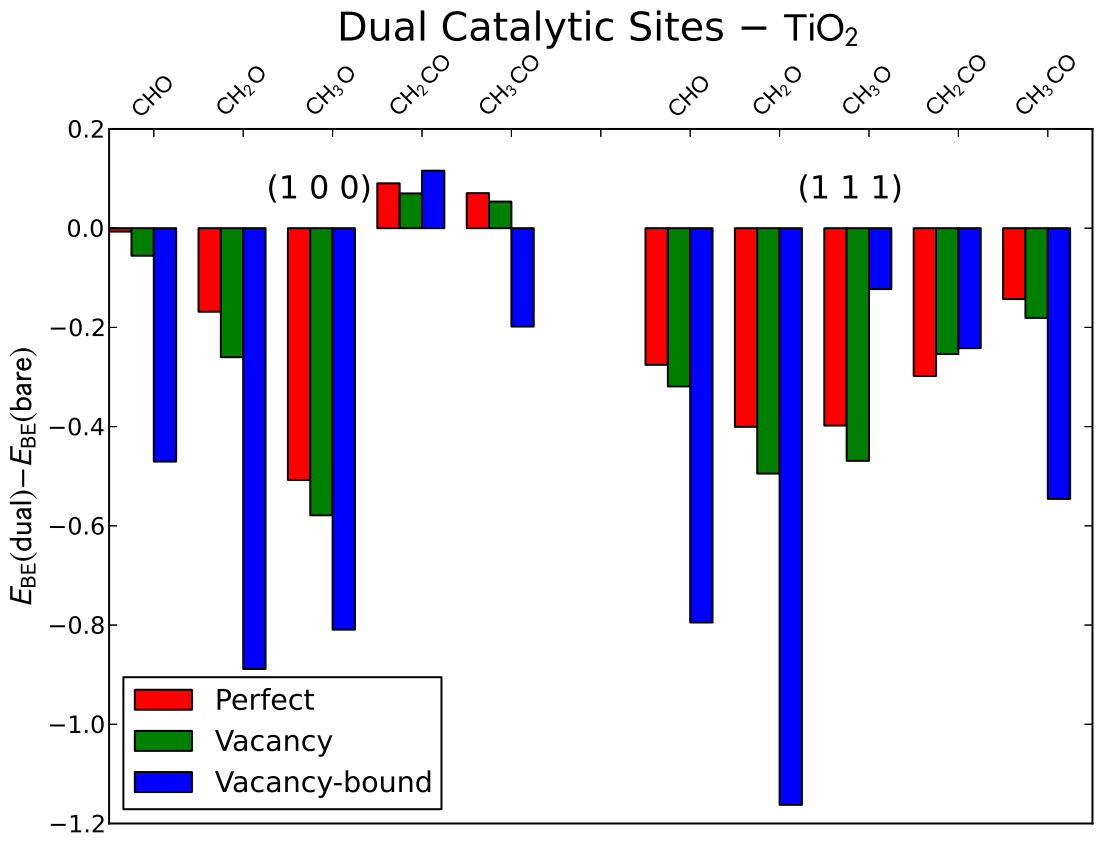

Figure 5.7: The effect on binding energies of adsorbates binding directly to the underlying TiO_2 support. Red bars indicate a perfect support with no oxygen vacancies, green bars indicate that there is an oxygen vacancy, but the adsorbate is not directly binding to the resulting undercoordinated Ti atoms, and blue bars indicate that there is an oxygen vacancy, and the adsorbate is binding directly to the resulting undercoordinated Ti atoms.

than observed for the TiO_2 support. While this could be due to differences in the electronic properties of the nanoparticle or the support, it is much more likely this is due to geometric differences between the two support materials. The metal–oxygen distance is larger on the hydrogenated support than with the pristine support, due to the presence of additional surface H atoms. This may result in adsorbates binding more strongly to vacancies in one material over the other purely due to how that particular adsorbate fits into the two binding sites.

Adsorbate	Rh_{37}	Rh_{37}/TiO_2			$Rh_{37}/(H)TiO_2$		
		Perfect	Defected	Vacancy	Perfect	Defected	Vacancy
			(1 0 0) Facet				
CO	−1.95	−1.82	−1.83	−1.16	−1.94	−2.00	−2.05
CHO	−2.91	−2.92	−2.97	−3.38	−2.76	−2.69	−3.20
CH_2O	−1.38	−1.55	−1.64	−2.27	−1.35	−1.24	−2.05
CH_3O	−2.48	−2.98	−3.06	−3.29	−3.02	−2.99	−3.52
CH_2CO	−1.59	−1.50	−1.52	−1.47	−1.42	−1.47	−1.99
CH_3CO	−2.84	−2.77	−2.79	−3.04	−2.58	−2.57	−2.35
			(1 1 1) Facet				
CO	−2.03	−2.07	−2.09	−1.37	−2.11	−1.89	−2.30
CHO	−2.77	−3.04	−3.09	−3.56	−2.85	−2.81	−2.81
CH_2O	−1.16	−1.56	−1.65	−2.32	−1.38	−1.39	−2.57
CH_3O	−2.54	−2.94	−3.01	−2.67	−2.99	−2.94	−3.71
CH_2CO	−1.48	−1.78	−1.74	−1.73	−1.54	−1.52	−2.36
CH_3CO	−2.67	−2.81	−2.85	−3.21	−2.60	−2.56	−3.26

Table 5.3: Binding energies of adsorbates to the metal-support interface. “Vacancy” refers to binding geometries in which the adsorbate binds directly to an oxygen vacancy.

As TiO_2 is known to readily form such oxygen vacancies, this binding motif is quite plausible for TiO_2-supported metal catalysts under realistic reaction conditions. Indeed, these results are consistent with Mars–van Krevelen-type reaction mechanisms, in which oxygen vacancies form on the support during the course of reaction and are subsequently quenched by water or other oxygen-containing reactants. The particular stability of a given dual-binding adsorbate will depend on the nature of the metal–oxide interface, as real metal nanoparticle catalysts can be quite large and polydisperse, but nonetheless these results suggest that such a mechanism is plausible. Further, if adsorbates bind to these sites too strongly, they will become poisoned during reaction, rendering them irrelevant to catalysis. It is therefore difficult to predict the importance of such sites in the absence of a detailed thermodynamic and kinetic analysis for a particular system and reaction of interest.

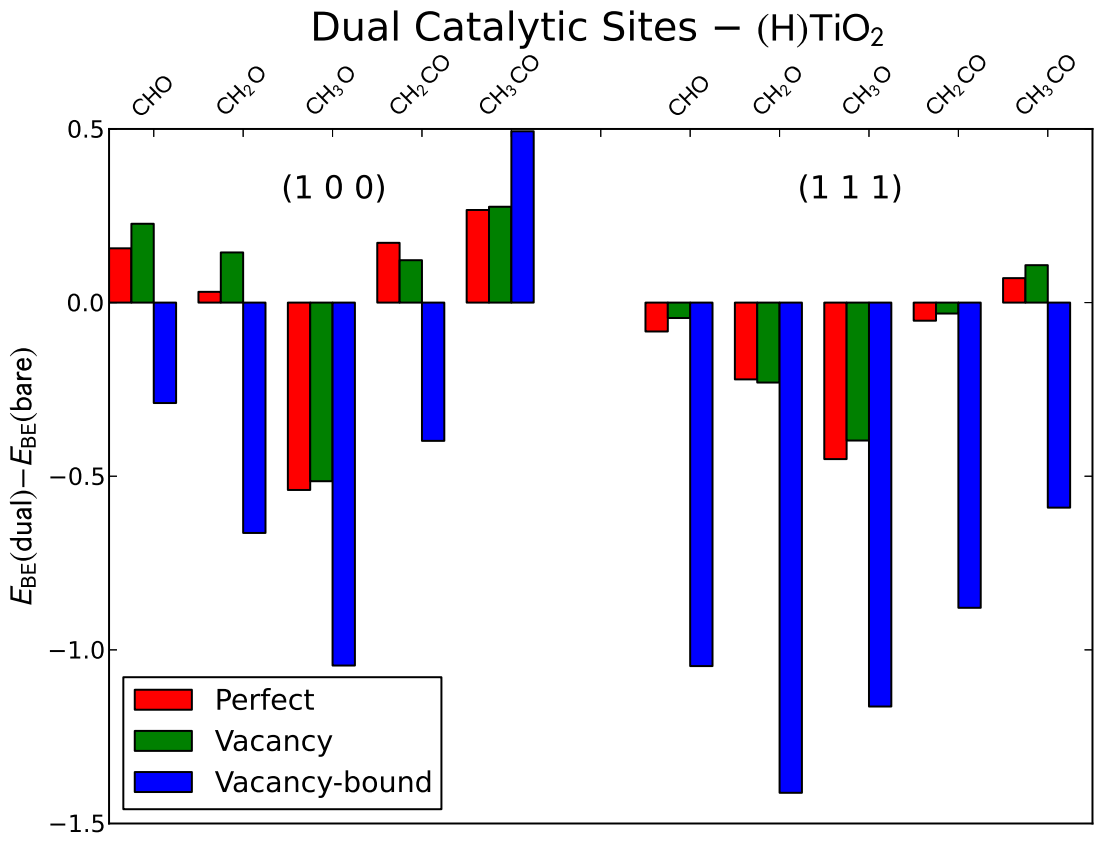

Figure 5.8: The effect on binding energies of adsorbates binding directly to the underlying (H)TiO_2 support. Red bars indicate a perfect support with no oxygen vacancies, green bars indicate that there is an oxygen vacancy, but the adsorbate is not directly binding to the resulting undercoordinated Ti atoms, and blue bars indicate that there is an oxygen vacancy, and the adsorbate is binding directly to the resulting undercoordinated Ti atoms.

5.6 Concluding remarks

The presence of support can strongly affect the thermodynamics of adsorbate binding to metal nanoparticle catalysts and the kinetics of reactions occurring on or near the catalyst. In some cases, the presence of support can change adsorbate binding energies by over 1 eV. It is therefore critical to understand how support affects particular catalytic applications in order to analyze experimental observations and make predictions based

on theoretical calculations. We showed previously that the use of silica or titania support in the Rh-catalyzed Fischer–Tropsch synthesis of alcohols could explain the observed selectivity towards ethanol over methane. A deeper understanding of the mechanism by which the support effects this change in activity would require the use of a detailed kinetic model incorporating all possible adsorbate binding geometries, including binding at the metal–support interface and to defects in the support itself.

Aside from direct participation of the support in catalysis through adsorbate binding at the metal–support interface, the impact of support can be characterized through a systematic shift in the binding energies of adsorbates to supported nanoparticle catalysts relative to the unsupported catalyst. For all support materials, adsorbates will bind more strongly relative to the unsupported catalyst due to geometric relaxation of the nanoparticle resulting in longer metal–metal bond lengths. However, depending on the electronic interactions between the support and the metal catalyst, adsorbates will bind either more or less strongly. The direction of this effect can be predicted through the use of a combination of charge partitioning (such as Bader analysis) and COOP analysis, though the predictive power of such an approach might be insufficient for accurate kinetic models.

In general, the presence of support stabilizes adsorbate binding relative to the unsupported catalyst. This shifts the equilibrium of bond-breaking steps towards the dissociated state, which may or may not be desirable for a particular application. Through judicious choice of support material, it is possible to shift reaction energetics to favor formation of a desired product. As the condition of the support surface also affects the energetics of binding to supported metal nanoparticles, it is also important to consider the state of the support under reaction conditions, taking into account such things as hydrogen spillover or surface oxygen vacancy concentration. With a sufficiently well-characterized supported metal nanoparticle system, it is possible to rationalize observed catalytic activity through a combination of the intrinsic properties of the catalyst and its interaction with the support.

6 MECHANISTIC INSIGHTS INTO SOLUTION-PHASE OXIDATIVE ESTERIFICATION OF PRIMARY ALCOHOLS ON PD(111) FROM FIRST-PRINCIPLES MICROKINETIC MODELING

Reproduced with permission from Hermes, E. D.; Janes, A. N.; Schmidt, J.R. Mechanistic Insights into Solution-Phase Oxidative Esterification of Primary Alcohols on Pd(111) from First-Principles Microkinetic Modeling. *ACS Catal.* **2018**, *8*, 272–282.[165] Copyright 2018 American Chemical Society.

6.1 Introduction

Selective oxidation of alcohols to carbonyl compounds is an important class of chemical transformations used in a wide variety of synthetic applications ranging from pharmaceuticals to industrial-scale bulk chemicals.[166] Aldehydes and esters, in particular, are highly valued for both their intrinsic properties and as reagents in other synthetic pathways.[167] These compounds are typically accessed through oxidation of their alcohol analogues, frequently via stoichiometric reaction with an oxidizing agent in transformations which are both inefficient and generate a substantial amount of byproduct.[168] Heterogeneous catalysis provides an alternative route for the selective oxidation of alcohols using molecular oxygen, which improves both efficiency and prospects for scale-up.[169]

While pure platinum group metals (PGM) such as Pt and Pd are capable of catalyzing the aqueous-phase aerobic oxidation of alcohols,[170] catalyst activity can be greatly improved via addition of promoters, such as Bi, Te, or Pb.[171–174] Promoters are especially useful in the oxidative dehydrogenation of aliphatic primary alcohols, which typically exhibit poor yields in the absence of main group promoters.[175] Although the mechanism of action of the promoters is unknown, a number of hypotheses have been put forth.[176–181] Furthermore, it has been shown that metallic (rather than oxidized) PGM sites are responsible for the bulk of catalytic activity in these systems.[182–187] Experimental measurements of Pt metal catalyst working potentials indicate that the catalyst becomes reduced upon

exposure to the alcohol substrate relative to the oxidized air-exposed resting catalyst.[181,188] Moreover, cyclic voltammetry experiments show that Bismuth promotion, which improves catalyst activity, suppresses H sorption on Pt catalysts, which indicates a negative correlation between surface H coverage and catalyst activity.[181] These observations suggest that unpromoted catalysts are likely at least partially hydrogen-covered under operating conditions, in contrast to the partially oxygen-covered resting (air-exposed) catalyst.[175,181] Further characterization of these catalysts is complicated by the difficulty of performing *in situ* measurements of liquid-phase heterogeneous catalysts.

The exact mechanism for the oxidative esterification of primary alcohols over PGM is a matter of some debate. For at least some alcohols, such as benzyl alcohol, an aldehyde intermediate can be isolated. In contrast, for other alcohols such as 1-octanol, the aldehyde intermediate either reacts too rapidly to be detected, or does not form at all.[174] The exact process by which the aldehyde forms is not known. Under basic conditions, it has been proposed that the alcohol becomes deprotonated in solution and undergoes hydride elimination on the catalyst surface to form the aldehyde.[189,190] This hypothesis has been disputed due to the observation that oxidation also occurs under acidic conditions[191], and it has been proposed instead that the alkoxide is formed on the catalyst surface.[192,193] Other authors have suggested that it is the C–H bond that is broken first due to its weaker bond strength.[194,195]

The subsequent oxidation of aldehyde to ester is also poorly understood. The aldehyde intermediate may desorb from the surface and react with alcohol in solution to form a hemiacetal species.[196–198] The putative hemiacetal intermediate must be further dehydrogenated to the final ester product, analogous to the initial dehydrogenation of the alcohol to the aldehyde. However, such an aldehyde intermediate cannot always be identified, suggesting that alternative pathways may also exist.[199] Consequently, the detailed aldehyde esterification mechanism is also highly non-trivial.

In a prior computational work, Hibbitts and Neurock suggest various pathways for the dehydrogenation and oxidation of ethanol to acetate based on the DFT-calculated energetics and barrier heights for a series of reactions on the water-solvated Pd(111) surface.[40] However, due to the complexity of their setup, they were unable to perform a full microkinetic analysis, and thus their conclusions regrading the predominant reaction

pathways relied upon assumptions about the condition of the working catalyst surface (e.g. hydrogen coverage).

In this work, we use Pd(111)-catalyzed esterification of 1-propanol to methyl propionate under basic conditions as a model of aliphatic primary alcohol esterification. We utilize first-principles microkinetic modeling informed by density functional theory (DFT) calculations of the catalyst surface and the solution-phase species. Microkinetic analysis of the reaction network allows us to identify the dominant reaction pathways that contribute to the catalytic activity from the large number of possible routes from propanol to the final ester product. It also facilitates a direct examination of the state of the catalyst under working conditions and the role of various reactants, including, in particular, the role of catalytic base.

In order to achieve these goals, we develop several novel microkinetic modeling techniques for the analysis of liquid-phase heterogeneous catalytic reaction networks. This work is one of the first comprehensive applications of first-principles microkinetic modeling to a liquid-phase heterogeneous reaction network containing charged reactants, accounting for the effects of solvation on both thermodynamics and mass transport. Additionally, we introduce a method to account for adsorption and desorption of charged reactants and their influence on subsequent adsorption / reaction. Interestingly, while we find intermediate and transition state energies for our system that are in qualitative agreement with the prior findings of Hibbitts and Neurock, the predominant reaction pathways differ, likely due to the strong influence of the catalysts surface coverage under steady-state working conditions, thus highlighting the importance a detailed microkinetic model for this reaction network.

6.2 Theoretical methods

The energies and geometries of surface-bound species were determined with the periodic density functional theory (DFT) code VASP in a basis of plane waves up to a cutoff energy of 450 eV.[151,200–202] All calculations were run using the Python environment ASE.[71] Geometry optimizations and vibrational frequency calculations were performed with the PBE-D3(ABC) dispersion-corrected density functional method, and single-point energies

were evaluated with the range-separated HSE06-D3(BJ,ABC) method at the PBE-D3(ABC) geometries.[61–64,66–70,203,204] While DFT calculations using hybrid functionals such as HSE06 are significantly more computationally expensive than typical semilocal functionals such as PBE, the inclusion of exact exchange has a substantial effect on reaction barrier heights and intermediate binding energies.[205–207] PBE-D3(ABC) yields a lattice constant of 3.90 Å for bulk Pd, which compares favorably to the experimental lattice constant of 3.89 Å.[208] The Pd(111) surface was modeled as a 4-layer 3x3 slab with a 15 Å vacuum gap, and the Brillouin zone was sampled with a 3x3x1 Monkhorst-Pack k-point mesh.[209] The bottom two layers of the slab were fixed to the PBE-D3(ABC) lattice constant, while the top two layers were allowed to relax in all geometry optimizations. The effect of solvation on the catalyst surface and adsorbed intermediates were included through the use of single-point GLSSA13 continuum solvation model calculations using VASPsol with methanol as the solvent at the PBE level of theory.[210–212] Pathways for all reactions were located using the nudged elastic band method[157,213,214], and transition states were optimized using the dimer method.[203,215,216] All transition states were verified to have exactly one imaginary vibrational frequency corresponding to the expected reaction coordinate.

Solution-phase species were optimized in Gaussian 09[217] with the PBE-D3(ABC) method using the aug-cc-pVTZ basis set[218] and the SMD continuum solvation model[219] with methanol solvent. SMD was chosen since it was parametrized to reproduce experimental total free energies of solvation, including the cavitation energy. Note that for periodic calculations involving the catalyst surface, the GLSSA13 PCM is used instead of SMD. This is because SMD is parametrized to reproduce experimental *free energies* of solvation, which includes contributions arising from the loss of translational entropy of gas-phase species. This is not relevant for immobile systems, such as adsorbates on the catalyst surface. Similarly, GLSSA13 would predict inaccurate solvation free energies of species in solution due to its neglect of translational entropy loss. Single-point calculations were performed with the HSE06-D3(BJ,ABC) method[70] and the resulting energies were extrapolated to the complete basis set limit using the aug-cc-PVnZ basis sets (n = 2 to 5). Calculations were performed with and without solvation correction to determine the free energy of solvation, which was used to correct the energy of the gas-phase species as determined in VASP (see Figure 6.1). Additionally, the energy of species that carry a formal

negative charge was determined by performing calculations of the corresponding neutral radical in VASP, and adding to that the electron affinity of that species as determined in Gaussian.

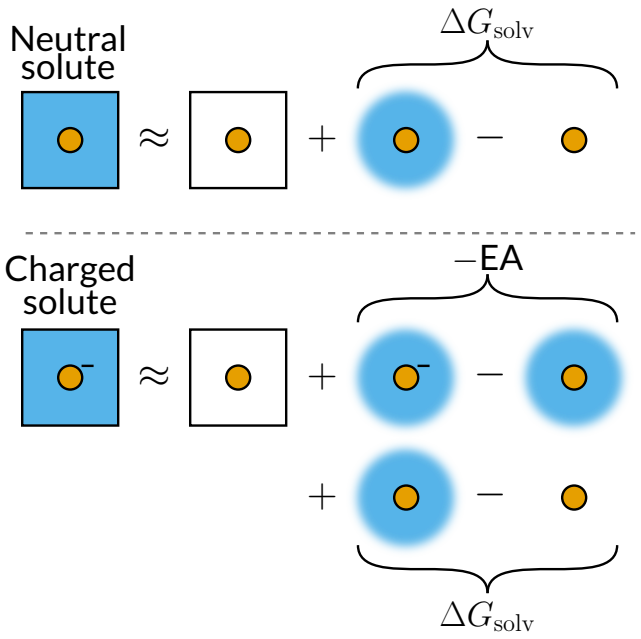

Figure 6.1: Schematic illustration of energy calculations for solution-phase species. The energy of a species in solution under periodic boundary conditions is approximated as the energy of the species in the absence of solvation under periodic boundary conditions plus the free energy of solvation, which is determined using Gaussian and SMD. For anions, we calculate the energy of the corresponding neutral radical under periodic boundary conditions without solvation, then add both the electron affinity and the solvation free energy determined using Gaussian and SMD.

The reaction network was analyzed using the Micki package[220], which allows for the construction and solution of microkinetic models from *ab initio* calculations. On-surface reaction rate constants were calculated using transition state theory. Reverse rate constants were chosen such that all reactions obey detailed balance. For barrierless on-surface reactions, transition state theory was used with a free energy barrier of 0 eV in the exothermic direction, resulting in a rate constant of $k_B T/h$. We treat $O_{2(g)}$ as a gas

phase species and enforce its equilibrium surface coverage. This is because O_2 has a low solubility in methanol and is typically introduced to the system by bubbling gas through the reactor. The rate of adsorption of all solution-phase species were calculated using a Langmuir equilibration-diffusion model (see Figure 3.1), which is described in detail in section 3.5. This model for the rate of diffusion-limited adsorption is similar to one developed by Hansen, Viswanathan, and Nørskov.[75]. For all simulations, a stationary layer thickness of 100 µm was used for diffusion. This choice of length scale motivated by a model for the laminar creeping flow of solvent around a spherical nanoparticles with a diameter of 1 nm.

The free energy for adsorbates are calculated as

$$F_{\text{ads}} = E_{\text{elec}} + F_{\text{vib}} - TS_{\text{conf}}, \tag{6.1}$$

where E_{elec} is the electronic energy, F_{vib} is the vibrational free energy, and S_{conf} is the configurational entropy. S_{conf} is 0 for all species that occupy only a single adsorption site in the microkinetic model, and $k_B \ln \frac{N_{\text{conf}}}{\sigma}$ for species occupying multiple sites, where N_{conf} is the number of equivalent configurations of the species on the surface and σ is the symmetry of the molecule with respect to its binding geometry. Most transition states are considered to take up two sites, with $N_{\text{conf}} = 6$ corresponding to the hexagonal symmetry of the Pd(111) surface. Most species have a symmetry number of $\sigma = 1$, except for symmetrical transition states such as homolytic cleavage of O_2 to two O atoms.

The free energy of O_2 was calculated under the ideal gas approximation as

$$F_{\text{gas}} = E_{\text{elec}} + F_{\text{vib}} + F_{\text{rot}} + F_{\text{trans}} + k_B T \ln\left(2 * S + 1\right), \tag{6.2}$$

where F_{rot} is the rotational free energy, F_{trans} is the translational free energy, S is the spin, and E_{elec} and F_{vib} are defined in the same way as for adsorbates. For O_2, $S = 1$, as it is a triplet in its ground state.

The free energy of solution phase species were calculated as the sum of the ideal gas free energy and ΔF_{solv}, the solvation free energy correction from the SMD continuum

solvation model,

$$F_{\mathrm{sol'n}} = F_{\mathrm{gas}} + \Delta F_{\mathrm{solv}}. \tag{6.3}$$

The free energy of an anion in solution is given by

$$F_{\mathrm{sol'n}}^{\mathrm{anion}} = F_{\mathrm{sol'n}}^{\mathrm{radical}} - \mathrm{EA}, \tag{6.4}$$

where EA is the electron affinity of the radical in solution as calculated in HSE06-D3(BJ,ABC) with the SMD continuum solvent model using Gaussian. The adsorption energy of anions is then related to the adsorption energy of the corresponding radical,

$$\Delta F_{\mathrm{ads}}^{\mathrm{anion}} = \Delta F_{\mathrm{ads}}^{\mathrm{radical}} - \Phi + \mathrm{EA} + \Delta E_{\mathrm{cap}}\theta_{\mathrm{e}}, \tag{6.5}$$

where Φ is the work function of the metal and ΔE_{cap} is the differential energy associated with adding negative charge to the catalyst surface, which we treat as a double layer capacitor.

The reference state of $O_{2(g)}$ and all solution-phase species was chosen to be 1 M, which is the standard state for solution-phase species. Note that this choice affects the reported free energy of adsorption, but does not affect any thermodynamic or kinetic parameters of the model. A diffusion constant of 2×10^{-9} m^2/s was used for all solution-phase species. We find that while adsorption is diffusion-limited, it is not rate limiting, and as such the results of our microkinetic model are invariant to the choice of diffusion constant to within an order of magnitude for all species.

We assume that the base reacts with the solvent (methanol) quantitatively to form methoxide, and we ignore the presence of any resulting conjugate acid. In this way, we control the concentration of the base by changing the concentration of methoxide in solution. We further set the concentration of the propoxide anion in solution to obey the predicted equilibrium for proton transfer from propanol to methoxide.

For adsorption of anions to the catalyst surface, we assume that the electron is transferred from the anion to the metal, resulting in a change in energy that depends on the work function of the metal. For more details, see section 3.5. The experimentally determined capacitance of a non-oxidized Palladium electrode is 23.1 $\mu F\,cm^{-2}$.[221] Given

that a single adsorption site of a Pd(111) catalyst has an area of approximately 6.57 $Å^2$, this corresponds with an absolute capacitance of approximately 1.52×10^{-20} F per site. ΔE_{cap} in equation 6.5 is the differential energy associated with adding or removing one electron from the catalyst surface per adsorption site, and is equal to approximately 10.5 eV.

Both PBE-D3(ABC) and HSE06-D3(BJ,ABC) predict the dissociative adsorption of H_2 to Pd(111) to be substantially more exothermic than experiments have shown. Consequently, the energy of surface-bound hydrogen atoms was offset by a constant value to accurately match the experimental binding enthalpy measured by Silbaugh and Campbell.[222]

The binding energy of all stable intermediates were also calculated on an H-saturated surface with a single hydrogen atom removed to make room for the adsorbate. The resulting binding energy was used to construct a linear dependence of the binding energy of all intermediates to the H coverage. Similar calculations were done to determine the lateral self-interactions of O and O_2. The lateral self-interactions of H, O, and O_2 were fitted to

$$E(\text{slab} + n\text{X}) - E(\text{slab}) = nE(\text{slab} + \text{X}) + \frac{n^2}{m}E(\text{X}\cdots\text{X}), \tag{6.6}$$

where E(slab + X) is the energy of X on the surface at infinite dilution, m is the number of binding sites in the periodic slab model (in our model, $m = 9$), and E(X···X) are the mean-field lateral interactions of species X with itself. We fit the zero-coverage energy and lateral interaction energies of H, O, and O_2 by solving this equation exactly for $n = 1$ and $n = 9$. For the lateral interaction of other species with H, we solve a similar equation,

$$E(\text{slab} + \text{X} + n\text{H}) - E(\text{slab}) - nE(\text{slab} + \text{H}) - \frac{n^2}{m}E(\text{H}\cdots\text{H}) = E(\text{slab} + \text{X}) + \frac{n}{m}E(\text{H}\cdots\text{X}). \tag{6.7}$$

This equation is solved exactly for $n = 0$ and $n = 8$.

Corrections to the free energy of transition states were calculated as

$$\Delta E_{ts} = \alpha \Delta E_{prod} + (1 - \alpha)\, \Delta E_{react}, \tag{6.8}$$

where ΔE_i is the correction to the free energy of species i including lateral interactions

effects, and α is the lateness of the transition state, which we approximate as

$$\alpha = \frac{\Delta F^{\ddagger}_{\text{for}}}{\Delta F^{\ddagger}_{\text{for}} + \Delta F^{\ddagger}_{\text{rev}}}, \tag{6.9}$$

where $\Delta F^{\ddagger}$ is the forward or reverse free energy barrier *excluding* coverage effects. If a species includes a constant correction to the free energy (such as adsorbed H, to match experimental values), equations 6.8 and 6.9 are solved self-consistently. For a more detailed discussion, see section 3.4.

The reactor was modeled as an idealized continuous stirred-tank reactor (CSTR) at 330 K. The gas- and solution-phase concentration of all reactants and products were fixed to their initial values. The coupled differential equations were solved until the rate of change of all concentrations and coverages was less than 1×10^{-6} s^{-1}. Sensitivity analysis was performed by numerically perturbing model parameters and re-running the model to find the new steady state conditions. For each reaction, Campbell's degree of rate control (χ_{RC}) was determined by increasing and decreasing the forward and reverse rate constants by 0.1 %. For each species, the thermodynamic rate control (χ_{TRC}) was determined by increasing and decreasing the free energy of the species by $0.001 k_B T$. The effective activation barrier of the model was determined by increasing and decreasing the reactor temperature by 0.01 K.[78–80]

Our sensitivity analysis differs from the definition originally given by Charles Campbell et. al. Equation 6.8 indicates that the energy of a transition state is affected by perturbations to the energy of its reactants and products according to the "lateness" of the transition state. Because of this, the energy of transition states adjoining a given species will also be modified when analyzing the sensitivity of a reaction network to the binding energy of that species. This means that the degree of thermodynamic rate control of a species will be correlated to the degree of kinetic rate control of all reactions that consume or produce that species. However, since this definition is consistent with our treatment for the energy of transition states, the observed sensitivities will represent to within first order the response of the kinetic model to perturbations in the binding energies of adsorbates, whereas Campbell's definition would not.

6.3 Results and Discussion

DFT results

Table 6.1: Reaction free energies and barrier heights for all reactions considered in this work on the pristine catalyst

Reaction	ΔF (eV)	$\Delta F^{\ddagger}_{\text{for}}$ (eV)	$\Delta F^{\ddagger}_{\text{rev}}$ (eV)
$RCH_2OH_{(sol'n)} + * \longleftrightarrow RCH_2OH*$	−0.35		
$RCH_2O^-_{(sol'n)} + * \longleftrightarrow RCH_2O* + e^-$	−1.97		
$CH_3O^-_{(sol'n)} + * \longleftrightarrow CH_3O* + e^-$	−1.52		
$O_{2(g)} + * \longleftrightarrow O_2*$	0.06		
$RCH_2OH* + * \longleftrightarrow RCH_2O* + H*$	0.71	1.38	0.66
$RCH_2OH* + O* \longleftrightarrow RCH_2O* + OH*$	0.33	0.40	0.07
$RCH_2OH* + OH* \longleftrightarrow RCH_2O* + H_2O*$	−0.02		
$RCH_2OH* + O_2* \longleftrightarrow RCH_2O* + OOH*$	0.21		
$RCH_2OH* + * \longleftrightarrow RCHOH* + H*$	0.13	0.74	0.61
$RCH_2O* + * \longleftrightarrow RCHO* + H*$	−0.61	0.36	0.97
$RCHOH* + * \longleftrightarrow RCHO* + H*$	−0.03	0.70	0.73
$RCHOH* + O* \longleftrightarrow RCHO* + OH*$	−0.41		
$RCHOH* + OH* \longleftrightarrow RCHO* + H_2O*$	−0.76		
$RCHOH* + O_2* \longleftrightarrow RCHO* + OOH*$	−0.53		
$RCHO* \longleftrightarrow RCHO_{(sol'n)} + *$	0.27		
$RCHO* + * \longleftrightarrow RCO* + H*$	−0.59	0.13	0.73
$RCO* + CH_3O* \longleftrightarrow RCOOCH_3* + *$	−1.04	0.16	1.19
$RCHO_{(sol'n)} + CH_3O^-_{(sol'n)} \longleftrightarrow RCHOOCH_3{}^-{}_{(sol'n)}$	−0.20		
$RCHOOCH_3{}^-{}_{(sol'n)} + * \longleftrightarrow RCHOOCH_3* + e^-$	−2.51		
$RCHOOCH_3{}^-{}_{(sol'n)} + CH_3OH_{(sol'n)} \longleftrightarrow RCH(OH)OCH_{3(sol'n)} + CH_3O^-_{(sol'n)}$	0.26		
$RCH(OH)OCH_{3(sol'n)} + * \longleftrightarrow RCH(OH)OCH_3*$	−0.52		
$RCH(OH)OCH_3* + * \longleftrightarrow RCHOOCH_3* + H*$	0.35	1.09	0.74
$RCH(OH)OCH_3* + O* \longleftrightarrow RCHOOCH_3* + OH*$	−0.02	0.37	0.40

Table 6.1 (continued)

$RCH(OH)OCH_3* + OH* \longleftrightarrow RCHOOCH_3* + H_2O*$	−0.37		
$RCH(OH)OCH_3* + O_2* \longleftrightarrow RCHOOCH_3* + OOH*$	−0.14		
$RCH(OH)OCH_3* + * \longleftrightarrow RC(OH)OCH_3* + H*$	0.15	0.76	0.61
$RC(OH)OCH_3* + * \longleftrightarrow RCOOCH_3* + H*$	−0.80	0.18	0.98
$RC(OH)OCH_3* + O* \longleftrightarrow RCOOCH_3* + OH*$	−1.18		
$RC(OH)OCH_3* + OH* \longleftrightarrow RCOOCH_3* + H_2O*$	−1.53		
$RC(OH)OCH_3* + O_2* \longleftrightarrow RCOOCH_3* + OOH*$	−1.30		
$RCHOOCH_3* + * \longleftrightarrow RCOOCH_3* + H*$	−1.01	0.41	1.42
$RCOOCH_3* \longleftrightarrow RCOOCH_{3(sol'n)} + *$	0.556		
$O_2* + * \longleftrightarrow 2O*$	−1.89	0.91	2.81
$O_2* + H* \longleftrightarrow OOH* + *$	−0.50	0.60	1.09
$OOH* + * \longleftrightarrow O* + OH*$	−1.77	0.07	1.84
$O* + H* \longleftrightarrow OH* + *$	−0.38	0.83	1.21
$OH* + H* \longleftrightarrow H_2O* + *$	−0.73	0.73	1.46
$2OH* \longleftrightarrow H_2O* + O*$	−0.35	0.52	0.86
$OH* + e^- \longleftrightarrow OH^-_{(sol'n)} + *$	1.55		
$H_2O* \longleftrightarrow H_2O_{(sol'n)} + *$	−0.03		
$CH_3O* + H* \longleftrightarrow CH_3OH* + *$	−0.91	0.45	1.37
$CH_3OH* + O* \longleftrightarrow CH_3O* + OH*$	0.54		
$CH_3OH* + OH* \longleftrightarrow CH_3O* + H_2O*$	0.19		
$CH_3OH* + O_2* \longleftrightarrow CH_3O* + OOH*$	0.41		
$CH_3OH* \longleftrightarrow CH_3OH_{(l)} + *$	0.13		
$2\,H* \longleftrightarrow H_{2(sol'n)} + 2\,*$	0.60		

Table 6.2: Free energies of reaction and forward and reverse free energy barriers for the all reactions considered in the microkinetic model (discussed later) under steady state conditions. Missing values for $\Delta F^{\ddagger}_{for}$ and $\Delta F^{\ddagger}_{rev}$ indicate that the reaction is barrierless.

Reaction	ΔF (eV)	$\Delta F^{\ddagger}_{for}$ (eV)	$\Delta F^{\ddagger}_{rev}$ (eV)
$RCH_2OH_{(sol'n)} + * \longleftrightarrow RCH_2OH*$	−0.01		

Table 6.2 (continued)

$RCH_2O^-_{(sol'n)} + * \longleftrightarrow RCH_2O* + e^-$	0.44		
$CH_3O^-_{(sol'n)} + * \longleftrightarrow CH_3O* + e^-$	0.34		
$O_{2(g)} + * \longleftrightarrow O_2*$	0.24		
$RCH_2OH* + * \longleftrightarrow RCH_2O* + H*$	1.10	1.64	0.54
$RCH_2OH* + O* \longleftrightarrow RCH_2O* + OH*$	0.47	0.52	0.05
$RCH_2OH* + OH* \longleftrightarrow RCH_2O* + H_2O*$	−0.06		
$RCH_2OH* + O_2* \longleftrightarrow RCH_2O* + OOH*$	1.11		
$RCH_2OH* + * \longleftrightarrow RCHOH* + H*$	0.25	0.81	0.56
$RCH_2O* + * \longleftrightarrow RCHO* + H*$	−0.92	0.27	1.20
$RCHOH* + * \longleftrightarrow RCHO* + H*$	−0.07	0.69	0.75
$RCHOH* + O* \longleftrightarrow RCHO* + OH*$	−0.70		
$RCHOH* + OH* \longleftrightarrow RCHO* + H_2O*$	−1.23		
$RCHOH* + O_2* \longleftrightarrow RCHO* + OOH*$	−0.06		
$RCHO* \longleftrightarrow RCHO_{(sol'n)} + *$	−0.03		
$RCHO* + * \longleftrightarrow RCO* + H*$	−0.04	0.22	0.26
$RCO* + CH_3O* \longleftrightarrow RCOOCH_3* + *$	−1.89	0.08	1.77
$RCHO_{(sol'n)} + CH_3O^-_{(sol'n)} \longleftrightarrow RCHOOCH_3{}^-{}_{(sol'n)}$	−0.20		
$RCHOOCH_3{}^-{}_{(sol'n)} + * \longleftrightarrow RCHOOCH_3* + e^-$	0.36		
$RCHOOCH_3{}^-{}_{(sol'n)} + CH_3OH_{(sol'n)} \longleftrightarrow RCH(OH)OCH_{3(sol'n)} + CH_3O^-_{(sol'n)}$	0.26		
$RCH(OH)OCH_{3(sol'n)} + * \longleftrightarrow RCH(OH)OCH_3*$	−0.10		
$RCH(OH)OCH_3* + * \longleftrightarrow RCHOOCH_3* + H*$	0.82	1.37	0.55
$RCH(OH)OCH_3* + O* \longleftrightarrow RCHOOCH_3* + OH*$	0.19	0.47	0.29
$RCH(OH)OCH_3* + OH* \longleftrightarrow RCHOOCH_3* + H_2O*$	−0.35		
$RCH(OH)OCH_3* + O_2* \longleftrightarrow RCHOOCH_3* + OOH*$	0.82		
$RCH(OH)OCH_3* + * \longleftrightarrow RC(OH)OCH_3* + H*$	0.40	0.89	0.50
$RC(OH)OCH_3* + * \longleftrightarrow RCOOCH_3* + H*$	−1.09	0.14	1.22
$RC(OH)OCH_3* + O* \longleftrightarrow RCOOCH_3* + OH*$	−1.72		
$RC(OH)OCH_3* + OH* \longleftrightarrow RCOOCH_3* + H_2O*$	−2.26		

Table 6.2 (continued)

$RC(OH)OCH_3* + O_2* \longleftrightarrow RCOOCH_3* + OOH*$	−1.09		
$RCHOOCH_3* + * \longleftrightarrow RCOOCH_3* + H*$	−1.51	0.30	1.81
$RCOOCH_3* \longleftrightarrow RCOOCH_{3(sol'n)} + *$	0.29		
$O_2* + * \longleftrightarrow 2O*$	−0.55	1.24	1.79
$O_2* + H* \longleftrightarrow OOH* + *$	0.00	0.77	0.77
$OOH* + * \longleftrightarrow O* + OH*$	−1.18	0.09	1.27
$O* + H* \longleftrightarrow OH* + *$	−0.63	0.73	1.36
$OH* + H* \longleftrightarrow H_2O* + *$	−1.17	0.59	1.75
$2OH* \longleftrightarrow H_2O* + O*$	−0.53	0.45	0.98
$OH* + e^- \longleftrightarrow OH^-_{(sol'n)} + *$	−0.75		
$H_2O* \longleftrightarrow H_2O_{(sol'n)} + *$	−0.22		
$CH_3O* + H* \longleftrightarrow CH_3OH* + *$	−0.86	0.47	1.33
$CH_3OH* + O* \longleftrightarrow CH_3O* + OH*$	0.23		
$CH_3OH* + OH* \longleftrightarrow CH_3O* + H_2O*$	−0.31		
$CH_3OH* + O_2* \longleftrightarrow CH_3O* + OOH*$	0.86		
$CH_3OH* \longleftrightarrow CH_3OH_{(l)} + *$	−0.11		
$2\,H* \longleftrightarrow H_{2(sol'n)} + 2\,*$	0.49		

Reaction free energies and barriers were calculated for all plausible elementary steps for the oxidative esterification of propanol to methyl propionate. The free energies of all reactions considered in this work on the pristine catalyst are presented in table 6.1, and the energies under steady state conditions are presented in table 6.2. A free energy diagram for the observed reaction mechanism (from the microkinetic model, see below) is presented in figure 6.2

The free energies of reaction and barrier heights on the pristine surface are in qualitative agreement with the results of Hibbitts and Neurock[40]. In particular, we find that oxygen assistance greatly lowers the barrier to cleavage of O–H bonds, but not C–H bonds. Similarly, we find dehydrogenation of propanol to form the hydroxypropyl intermediate is the most thermodynamically and kinetically favorable first step in the absence of surface

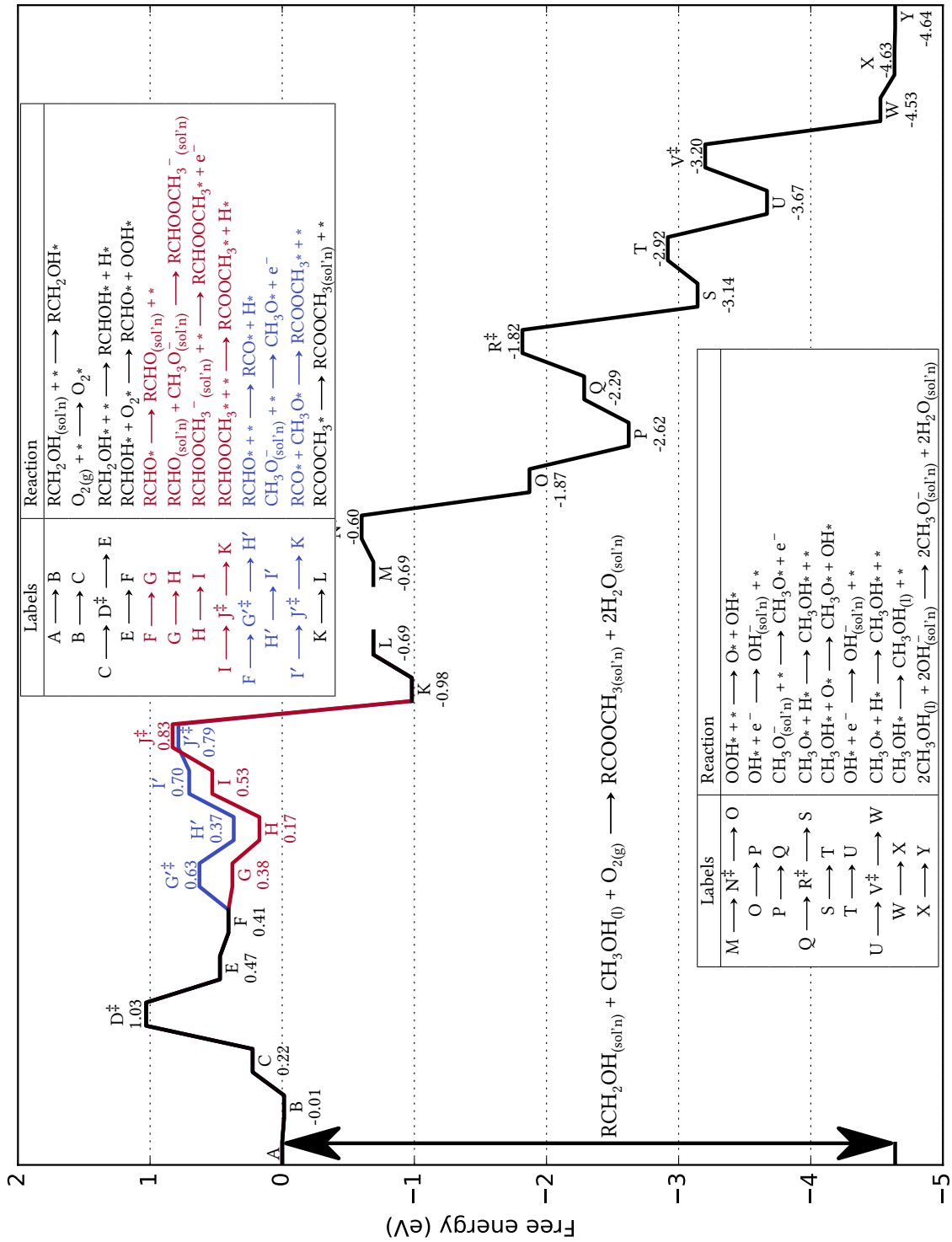

Figure 6.2: Free energy profile of one representative pathway in the overall propanol esterification reaction network under steady state conditions. The on-surface and in-solution pathways for esterification of propanal are highlighted in blue and red, respectively.

	Hibbitts		This work	
Reaction	ΔE (eV)	$\Delta E^{\ddagger}_{\text{for}}$ (eV)	ΔF (eV)	$\Delta F^{\ddagger}_{\text{for}}$ (eV)
$RCH_2OH* + * \longleftrightarrow RCH_2O* + H*$	0.60	1.36	0.71	1.38
$RCH_2OH* + O* \longleftrightarrow RCH_2O* + OH*$	0.26	0.83	0.33	0.40
$RCH_2OH* + OH* \longleftrightarrow RCH_2O* + H_2O*$	−0.22	0.30	−0.02	0.00
$RCH_2OH* + * \longleftrightarrow RCHOH* + H*$	−0.03	0.87	0.13	0.74
$RCH_2OH* + O* \longleftrightarrow RCHOH* + OH*$	−0.36	1.31	−0.25	0.90
$RCH_2O* + * \longleftrightarrow RCHO* + H*$	−0.67	0.53	−0.61	0.36
$RCH_2O* + O* \longleftrightarrow RCHO* + OH*$	−1.01	0.98	−0.99	0.74
$RCH_2O* + OH* \longleftrightarrow RCHO* + H_2O*$	−1.31	0.62	−1.34	0.61
$RCHOH* + * \longleftrightarrow RCHO* + H*$	−0.04	0.93	−0.03	0.70
$RCHOH* + O* \longleftrightarrow RCHO* + OH*$	−0.37	1.04	−0.41	0.00
$RCHOH* + OH* \longleftrightarrow RCHO* + H_2O*$	−0.79	0.00	−0.76	0.00
$RCHO* + * \longleftrightarrow RCO* + H*$	−0.31	0.30	−0.59	0.13

Table 6.3: Comparison of our results and those of Hibbitts and Neurock for some reaction free energies and barrier heights.

oxygen species. In general, we find that most kinetically relevant steps in the model are exothermic and have small or no barriers, with the exception of the dehydrogenation of propanol to hydroxypropyl and the desorption of propanal and methyl propionate. The differences between the two sets of results could be caused by a number of factors, including the different substrates under consideration (propanol in this work, as compared to ethanol in Hibbitts and Neurock), different solvents and treatment of solvation, and different DFT functionals.

While Table 6.2 indicates that adsorption of anions is strongly disfavored, this is only the case under steady state conditions due to the buildup of excess negative charge on the catalyst surface. In fact, anions bind to the pristine surface very strongly, around 1.5 eV to 2.0 eV, becoming less exothermic with increasing anion adsorption due to surface charge accumulation.

Microkinetic model results

Table 6.4: Steady state rate and Campbell's degree of rate control for all reactions considered in our model.

Reaction	Rate (h^{-1})	χ_{RC}
$RCH_2OH_{(sol'n)} + * \longleftrightarrow RCH_2OH*$	95.6	0.000
$RCH_2O^-_{(sol'n)} + * \longleftrightarrow RCH_2O* + e^-$	−7.2	0.000
$CH_3O^-_{(sol'n)} + * \longleftrightarrow CH_3O* + e^-$	105.1	0.000
$O_{2(g)} + * \longleftrightarrow O_2*$	81.9	0.000
$RCH_2OH* + * \longleftrightarrow RCH_2O* + H*$	0.0	0.000
$RCH_2OH* + O* \longleftrightarrow RCH_2O* + OH*$	0.0	0.000
$RCH_2OH* + OH* \longleftrightarrow RCH_2O* + H_2O*$	13.7	0.000
$RCH_2OH* + O_2* \longleftrightarrow RCH_2O* + OOH*$	0.00	0.000
$RCH_2OH* + * \longleftrightarrow RCHOH* + H*$	81.9	0.619
$RCH_2O* + * \longleftrightarrow RCHO* + H*$	6.5	−0.256
$RCHOH* + * \longleftrightarrow RCHO* + H*$	0.0	0.003
$RCHOH* + O* \longleftrightarrow RCHO* + OH*$	0.0	−0.002
$RCHOH* + OH* \longleftrightarrow RCHO* + H_2O*$	0.0	0.000
$RCHOH* + O_2* \longleftrightarrow RCHO* + OOH*$	81.9	0.005
$RCHO* \longleftrightarrow RCHO_{(sol'n)} + *$	46.8	−0.001
$RCHO* + * \longleftrightarrow RCO* + H*$	41.6	0.000
$RCO* + CH_3O* \longleftrightarrow RCOOCH_3* + *$	41.6	−0.001
$RCHO_{(sol'n)} + CH_3O^-_{(sol'n)} \longleftrightarrow RCHOOCH_3{}^-{}_{(sol'n)}$	46.8	0.000
$RCHOOCH_3{}^-{}_{(sol'n)} + * \longleftrightarrow RCHOOCH_3* + e^-$	46.8	0.000
$RCHOOCH_3{}^-{}_{(sol'n)} + CH_3OH_{(sol'n)} \longleftrightarrow RCH(OH)OCH_{3(sol'n)} + CH_3O^-_{(sol'n)}$	−0.1	0.000
$RCH(OH)OCH_{3(sol'n)} + * \longleftrightarrow RCH(OH)OCH_3*$	−0.1	0.000
$RCH(OH)OCH_3* + * \longleftrightarrow RCHOOCH_3* + H*$	−0.1	0.000
$RCH(OH)OCH_3* + O* \longleftrightarrow RCHOOCH_3* + OH*$	0.0	0.000
$RCH(OH)OCH_3* + OH* \longleftrightarrow RCHOOCH_3* + H_2O*$	0.0	0.000
$RCH(OH)OCH_3* + O_2* \longleftrightarrow RCHOOCH_3* + OOH*$	0.0	0.000
$RCH(OH)OCH_3* + * \longleftrightarrow RC(OH)OCH_3* + H*$	0.0	0.000
$RC(OH)OCH_3* + * \longleftrightarrow RCOOCH_3* + H*$	0.0	0.000

Table 6.4 (continued)

$RC(OH)OCH_3* + O* \longleftrightarrow RCOOCH_3* + OH*$	0.0	0.000
$RC(OH)OCH_3* + OH* \longleftrightarrow RCOOCH_3* + H_2O*$	0.0	0.000
$RC(OH)OCH_3* + O_2* \longleftrightarrow RCOOCH_3* + OOH*$	0.0	0.000
$RCHOOCH_3* + * \longleftrightarrow RCOOCH_3* + H*$	46.8	−0.001
$RCOOCH_3* \longleftrightarrow RCOOCH_{3(sol'n)} + *$	88.4	−0.024
$O_2* + * \longleftrightarrow 2O*$	0.0	0.000
$O_2* + H* \longleftrightarrow OOH* + *$	0.0	0.001
$OOH* + * \longleftrightarrow O* + OH*$	81.9	0.000
$O* + H* \longleftrightarrow OH* + *$	0.0	0.000
$OH* + H* \longleftrightarrow H_2O* + *$	0.0	0.000
$2OH* \longleftrightarrow H_2O* + O*$	0.0	0.000
$OH* + e^- \longleftrightarrow OH^-_{(sol'n)} + *$	144.7	0.000
$H_2O* \longleftrightarrow H_2O_{(sol'n)} + *$	19.2	0.000
$CH_3O* + H* \longleftrightarrow CH_3OH* + *$	150.8	0.427
$CH_3OH* + O* \longleftrightarrow CH_3O* + OH*$	81.9	0.002
$CH_3OH* + OH* \longleftrightarrow CH_3O* + H_2O*$	5.4	0.000
$CH_3OH* + O_2* \longleftrightarrow CH_3O* + OOH*$	0.0	0.000
$CH_3OH* \longleftrightarrow CH_3OH_{(l)} + *$	63.5	0.000
$2\,H* \longleftrightarrow H_{2(sol'n)} + 2\,*$	12.9	0.452

Our microkinetic model yields an overall turnover frequency of about $88.4\,h^{-1}$, consistent with the low experimentally-observed activity of the unpromoted catalyst. Based on these results, we find that two pathways to the formation of methyl propionate contribute to the majority of the activity (see Table 6.4). The first pathway involves initial dehydrogenation of adsorbed propanol (RCH_2OH) to hydroxypropyl (RCHOH), which reacts with adsorbed O_2 to form propanal (RCHO) and hydroperoxyl (OOH). OOH dissociates to O and hydroxyl (OH), and OH accepts an electron from the surface and leaves the catalyst as hydroxide (OH^-). Propanal desorbs from the surface and reacts in solution with methoxide to form a deprotonated hemiacetal anion ($RCHOOCH_3{}^-$). This anion then adsorbs to the surface

Species	Coverage	χ_{TRC}
H	0.7352	−1.368
RCH_2OH	0.1049	0.453
$RCOOCH_3$	0.0572	0.048
CH_3OH	0.0376	0.182
$RCHOHOCH_3$	< 0.0001	0.000
CH_3O	< 0.0001	0.552
RCO	< 0.0001	−0.003
O_2	< 0.0001	0.010
RCHO	< 0.0001	−0.167
$RCHOOCH_3$	< 0.0001	−0.002
RCHOH	< 0.0001	0.769
H_2O	< 0.0001	0.000
O	< 0.0001	−0.005
RCH_2O	< 0.0001	−0.525
OOH	< 0.0001	0.002
OH	< 0.0001	0.005
$RCOHOCH_3$	< 0.0001	0.000
*	0.0650	

Table 6.5: Steady state concentrations and degree of thermodynamic rate control for all adsorbates considered in our model.

and undergoes β-hydride elimination to form methyl propionate ($RCOOCH_3$). The second pathway is identical up to the formation of propanal, at which point propanal becomes further dehydrogenated by the catalyst to propanoyl (RCO), which reacts with catalyst-bound methoxy to form methyl propionate. Both pathways contribute an essentially equal amount to the overall formation of methyl propionate (see Figure 6.9).

Since our microkinetic model accounts for lateral interactions between adsorbates, reaction energies and barrier heights depend on the catalyst surface coverage. In the discussion that follows, all reported energies correspond to the steady-state catalyst coverage. In general, this tends to raise barrier heights and destabilize intermediates that form strong bonds to the catalyst relative to that of the pristine catalyst. In particular, we find that the steady state catalyst has a large buildup of adsorbed H (see Table 6.5).

In the following sections, we will discuss the results of our microkinetic model by

focusing on specific reactions that occur in the overall reaction network. We begin by discussing the dehydrogenation of propanol to propanal, followed by the esterification of propanal to form methyl propionate. We subsequently discuss the predominant pathway(s) by which H is removed from the catalyst surface, the reduction of O_2 to form H_2O, and finally the role of catalytic base. We end by outlining the possible role of main-group element additives in promoting the dehydrogenation and oxidation of alcohols.

Dehydrogenation of propanol to propanal

The first step towards formation of methyl propionate is the dehydrogenation of propanol to propanal. Formation of propanal involves sequential dehydrogenation at the alcohol oxygen and the adjacent carbon. These steps have different barriers depending on the order in which they occur, resulting in two possible pathways with different kinetics. We refer to the pathway in which the O–H bond is broken first as the "propoxy" pathway, and the pathway in which the C–H bond is broken first the "hydroxypropyl" pathway, after the partially dehydrogenated intermediates involved in the respective pathways.

In both pathways, we find that the barrier to O–H bond scission can be effectively eliminated by cooperative reduction of on-surface oxygen species in the form of O, OH, and O_2. We do not find the same cooperativity for the C–H bond scission steps. While oxygen-assisted C–H bond scission can occur, in all cases we find these reactions to have a substantially higher free energy barrier than unassisted C–H bond scission. This is likely because the C–H bonds in the surface-bound intermediates in our model form agostic interactions with underlying Pd atoms, which facilitates C–H bond scission onto the catalyst surface (see Figure 6.3). In order for a coadsorbed oxygen species to abstract H directly from the C–H bond, this agostic interaction must be broken, which destabilizes the transition state relative to the unassisted mechanism. On the other hand, O–H bond containing species can form hydrogen bonds with coadsorbed oxygen species, which facilitates direct transfer of H from one oxygen atom to another.

In the propoxy pathway (see figure 6.4), the initial unassisted O–H bond scission step has a free energy of reaction of 1.10 eV and involves a substantial free energy barrier of 1.64 eV. This reaction is made substantially more favorable via oxygen assistance, while

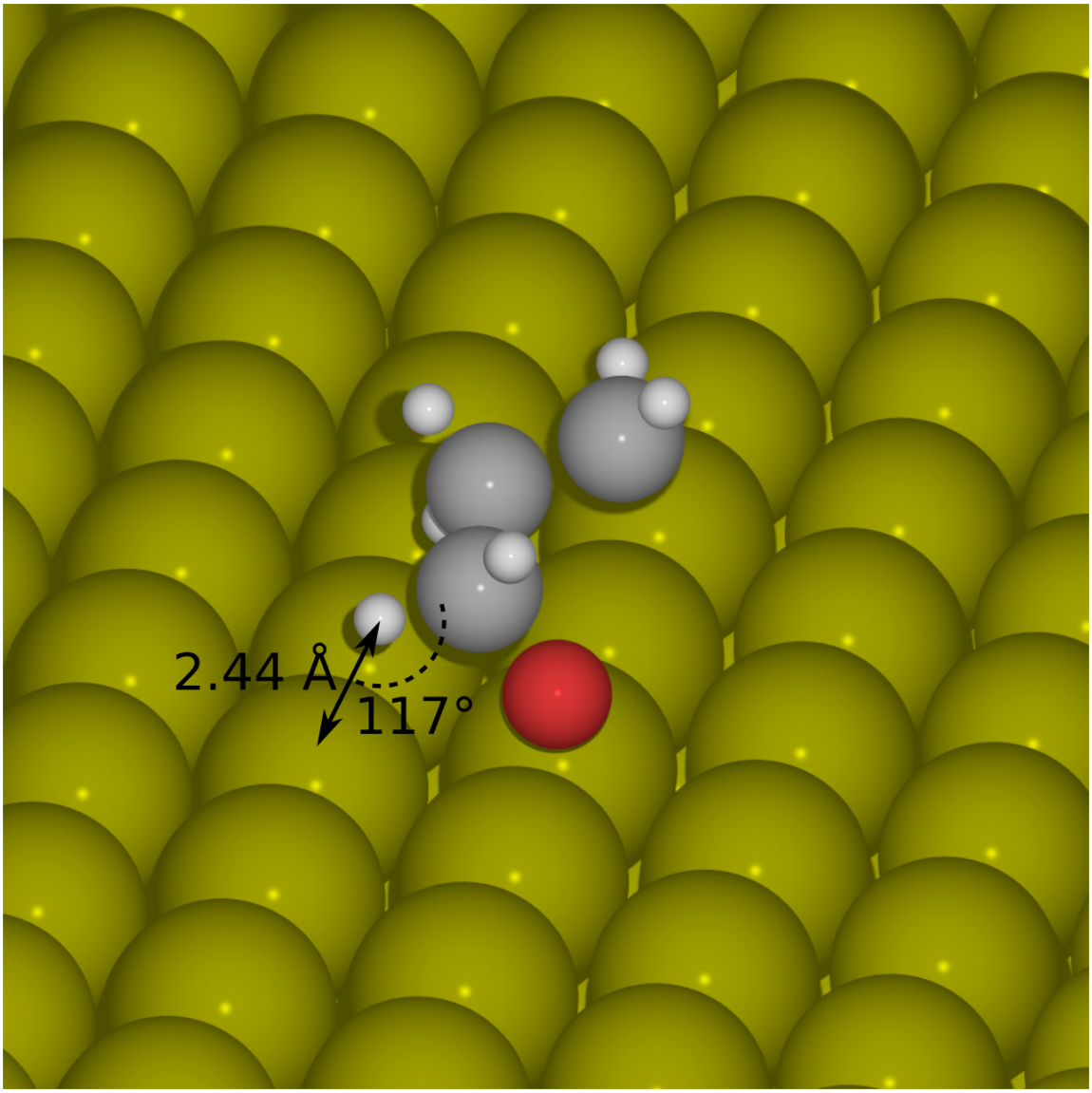

Figure 6.3: The propoxy intermediate adsorbed to the Pd(111) surface. The Pd–H distance and Pd–H–C angle are shown, which indicate an agostic type interaction.

also reducing the associated barriers. The barrier for C–H bond scission that occurs in the second step of the propoxy pathway has a free energy of reaction of −0.92 eV and a free energy barrier of 0.27 eV. For energetics on the pristine catalyst surface, see figure 6.5.

The initial step of the hydroxypropyl pathway (see figure 6.6) is C–H bond scission

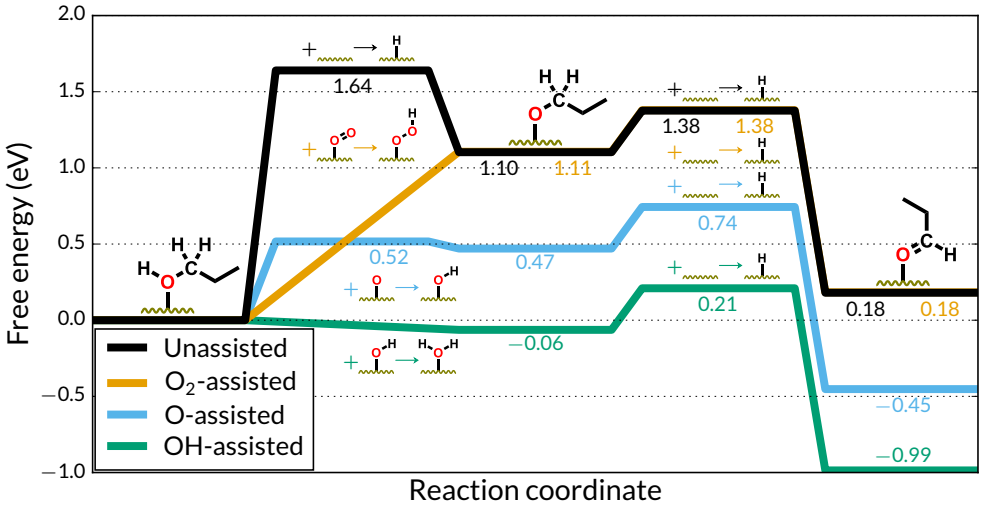

Figure 6.4: Free energy profile of the dehydrogenation of propanol to propanal through the adsorbed propoxy intermediate under steady state conditions via the unassisted (black), O_2-assisted (orange), O-assisted (blue), and OH-assisted (green) mechanisms. The zero of free energy corresponds to all co-reactants separated but pre-adsorbed on the catalyst surface.

of adsorbed propanol, which has a free energy of reaction of 0.25 eV and a barrier of 0.81 eV. The second O–H bond scission step has a free energy of reaction of −0.07 eV and an unassisted barrier of 0.69 eV. Note that both steps of the hydroxypropyl pathway have similar free energy barriers, unlike the propoxy pathway, in which the barrier to unassisted O–H bond scission is substantially higher. As in the propoxy pathway, oxygen assistance eliminates the barrier to O–H bond scission. While O–H bond scission of hydroxypropyl to propanal is exothermic in all cases, O–H bond scission of propanol to propoxy remains endothermic in most cases, with the exception of the OH-assisted mechanism, which is very slightly exothermic. For energetics on the pristine catalyst surface, see figure 6.7.

Based only on thermodynamic considerations, it is not *a priori* obvious which of these two pathways will predominate the catalyst's activity. It is clear that oxygen assistance lowers the barrier to O–H bond scission, and that the forward barriers are overall lower

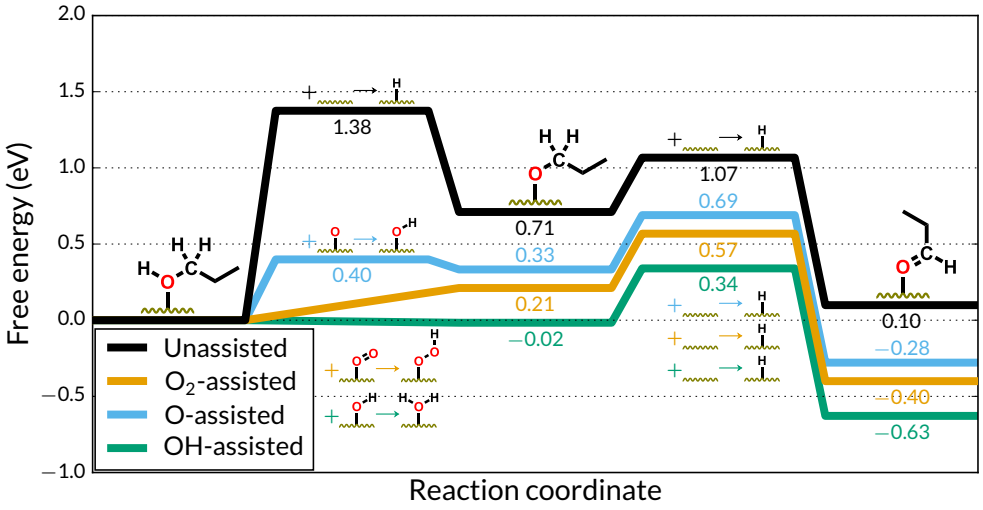

Figure 6.5: Free energy profile of the dehydrogenation of propanol to propanal through the adsorbed propoxy intermediate on the pristine surface via the unassisted (black), O_2-assisted (orange), O-assisted (blue), and OH-assisted (green) mechanisms. The zero of free energy corresponds to all co-reactants separated but pre-adsorbed on the catalyst surface.

in the oxygen-assisted propoxy pathway. However, the kinetics of the reaction are governed both by the thermodynamics of the reactants and transition state and by the concentration of the reactants on the surface. In particular, the reaction of propanol (hydroxypropyl) with surface-bound O and OH is less endothermic (more exothermic) than reaction with surface-bound O_2. However, surface-bound O and OH are formed primarily by decomposition of surface-bound OOH (free energy barrier of 0.09 eV), as the free energy barrier for O_2 decomposition is a very substantial 1.24 eV. Moreover, formation of OOH by the purely on-surface reaction of O_2* + H* has a free energy barrier of 0.77 eV, which is more unfavorable than the endothermic reaction of O_2 with propanol to form OOH and propoxide. *This suggests that O_2-assisted O–H bond scission is a prerequisite for the O-assisted and OH-assisted pathways, and therefore it must occur at some point in the reaction network.*

Microkinetic modeling gives us the ability to identify which of the many plausible reac-

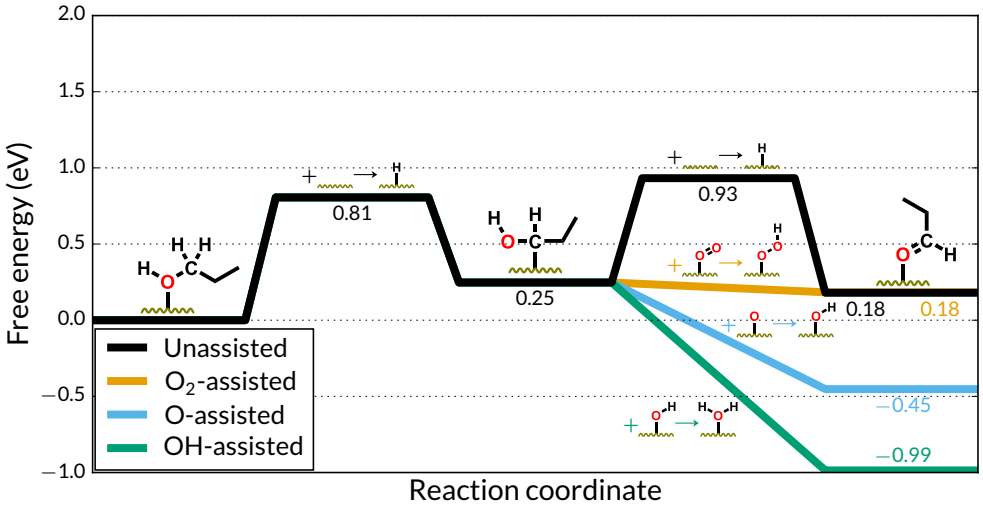

Figure 6.6: Free energy profile of the dehydrogenation of propanol to propanal through the adsorbed hydroxypropyl intermediate under steady state conditions via the unassisted (black), O_2-assisted (orange), O-assisted (blue), and OH-assisted (green) mechanisms. The zero of free energy corresponds to all co-reactants separated but pre-adsorbed on the catalyst surface.

tion pathways outlined above are, in fact, kinetically relevant. Based on our microkinetic model, we find that the initial dehydrogenation of propanol to form propanal proceeds largely through a single pathway: dehydrogenation of propanol to the hydroxypropyl intermediate, which reacts with coadsorbed O_2 to form propanal and OOH (see Figure 6.8).

Initial dehydrogenation of propanol to the hydroxypropyl intermediate (via C–H bond cleavage) has the largest barrier and the highest degree of rate control of all elementary steps in the reaction network. This reaction is endothermic by 0.13 eV on the pristine catalyst, while under steady-state conditions this nearly doubles to 0.25 eV. This increase in endothermicity of the reaction is coupled with an increase in barrier from 0.74 eV under pristine to 0.81 eV under steady state conditions. We find no barrier for the reaction of hydroxypropyl with either O or O_2. In comparison, the dehydrogenation of propoxy to propanal proceeds over a barrier of 0.27 eV (0.36 eV) under steady-state

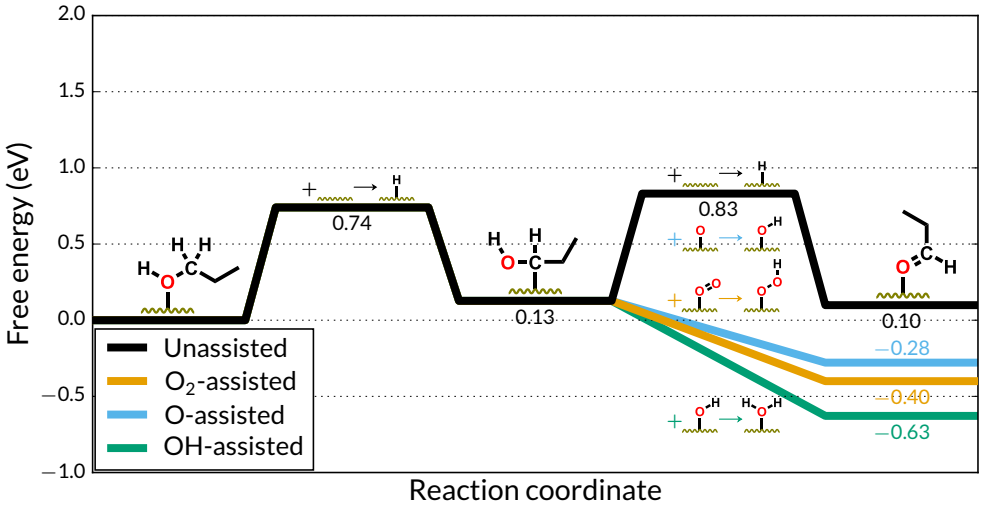

Figure 6.7: Free energy profile of the dehydrogenation of propanol to propanal through the adsorbed hydroxypropyl intermediate on the pristine surface via the unassisted (black), O_2-assisted (orange), O-assisted (blue), and OH-assisted (green) mechanisms. The zero of free energy corresponds to all co-reactants separated but pre-adsorbed on the catalyst surface.

(pristine) conditions.

One might wonder why the reaction proceeds through the hydroxypropyl intermediate at all, given the presence of propoxide in solution and the lower barrier to dehydrogenation of propoxy to propanal. However, the degree of thermodynamic rate control of adsorbed propoxy is negative, indicating that stabilization of propoxy hinders formation of methyl propionate. In fact, we observe a net *desorption* of propoxide from the surface following deprotonation of propanol by OH. These observations can be explained by the critical role of hydroxypropyl for the reduction of O_2 to OOH. As we will discuss in a later section, direct abstraction of surface-bound H by O_2 has a substantial barrier, whereas reaction of the hydroxypropyl intermediate with O_2 to form propanal and OOH is barrierless. The pathway in which propoxide anions adsorb to the catalyst and become dehydrogenated to propanal completely bypasses the hydroxypropyl intermediate, thereby inhibiting crucial O_2 reduction to OOH.

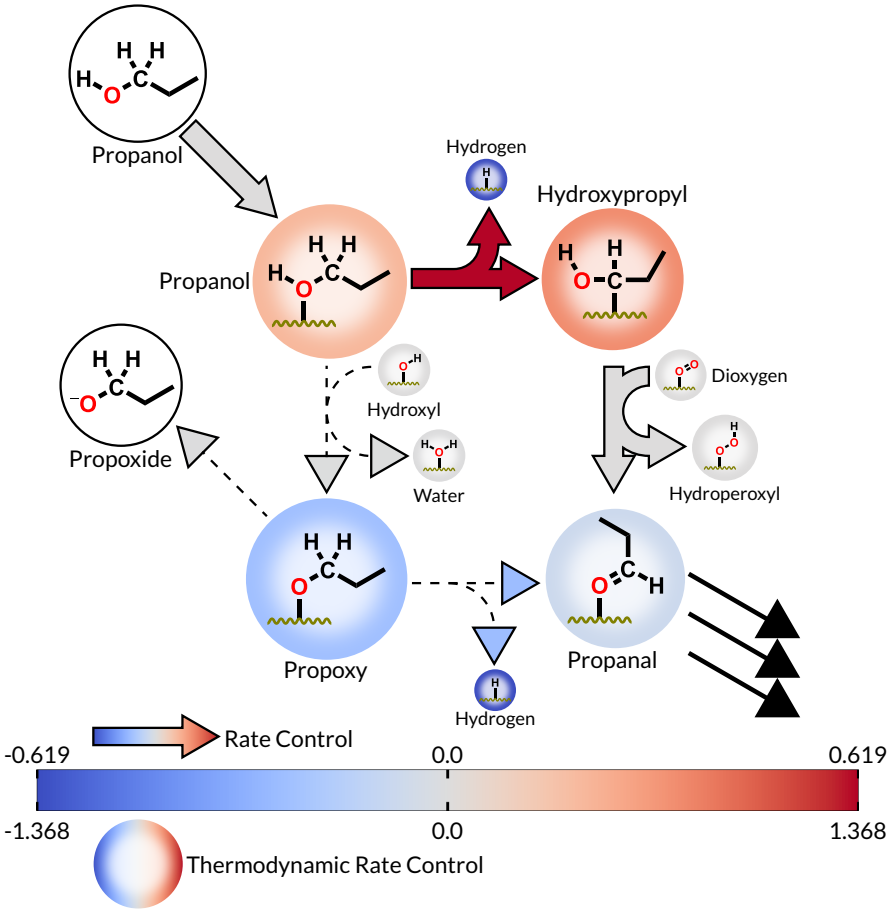

Figure 6.8: Reaction diagram for the catalytic dehydrogenation of propanol to propanal. For this and all following reaction diagrams, arrow stem thickness represents relative steady state flux and color represents the sensitivity of the rate of methyl propionate formation to the binding energy of intermediates (circles) and reaction rate constants (arrows).

Note that the predominant pathway predicted by our microkinetic model for dehydrogenation of propanol to propanal differs from the pathways proposed by Hibbitts and Neurock for dehydrogenation of ethanol to acetaldehyde, despite the similar energetics of these two systems. Hibbitts and Neurock predict that under basic conditions, the alcohol will primarily adsorb to the catalyst as the deprotonated alkoxide, which is in disagreement with the results of our microkinetic model. Our results can be explained

both by the unfavorable thermodynamics of adsorption of the alkoxide due to the negative steady-state charge acquired by the catalyst under working conditions, and by the critical role played by the hydroxypropyl intermediate in reduction of O_2. These factors are difficult to predict in the absence of kinetic modeling.

Dehydrogenation and esterification of propanal to methyl propionate

Subsequent esterification of propanal can proceed through one of two potential pathways, both involving one C–O bond formation step and one C–H bond cleavage step. The most direct pathway proceeds through dehydrogenation of surface-bound propanal to the propanoyl intermediate, which reacts with surface-bound methoxy to form the ester. The alternative pathway involves desorption of propanal, which reacts with methoxide in solution to form a deprotonated hemiacetal anion. The deprotonated hemiacetal anion then adsorbs to the catalyst and undergoes β-hydride elimination to the final ester product. In both pathways, one H atom is deposited onto the catalyst surface and one anion – either methoxide or the deprotonated hemiacetal anion – adsorbs to the surface.

Based on the results of our microkinetic model, we find that both pathways are feasible and contribute to the overall catalyst activity (see Figure 6.9). A slight majority (53 %) of the propanal that is formed on the catalyst desorbs and proceeds through the hemiacetal pathway, while the remaining propanal (47 %) becomes dehydrogenated to propanoyl. Sensitivity analysis shows that the rate of methyl propionate formation is largely unaffected by the kinetic parameters of either pathway, suggesting that esterification of propanal is not rate determining and that both pathways are capable of rapidly converting propanal to methyl propionate, which is consistent with the lack of an observed build up of aldehyde intermediates in the esterification of other primary alcohols.[174]

Note that we do not see any substantial formation of the neutral hemiacetal species either in solution or on the catalyst surface, and solution-phase deprotonated hemiacetal rapidly adsorbs to the catalyst surface and is dehydrogenated to methyl propionate. Similarly, any propanoyl that is formed on the surface reacts exothermically (–1.69 eV) and with modest barrier (0.08 eV) with adsorbed methoxy to form the ester.

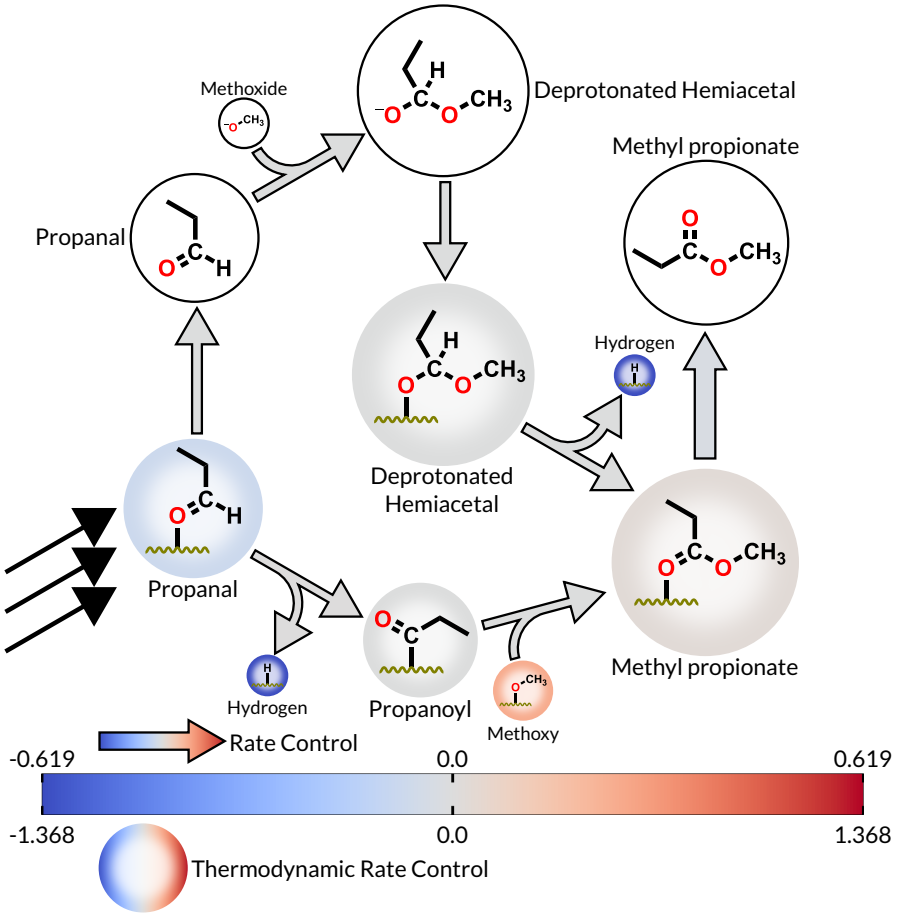

Figure 6.9: Reaction diagram for the formation of methyl propionate from propanal and methanol.

The role of hydrogen

The catalyst surface is substantially H-covered in the steady state, with 74 % of all active sites occupied by H atoms. This is consistent with experimental working catalyst potential measurements which show that even in oxygen-rich environments, PGM dehydrogenation catalysts tend to become reduced relative to the air-exposed resting catalyst when exposed to dehydrogenation targets such as alcohols.[175] These surface H atoms are byproducts of the dehydrogenation steps involved in the conversion of propanol to methyl propionate and must be removed in order to regenerate the catalyst under steady-state conditions.

While it is known that surface-bound H ultimately reduces O_2 to H_2O, the mechanism by which H is removed from the surface is complex.

Three H atoms are removed from propanol over the course of the reaction: one from an O–H bond and two from C–H bonds. We find that surface-bound oxygen species such as O, OH, and O_2 can facilitate O–H bond scission both by stabilizing the products and lowering or eliminating the reaction barrier, but these oxygen species cannot facilitate C–H bond scission. As such, while O–H bond scission does not necessarily contribute to the overall surface H coverage, the remaining two C–H dehydrogenation steps must necessarily contribute to overall surface H coverage.

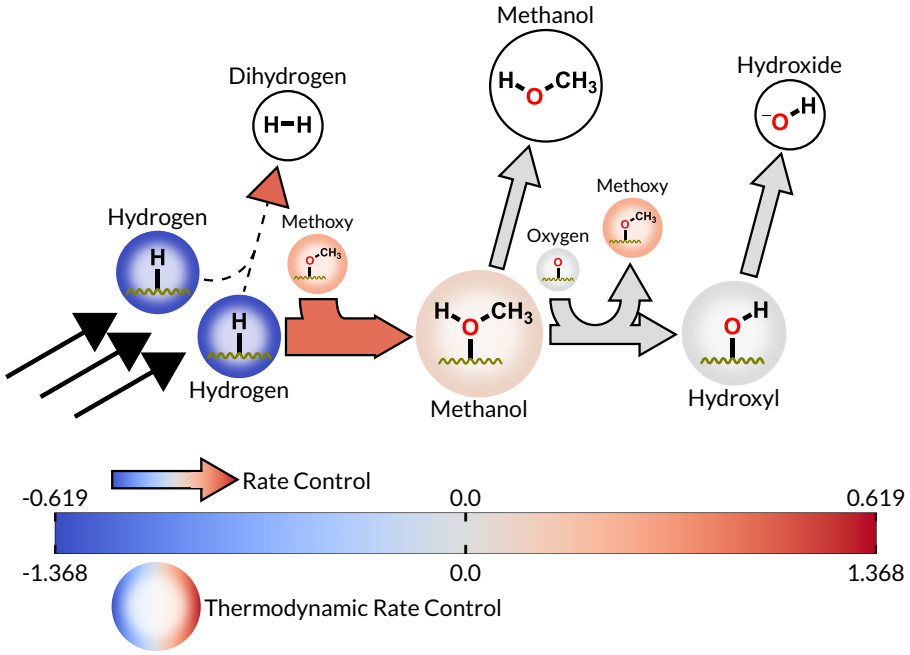

Figure 6.10: Reaction diagram of the mechanism by which adsorbed H is removed from the catalyst surface.

Once an H atom becomes adsorbed to the catalyst, there are several pathways by which it can be removed. The most direct pathway is desorption of H_2, though the rate of this pathway is expected to be small, as it does not contribute to the reduction of O_2 and it is not observed to be a major product experimentally. The majority of surface-

bound H will react to eventually form H_2O. However, direct abstraction of H from the catalyst surface by O_2, O, or OH are found to have very large barriers. Instead, we find that methoxide adsorbs to the catalyst and abstracts a proton, then it either desorbs as methanol or subsequently reacts with surface-bound O or OH to form OH or H_2O (see Figure 6.10). Any OH that is formed rapidly picks up an electron from the catalyst surface and desorbs as OH^-, which can in turn abstract a proton from the methanol solvent to form H_2O and regenerate methoxide. In this way, methoxide shuttles H atoms off the surface and onto oxygen, which is less able to directly abstract H from the surface itself,

$$CH_3O^- + 2\,H* + O* \longrightarrow CH_3OH + OH^- \longrightarrow CH_3O^- + H_2O. \tag{6.10}$$

We find that H has the most strongly negative degree of thermodynamic rate control of all species in the reaction network, with $\chi_{TRC} = -1.37$. As such, the presence of H on the catalyst surface strongly suppresses catalytic activity.

However, the negative degree of rate control observed for H does not necessarily arise from catalyst poisoning via site blocking, as around 7 % of the catalyst surface remains unoccupied in the steady state. Instead, we find that the presence of H *destabilizes* co-adsorbates through lateral interactions. Indeed, the high H coverage of the catalyst surface raises the binding energy of other adsorbates by as much as 0.83 eV in the steady state (in the case of the deprotonated hemiacetal intermediate). We find that all adsorbates are destabilized under high H coverage conditions, but closed-shell and physisorbed molecules are destabilized to much lesser extent than open-shell reaction intermediates. For example, OOH is destabilized to a much greater extent than adsorbed O_2, and consequently reduction of O_2 to OOH is less exothermic under steady state vs. pristine conditions.

The role of oxygen

The influence of O_2 on the dehydrogenation and esterification of propanol to methyl propionate is not straightforward. Clearly O_2 is required for the reaction to occur – the ultimate fate of surface-bound H atoms is H_2O – but the exact mechanism by which O_2 assists the reaction is not obvious. The most direct pathway to O_2 reduction involves

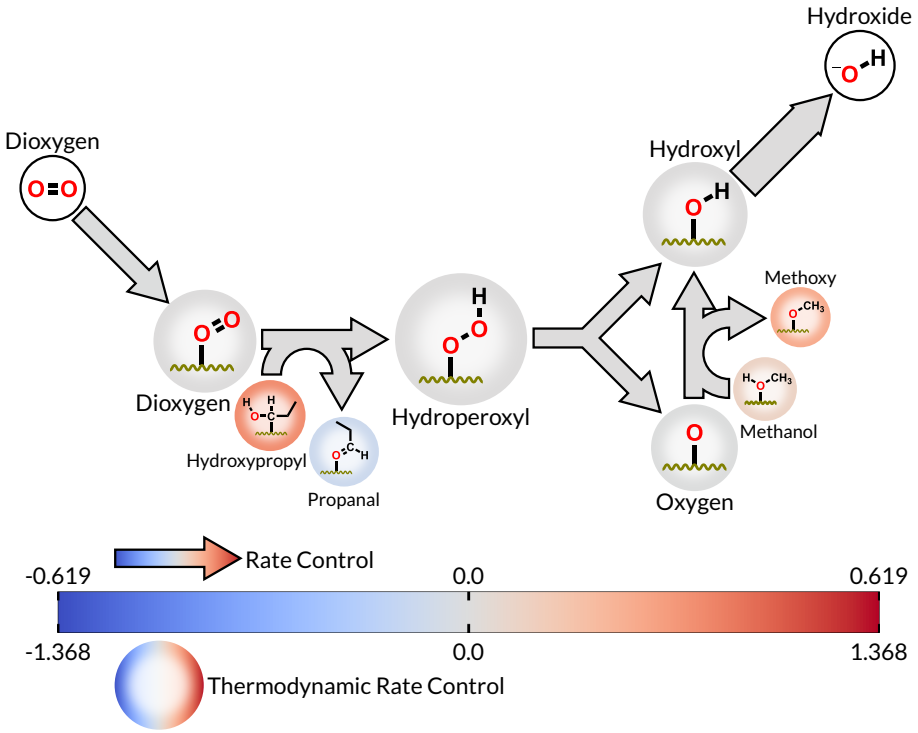

Figure 6.11: Reaction diagram for the reduction of O_2 to OH^- on the catalyst.

direct abstraction of surface H atoms; however, we find that this reaction occurs only very slowly due its large free energy barrier of 0.77 eV. Other mechanisms by which O_2 can be reduced to OOH involve direct H abstraction from O–H groups on coadsorbates such as propanol and methanol. We find that these reactions are barrierless in all cases, but slightly less thermodynamically favorable than unassisted O–H bond cleavage onto the catalyst surface. In our microkinetic model, we find that only the hydroxypropyl intermediate directly reacts with O_2 to form OOH (see Figure 6.11). This is likely because of all O–H bond scission steps in the microkinetic model, dehydrogenation of hydroxypropyl to propanal is the only one that is intrinsically exothermic, allowing it to drive the formation of OOH. The exothermicity of this reaction is due to the formation of the stable, closed-shell propanal intermediate, whereas dehydrogenation of propanol or methanol produces less stable open-shell alkoxy intermediates.

Once OOH is formed on the surface, it rapidly decomposes to O and OH. We find

that most OH that forms on the surface rapidly accepts an electron from the catalyst and desorbs as OH^-. A small amount of OH reacts with propanol to form propoxy and H_2O, which then desorbs. The remaining O atom must abstract at least one more H atom before desorbing from the surface as OH^- or H_2O. However, as with O_2, direct abstraction of surface H by O has a large free energy barrier (0.73 eV). However, O is also capable of abstracting H atoms directly from the O–H groups of coadsorbates, but unlike O_2, this reaction is intrinsically exothermic. We find that O primarily reacts with adsorbed methanol to form OH and methoxy.

The role of base

The impact of base in esterification of propanol to methyl propionate is also complex. Ultimately, we find that base facilitates removal of H atoms from the catalyst surface, but that its ability to do so is limited by removal of excess negative charge from the catalyst via OH^- desorption.

Based on the results of our microkinetic model (see Figure 6.12), we find that for each methyl propionate produced, approximately 1.64 OH^- anions and 0.08 propoxide anions desorb from the catalyst surface. To maintain charge balance, 1.19 methoxide anions and 0.53 deprotonated hemiacetal anions adsorb to the catalyst surface. Both methoxide and the deprotonated hemiacetal anions are directly involved in the formation of methyl propionate, but we find that adsorption of methoxide is in excess of what is required to react with propanoyl on the surface to form methyl propionate. This excess methoxide eventually desorbs from the catalyst surface as methanol, thereby facilitating the removal of H atoms. In fact, the effect of base can be broadly characterized as lowering the steady state H atom concentration on the surface, either by direct H atom removal (see equation 6.10) or by eliminating the need for on-surface O–H bond scission. In the absence of base, it becomes much more difficult to remove excess H from the catalyst surface, which slows the overall reaction due to destabilization of reaction intermediates, as discussed previously. Additionally, as OH cannot desorb as OH^- in the absence of base, it must further react on the surface to form H_2O before desorbing.

While base is clearly very effective at scouring H atoms from the catalyst surface,

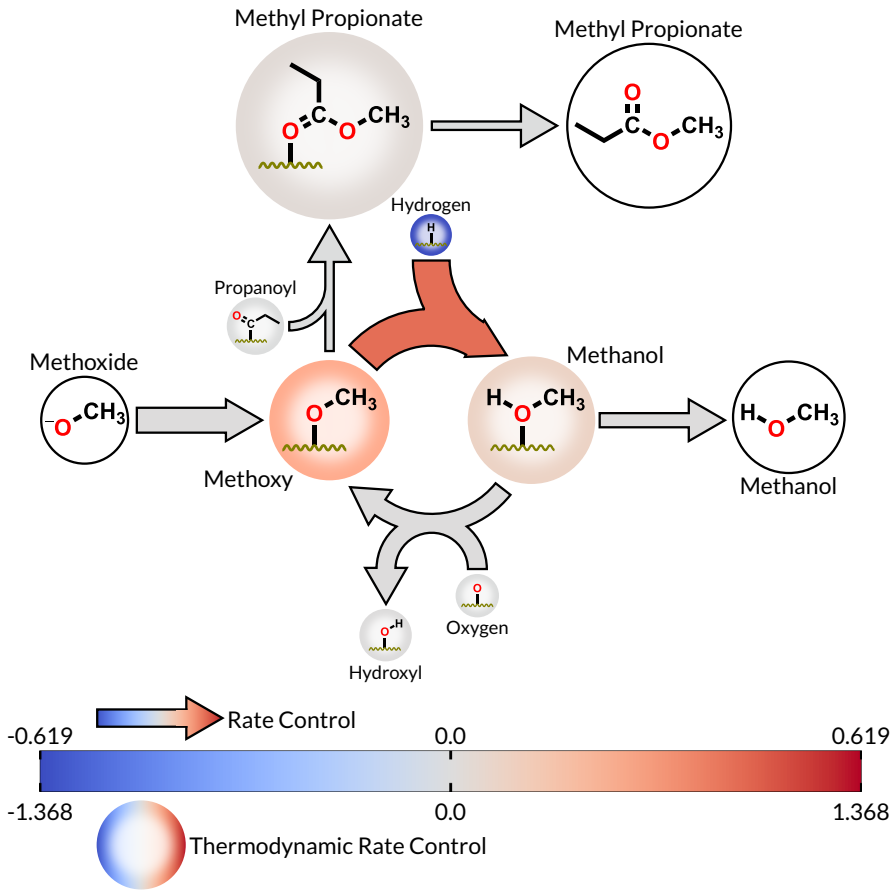

Figure 6.12: Reaction diagram illustrating the mechanism by which methoxide removes H atoms from the catalyst surface.

the rate at which this occurs is limited by removal of excess negative charge from the catalyst. On a pristine and uncharged catalyst surface, adsorption of anions from solution is strongly exothermic, due to the large work function of Pd. When an anion adsorbs to the catalyst surface from solution, its excess electron is deposited into the catalyst, making adsorption of subsequent anions less favorable due to the electrostatic repulsion between excess surface electrons. Under steady state conditions, the charge of the catalyst does not change, and thus any anions that adsorb to the catalyst will be exactly balanced by desorption of other anions. The primary way that negative charge is removed from

the catalyst is by desorption of OH^-, which is formed following reduction of O_2 to OOH. Therefore, we argue that the ability of catalytic base to remove excess H from the catalyst surface is limited by the rate at which O_2 is reduced to OOH.

We observe that the majority of OH formed on the catalyst surface immediately accepts an electron from the catalyst and desorbs as OH^-. In the absence of base, OH would need to be further reduced to H_2O before desorbing. While this reaction is strongly exothermic, it has a fairly high free energy barrier of 0.59 eV in the steady state under basic conditions. Consequently, this reaction would compete with O and O_2 for the limited number of O–H group containing coadsorbates.

In summary, catalytic base plays three key roles in the esterification of propanol on Pd(111): 1) scavenging of H from the catalyst surface, 2) deprotonation of alcohols in solution to the corresponding alkoxide (thereby removing the need for on-surface alcohol deprotonation), and 3) driving surface-bound OH to desorb as OH^- rather than requiring it be fully hydrogenated to H_2O on the catalyst.

6.4 Concluding remarks

Our first-principles microkinetic model of the solution-phase base-catalyzed oxidative esterification of propanol to methyl propionate predicts a TOF of $88.4\,h^{-1}$, consistent with the modest experimentally observed activity of the unpromoted catalyst. Sensitivity analysis demonstrates that activity is limited by the slow removal of H from the catalyst surface. Nonetheless, approximately 7 % of the catalyst surface is unoccupied in the steady state, suggesting the surface is not necessarily poisoned via site blocking. Rather, we find that the presence of adsorbed H destabilizes other reaction intermediates via strong lateral interactions. Additionally, the activity of the catalyst is hindered by a high kinetic barrier for initial C–H bond scission in propanol and the unfavorable thermodynamics of reduction of O_2 to OOH.

There have been a number of hypotheses for the mechanism by which main group promoter elements improve catalyst activity and selectivity for oxidative dehydrogenation and esterification of alcohols. These hypotheses fall into one of three broad classes: 1) the promoter blocks sites, thereby preventing the formation of strongly-bound undesired

side-products (the so-called ensemble effect);[180,181] 2) the promoter indirectly modulates the activity of the catalyst, which can, for example, prevent corrosion[179] or suppress a buildup of H[178]; or 3) the promoter directly interacts with surface adsorbates, either acting as a co-catalyst[176], or by simply coordinating adsorbates to create more stable configurations.[177]

The results of our microkinetic model and some preliminary calculations on model main-group promoted surfaces suggest that both the indirect modulation of intrinsic Pd metal binding energetics and direct participation of main group promoter elements may play a role in the oxidative dehydrogenation and esterification of alcohols on Pd. In our microkinetic model, the surface is heavily H-covered, and this results in the destabilization of many reaction intermediates due to repulsive lateral interactions. Preliminary calculations of a Te-promoted Pd(111) surface indicate that most species, including H, bind more weakly to this surface than to the unpromoted surface. We also find that stable molecules and H do not bind to Te atoms at all, whereas other reaction intermediates do (albeit more weakly than to Pd). While in our model the surface is not poisoned by H, it is approximately 74 % covered by H, and this yields a strong destabilizing effect on other adsorbates. Consequently, we believe that the Te-promoted catalyst surface will have a substantially lower steady state H coverage than the unpromoted catalyst. Microkinetic analysis of the esterification of propanol to methyl propionate on the Te- and Bi-promoted Pd(111) surfaces will be the subject of a future communication.

7 MODELING ELECTROCATALYTIC OXYGEN REDUCTION FOR H_2O_2 SYNTHESIS

7.1 Motivation

The ORR has received a large amount of attention due to its importance in fuel cell applications.[223–227] The primary goal of these studies is typically the discovery of new, chemically stable ORR electrodes with low overpotential in order to maximize the energy that can be extracted from a fuel cell. The current best electrode material for this reaction is Pt, the use of which is limited by its substantial cost. For fuel cell applications, one is most interested in the complete reduction of O_2 to H_2O, while H_2O_2 is an undesired byproduct. However, electrochemical synthesis of H_2O_2 is also very useful, with applications in water treatment and chemical synthesis.[228–230]

Currently, most commercial hydrogen peroxide is produced through homogeneous catalytic reduction of oxygen by anthraquinone derivatives.[231] This reaction proceeds through cycles in which the anthraquinone derivative is reduced by hydrogen gas and a palladium catalyst, then isolated and exposed to oxygen, producing H_2O_2. The resulting H_2O_2 must be separated from the anthraquinone derivative catalyst and purified through distillation. This process is very inefficient, as it must cycle through isolation and purification steps in order to continuously produce H_2O_2. Additionally, the process has a substantial materials cost, owing to the use of the precious metal palladium as a catalyst in the reduction step of the cycle. Electrocatalysis using non-precious metal electrodes is therefore a promising alternative route for H_2O_2 synthesis. Moreover, electrochemical synthesis of H_2O_2 is well suited for low-scale on-site production, for example in portable water purification systems. This further lowers the cost of producing H_2O_2 by eliminating the need for costly transport of the highly reactive species.

Theoretical modeling plays an increasingly important role for studies of electrocatalysis.[30,232–238] The use of theory for these systems is somewhat complicated by the need to consider the impact of the fixed external potential.[239] A tool that is commonly used to incorporate these effects is that of the computational hydrogen electrode, in which the

energy of reduction steps is related to the half-cell reaction

$$\frac{1}{2}H_2 \longrightarrow H^+ + e^-. \tag{7.1}$$

More complex models of electrocatalytic systems incorporate the effect of the applied potential on the binding energy of reaction intermediates and transition states.[238,240–244] In this work, we use the computational hydrogen electrode to investigate the oxygen reduction reaction (ORR) of O_2 to H_2O_2 on three pyrite-structure catalysts: FeS_2, CoS_2, and NiS_2.

While most computational investigation of the ORR has had the goal of maximizing selectivity to H_2O and eliminating the overpotential for this reaction, improving the selectivity to H_2O_2 requires very different properties. Prior work by Siahrostami et. al. illustrates that this selectivity arises from the intrinsic correlations between the strength with which metal surfaces bind adsorbates.[245] In order to facilitate the ORR, an electrode must bind OOH sufficiently strongly, as this is the first intermediate in the overall reaction. However, strong OOH binding correlates with strong O and OH binding, suggesting that metals which bind OOH strongly will also tend to favor its dissociation, thereby inhibiting formation of H_2O_2.

In their work, Siahrostami et. al. present a novel Pt_4Hg intermetallic catalyst that exhibits near-optimal OOH binding according to DFT calculations, as well as experimentally-determined high selectivity towards formation of H_2O_2. This catalyst exhibits impressive activity, selectivity, and stability under reaction conditions. Unfortunately, the use of Pt hinders broad use due to materials costs, and the use of Hg prevents its use in water treatment applications for safety reasons.

In addition to having favorable thermodynamic properties, this Pt_4Hg has active sites that are spatially separated. The authors reason that this hinders O–O bond dissociation through elimination of active site ensembles that stabilize the transition state for this reaction. An alternative approach to the use of intermetallic systems composed of known good ORR catalyst material is the use of metal compounds such as oxides or sulfides. In addition to the lower cost of these materials, they afford substantial versatility and novel activity beyond that which can be achieved with simple metal electrodes. One

such material is CoS_2, a conductive solid which has shown promise for a variety of electrochemical applications.[246–248] Prior experimental work has shown that not only is CoS_2 an effective ORR electrocatalyst, it also exhibits selectivity towards H_2O_2 under certain conditions.[249] Additionally, CoS_2 poses a much lower safety risk than the mercury-containing Pt_4Hg catalyst developed by Siahrostami et. al.

In order to explain the observed ORR activity and selectivity of CoS_2, we perform DFT calculations on all ORR intermediates on a CoS_2 surface. For comparison, we perform similar calculations on FeS_2 and NiS_2 surfaces, which do not exhibit the same ORR activity. While FeS_2 are NiS_2 are semiconductors (unlike CoS_2, which is at least partially metallic) and therefore not ideal for electrocatalytic applications, this serves as a useful comparison to illustrate the favorable properties of CoS_2. Finally, in order to explain the observed selectivity towards H_2O_2, we investigate the kinetics of non-electrochemical O–O bond cleavage on CoS_2, as this step necessarily leads to formation of H_2O. We see that the overall selectivity of CoS_2 to H_2O_2 in the ORR is due both to favorable thermodynamics of the electrochemical steps and the slow kinetics of non-electrochemical O–O bond cleavage.

7.2 Methods

Theoretical energies and geometries were determined using the Vienna Ab-initio Simulation Package (VASP) in a basis of plane waves up to a cutoff of 400 eV. The (100) surfaces of FeS_2, CoS_2, and NiS_2 were modeled as a 1x1 slab with two repeats of the DFT-optimized bulk lattice in the direction perpendicular to the surface. While the DFT+U formalism is commonly used in transition metal compounds such as these, we find that its use has little affect on the binding energies of intermediates for this reaction. Consequently, we do not use the DFT+U for any of the results reported in this work. All calculations were performed with the PBE exchange-correlation functional. The reaction coordinates of non-electrochemical steps were determined using the Nudged Elastic Band (NEB) method, and the transition states were optimized with the dimer method. Vibrational frequencies for all species were calculated in order to determine reaction and activation free energies. Transition states were verified to have exactly one imaginary mode corresponding to the

Reaction	ΔF(U = 0.66) (eV) FeS_2	CoS_2	NiS_2
$O_2 + e^- + H^+ + * \longrightarrow OOH*$	−0.44	−0.09	0.29
$OOH* + e^- + H^+ \longrightarrow H_2O_2 + *$	0.44	0.09	−0.29

Table 7.1: A summary of the free energy of reaction for the electrochemical steps in the ORR formation of H_2O_2 at the reaction potential of 0.66 V on the computational hydrogen electrode.

expected reaction coordinate.

With the exception of O_2, the free energy of gas-phase species were calculated using a combination of experimentally determined absolute entropies and theoretically calculated enthalpies. The free energy of O_2 was calculated using the experimental reaction free energy of the reaction $O_2 + 2H_2 \longrightarrow 2\,H_2O$ in combination with our predicted free energies for H_2 and H_2O. This was done to avoid the well-known errors in the energy of O_2 as predicted by DFT. This approximation results in a predicted reduction potential for the reaction $O_2 + 2\,H^+ + 2\,e^- \longrightarrow H_2O_2$ of approximately 0.66 V, which is in close agreement with the experimental value of 0.70 V. The free energy of adsorbates were approximated by treating all adsorbate degrees of freedom as vibrational in nature. As the nature of the binding between adsorbates and the CoS_2 surface is somewhat covalent in nature, we include the vibrational motion of the first two slab layers in the reported free energy differences. The energy of reactions involving electrochemical steps were calculated for a given potential relative to the computational hydrogen electrode.

7.3 Results and Discussion

According to the work of Nørskov et. al., the overpotential of an electrode for a particular reaction is related to the most endothermic electrochemical step in the mechanism under an applied potential equal to the overall reaction potential. The predicted standard potential for reducing O_2 to H_2O_2 is 0.66 V versus the computational hydrogen electrode; consequently, any endothermic electrochemical step in the H_2O_2 formation mechanism at 0.66 V will limit the electrocatalytic activity of the material. Activity will be maximized

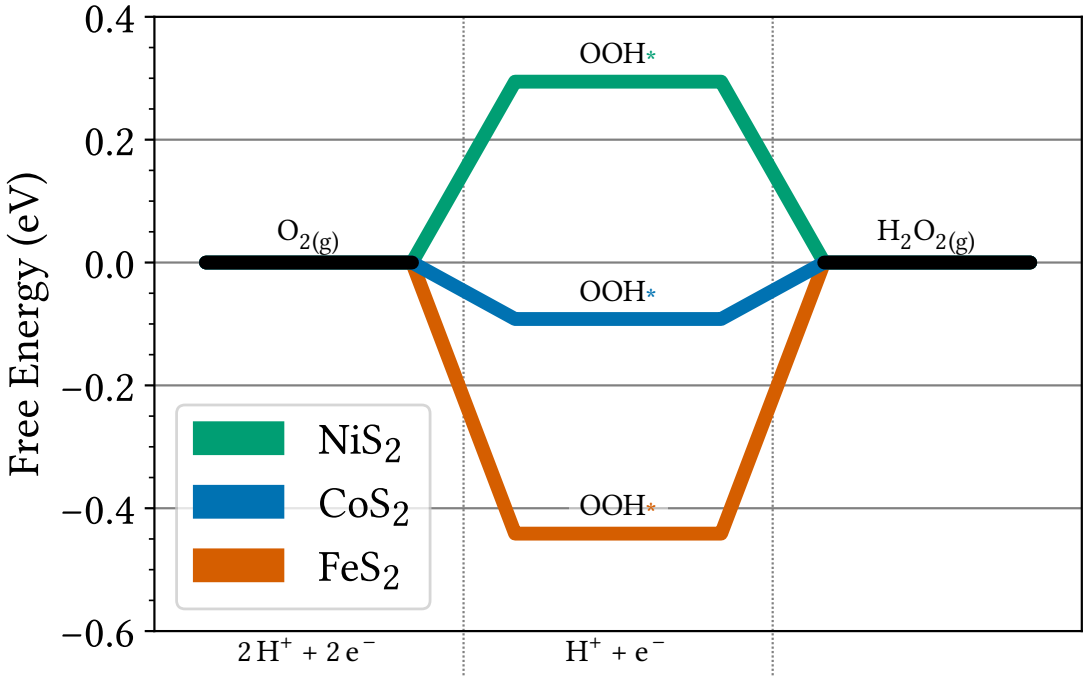

Figure 7.1: The free energy profile for the electrochemical reduction of O_2 to H_2O_2 on FeS_2, CoS_2, and NiS_2 at an applied potential of 0.66 V.

	ΔF(U = 1.23) (eV)		
Reaction	FeS_2	CoS_2	NiS_2
$O_2 + e^- + H^+ + * \longrightarrow OOH*$	0.12	0.47	0.86
$OOH* + e^- + H^+ \longrightarrow O* + H_2O$	−0.94	−0.35	0.05
$O* + e^- + H^+ \longrightarrow OH*$	0.24	−0.37	−0.68
$OH* + e^- + H^+ \longrightarrow H_2O + *$	0.58	0.25	−0.22

Table 7.2: A summary of the free energy of reaction for the electrochemical steps in the ORR formation of H_2O at the reaction potential of 1.23 V on the computational hydrogen electrode.

when all electrochemical steps in the pathway are are thermoneutral at this potential. Similarly, activity towards formation of H_2O will be maximized when all electrochemical steps in that mechanism are at thermoneutral at 1.23 V.

Table 7.1 and Figure 7.1 show the predicted free energies for the electrochemical steps

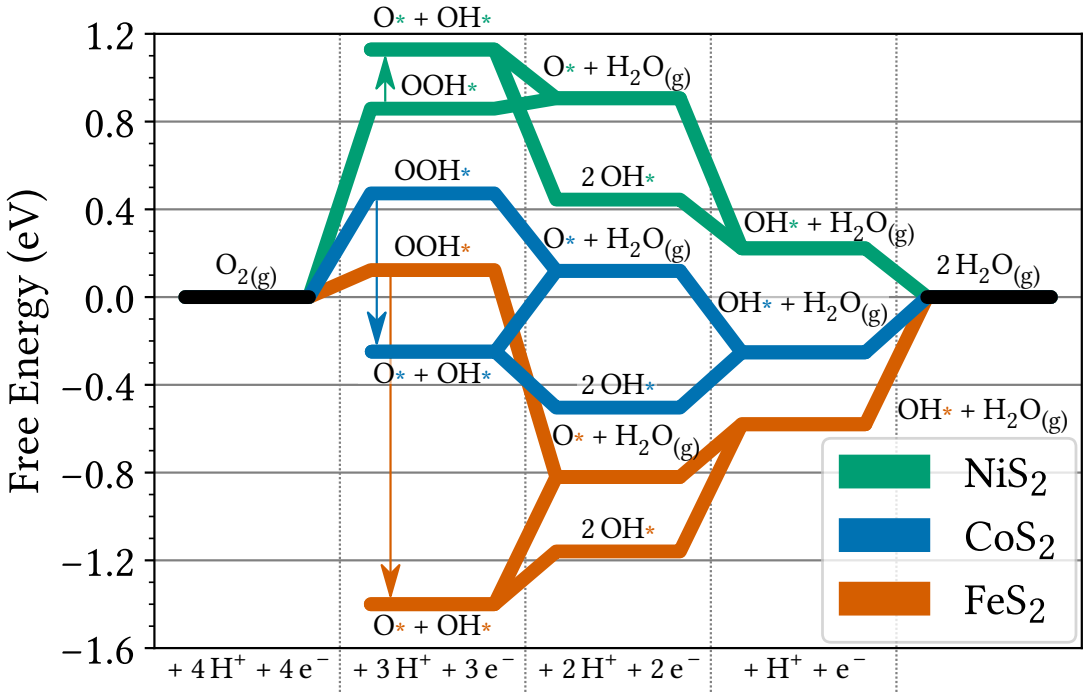

Figure 7.2: The free energy profile for the electrochemical reduction of O_2 to $2\,H_2O$ on FeS_2, CoS_2, and NiS_2 at an applied potential of 1.23 V. The vertical arrows signify non-electrochemical steps.

of the $2\,e^-$ ORR mechanism at the reaction potential of 0.66 V. We find that of the three materials, CoS_2 exhibits the most favorable thermodynamics, as its most endothermic step is only 0.09 eV uphill. In comparison, the most endothermic step of FeS_2 and NiS_2 are 0.44 eV and 0.29 eV, respectively. Based on these data alone, we would predict CoS_2 to have the highest activity for H_2O_2 synthesis among the three materials. It is worth noting that as the $2\,e^-$ pathway has only two steps, both of which are electrochemical in nature, the thermodynamics of the overall reaction is controlled entirely by the binding strength of the OOH intermediate. When OOH is bound too weakly, the initial reduction of O_2 to adsorbed OOH becomes the thermodynamically limiting step. When OOH is bound too strongly, subsequent reduction of OOH to H_2O_2 becomes thermodynamically limiting. In the latter case, the residence time of OOH on the catalyst surface will be longer, leading to eventual O–O bond cleavage and subsequent reduction to H_2O. Consequently, achieving a

proper balance of OOH binding strength is important not only for minimizing the required overpotential and improving catalyst activity, but also for improving the selectivity of the catalyst towards H_2O_2.

Table 7.2 and Figure 7.2 show the predicted free energies for the electrochemical steps of the $4\,e^-$ ORR mechanism at the reaction potential of 1.23 V. For the $4\,e^-$ mechanism, the most endothermic electrochemical step for all three materials are higher than what is observed for the $2\,e^-$ mechanism. Of the three materials, CoS_2 has the most favorable thermodynamics for the $4\,e^-$ mechanism, as it does with the $2\,e^-$ mechanism. However, the most endothermic electrochemical step of the $4\,e^-$ mechanism on CoS_2 is 0.47 eV at 1.23 V, suggesting the catalyst will have a high overpotential for this reaction. Additionally, the electrochemical step of $OOH* + H^+ + e^- \longrightarrow O* + H_2O$ involves electron transfer from the catalyst surface to the far end of adsorbed OOH (see figure 7.3). For this reaction, the intrinsic electron transfer rate will be quite low, as the transfer must either occur through-space or through multiple bonds. In comparison, the reaction $OOH* + H^+ + e^- \longrightarrow H_2O_2 + *$ must travel only through a single Co–O bond, and thus formation of H_2O_2 will be kinetically favored over the $H_2O + O*$ products, despite being less favored thermodynamically.

In addition to the purely electrochemical $4\,e^-$ reduction mechanism, it is possible for the O–O bond of adsorbed OOH to split into adsorbed O and OH. If this occurs, then the only possible final product is $2H_2O$, even if the electrochemical thermodynamics are not ideal at the overall reaction potential. Therefore, suppression of O–O bond cleavage in OOH is important for selectivity towards H_2O_2. Transition metal catalysts tend to exhibit low barriers for this reaction, as the transition state is stabilized by the ensemble of active sites present in close-packed metal surfaces. In comparison, the metal sites of pyrite structure materials are essentially isolated in the (100) surface.

Indeed, we find that the O–O bond in OOH on CoS_2 extends from its minimum energy bond length of 1.44 Å to 1.81 Å in the transition state of the O–O bond cleavage reaction. This is consistent with the observed activation energy of 0.80 eV for this reaction. For comparison, the barrier for this reaction on Pt(111) is 0.16 eV, and even on Au(111) the barrier is only 0.51 eV.[250] This difference highlights the important role of active site ensembles for bond-breaking reactions, as despite being nominally less reactive than CoS_2,

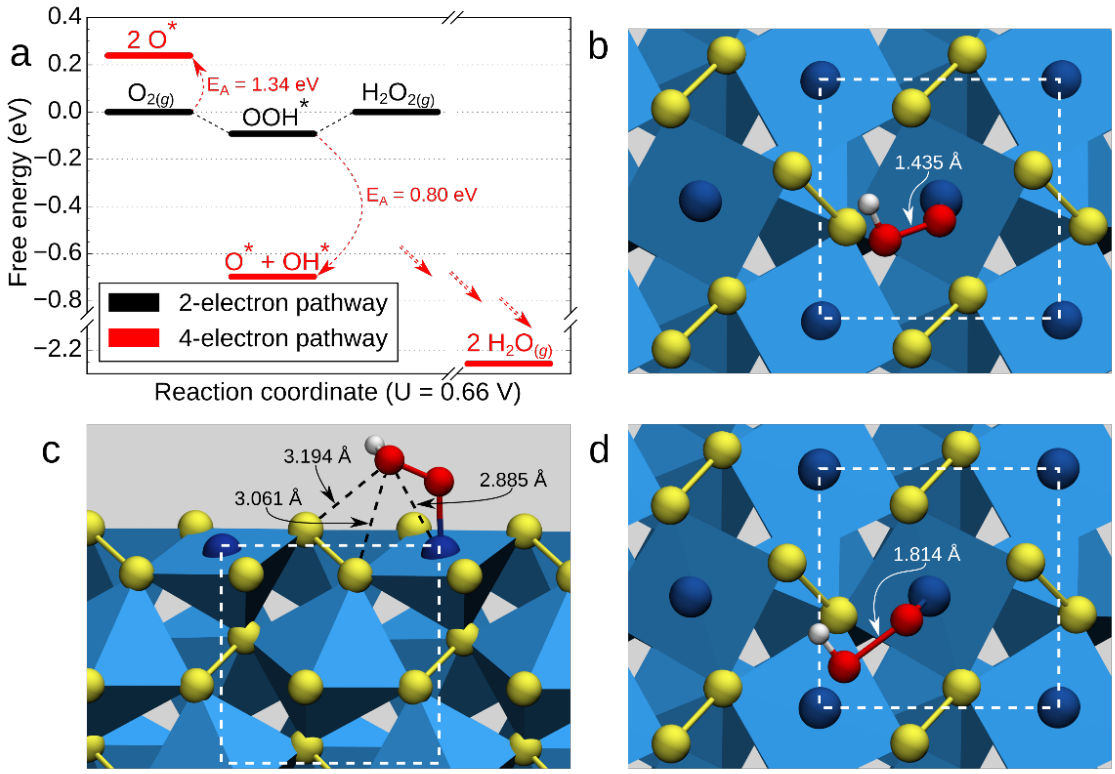

Figure 7.3: A summary of the activity of CoS_2 for the ORR. **a**, the thermodynamics of the $2\,e^-$ and $4\,e^-$ mechanisms at an applied potential of 0.66 V. Red arrows indicate steps of the $4\,e^-$ mechanism, with E_A indicating the activation energy of non-electrochemical steps. **b** top-down and **c** side-on views of the OOH intermediate adsorbed to CoS_2, with some bond and contact distances highlighted. **d**, the transition state for the reaction $OOH* + * \longrightarrow O* + OH*$, with the strained O–O bond length indicated.

gold exhibits a lower barrier for this bond-breaking reaction.

7.4 Concluding Remarks

We observe thermodynamics for formation of OOH and formation of H_2O_2 on CoS_2 that are consistent with its observed catalytic activity. In comparison, neither FeS_2 nor NiS_2 exhibit thermodynamics that are predictive of high electrocatalytic activity. Additionally,

the barrier for O–O bond cleavage in adsorbed OOH helps explain the observed selectivity for formation of H_2O_2, despite H_2O being the thermodynamically favored product. Due to its favorable binding activity and inexpensive cost, CoS_2 is a promising material for electrocatalytic applications that currently rely on expensive and less-efficient noble metal catalysts.

8 FUTURE WORK

8.1 Microkinetic modeling

In section 8.1, we outlined a technique for including adsorption and desorption of anions to a catalyst surface in a kinetic model by treating it as a capacitor. This is done by including the number of excess electrons on the catalyst as a species in the model which has strong lateral self-interactions to simulate the energetic cost of charging and discharging a capacitor. The chemical potential of the electron (see equation 3.68) has both a capacitive term which depends on the excess electron coverage and a constant term that references the energy of the electron to the vacuum. It is therefore possible to determine the working potential of the catalyst relative to the vacuum directly from the chemical potential of an electron at any point in the microkinetic model. However, we find that this simple model does not agree qualitatively with experimentally measured working catalyst potentials, and so we do not discuss these results in chapter 6.

One possible reason for this discrepancy is that the parameters used in the microkinetic model are a mixture of DFT-calculated properties and experimentally measured properties. For example, we use experimental values for the areal capacitance (C_a) and work function (Φ) of the catalyst, but the free energy of adsorption of anions is calculated entirely within DFT. The work function can be trivially calculated in DFT simulations by the difference between the average electrostatic potential far away from the catalyst surface and the Fermi level. The areal capacitance can also be predicted with DFT through the use of continuum solvent models with a self-consistent treatment of electrolyte by calculating the system energy as a function of charge. However, it is likely that this approach alone will result in quantitative agreement with experiment.

A likely more significant source of error in our approach is the lack of potential-dependent adsorbate binding energies. In reality, oxidizing species such as O and OH will adsorb more strongly to catalysts with excess negative charge, while reducing species such as H will adsorb more strongly to catalysts with excess positive charge. This can be modeled as lateral interactions between oxidizing or reducing adsorbates and the excess charge stored on the catalyst surface by extension of the capacitor model presented in

section 3.5. This is essentially equivalent to calculating the binding energy of adsorbates as a function of instantaneous working potential, and it can be included explicitly in the differential equations of the microkinetic model. Performing DFT calculations at constant electron potential rather than at a fixed number of electrons may also alleviate some of the system size dependence of the binding energies of electron-withdrawing or -donating adsorbates. However, it is not clear whether the many body expansion of the lateral interaction energy truncated at second order will be sufficient to capture the potential-dependent binding energy of adsorbates.

8.2 Micki

Currently, Micki is able to simulate batch reactor, simplified CSTR, and PFR models. A true CSTR model includes terms in the differential equations corresponding to inflow of the reactants and outflow of the reaction mixture, rather than simply fixing the concentrations of fluid species to their initial values. The feature would be rather straightforward to implement, though it has not yet been done.

Micki provides a consistent API for accessing the thermodynamic properties of fluid-phase and adsorbed species as well as the kinetic properties for a number of different types of reactions. It is designed to allow the user to create their own classes for species and reactions with different internal approximations that are compatible with the microkinetic model. This API was designed with the goal of simplifying the construction of arbitrary microkinetic models in mind, but there are possible applications beyond microkinetic modeling. For example, the user can quickly calculate the free energy of species for presentation in a tabular format without the need for complex spreadsheets or custom computer scripts.

Even within the domain of kinetic modeling, Micki has multiple potential uses. Lattice Kinetic Monte Carlo (KMC) is an alternative to microkinetic modeling which explicitly represents the catalyst as a lattice with discrete adsorption sites, each of which is unoccupied or occupied by a single species. Rather than using the mean field approximation, lattice KMC generates an ensemble of surface coverages by sampling reactions from a list of all possible reactions given the current condition of the catalyst. As this is a Monte Carlo

technique, simulations require sufficient sampling in order to calculate properties such as turnover frequency and selectivity. The only information required for KMC beyond that which is needed for microkinetic modeling is a detailed (finite) lattice structure for the catalyst and reaction information pertaining to diffusion between adsorption sites. Since lattice KMC explicitly represents the distribution of adsorbates on the lattice, it is possible to develop more complex treatments for the lateral interaction energies, such as nearest-neighbor interactions arising from steric effects or directional interactions such as hydrogen bonding.

In order to implement lattice KMC functionality, it would be necessary to develop a class for keeping track of the structure and occupation of the catalyst lattice, write routines for keeping track of all possible reactions, and write the actual KMC modeling code itself. While this is by no means trivial, the thermodynamic and reaction classes that have already been developed for microkinetic modeling could be reused in a lattice KMC code. This would also make it possible for users to directly compare the results of a mean-field microkinetic model with a discrete lattice KMC model.

8.3 Support effects

The results presented in chapter 5 provide a guide for incorporating the effects of support in computational studies of heterogeneous catalysis. From the perspective of kinetic modeling, the main difficulty with supported nanoparticles is the number of distinct binding geometries as compared to perfect crystal surfaces. In the limit of very large nanoparticles, adsorption to step edges, kinks, and the metal–support interface will become a minority of all binding.

However, these sites cannot be ignored in a kinetic model, as it is possible for reaction pathways to involve diffusion between the facets of the nanoparticle and the edges between facets or between the nanoparticle and the support. Despite this, a microkinetic model can incorporate the effect of support to first order through a simple modulation of the adsorbate binding energies according to the geometric and electronic perturbations as outlined in chapter 5. A more thorough microkinetic model would introduce additional adsorbate binding geometries as separate species in the model, and allow diffusion between

the different binding geometries. As more unique binding geometries are added, this leads to a combinatorial explosion in the number of distinct reaction pathways that can occur, which are not only difficult to manage for the scientist, but which can also lead to numerical instabilities in a microkinetic model.

While microkinetic modeling may not be well-suited for an explicit consideration of all unique reaction sites and binding geometries present in systems of supported nanoparticles, a well-designed lattice KMC approach might be more well-suited. Lattice KMC enables the scientist to create a model that explicitly accounts for the different reaction geometries and their relative physical position. A full parametrization of such a model would still require a large number of DFT calculations, such that the binding energy of each adsorbate for each unique binding site is known. However, it would be possible to use the observed trends in the binding energy shifts due to geometric and electronic perturbation by the support to predict the binding energy of adsorbates in the various available adsorption sites without the need to perform explicit DFT calculations for each combination.

8.4 Catalytic esterification of 1-propanol to methyl propionate

The motivation behind the work presented in chapter 6 was the explanation of the observed synergistic promotional effect of Bi and Te in palladium-catalyzed esterification of primary alcohols. The unpromoted Pd(111) catalyst model was the first step of the process. Work on the Bi-promoted and Te-promoted catalysts are currently in progress, with investigation of the Bi and Te doubly-promoted catalyst planned. These systems are more complex than the unpromoted system, as adsorbates can bind in many unique geometries with different energies. It is believed that Te forms a surface alloy or intermetallic state with the palladium catalyst, while Bi is present as adatoms or small clusters due it its larger size.

Based on some preliminary calculations of a model surface alloy of Te and Pd, we believe that the effect of Te can be primarily characterized as a uniform destabilization

of adsorbates and the creation of new adsorption sites on the Te atoms themselves that bind adsorbates much more weakly. From the results presented in chapter 6, we believe this could accelerate catalyst activity by lowering the steady-state concentration of H and otherwise increasing the number of catalytically active sites under steady state conditions. Work is currently in progress to calculate the binding energy of adsorbates in multiple configurations on the Te-promoted catalyst surface. We are also working to incorporate the promoted surface into our microkinetic modeling framework by considering the Pd and Te adsorption sites as distinct, and explicitly accounting for diffusion between these sites as a reaction in the model.

The Bi-promoted surface requires a slightly different treatment, as the Bi atoms behave more like coadsorbates than as alternative catalytic sites. We believe that atoms or small clusters of Bi will selectively bind to O-containing species, such as O_2 or deprotonated alcohols. This may facilitate bond-breaking or bond-making reactions involving O, such as O–O bond cleavage in O_2, deprotonation of alcohols, or abstraction of adsorbed H by alkoxides such as methoxide.

8.5 Electrocatalytic H_2O_2 synthesis on CoS_2

In chapter 7, we primarily focus on the thermodynamics of electrochemical reactions using the computational hydrogen electrode. This is because the kinetics of electron transfer reactions are difficult to predict. Marcus theory is the standard model for predicting electron transfer kinetics. However, to use Marcus theory requires knowledge of the free energy of each electronic state as a function of the nuclear reaction coordinate. This is not possible in typical DFT methods, which will relax the electron density to the lowest energy configuration for a particular configuration of atoms. Constrained DFT could potentially solve this problem by enforcing a particular electronic configuration regardless of position along the reaction coordinate. This is not a black box technique though, and this approach requires thorough validation before its accuracy can be trusted.

Chan and Nørskov developed a model for calculating electrochemical reaction barriers as a function of electrode potential on the basis of nudged elastic band calculations and Bader analysis. They argue that over a small range of potentials, the barrier for an

electrochemical reaction can be separated into chemical and electronic contributions. The chemical contribution can be obtained directly from the nudged elastic band calculation, while the electronic contribution can be predicted based on a capacitance model similar to the one presented in section 3.5. However, they only use this model to investigate a small class of reactions with only a fixed monolayer of solvent, and they did not consider reduction of adsorbates through proton-coupled electron transfer. In Marcus theory, the barrier for an electron transfer reaction arises due to fluctuations in the solvent degrees of freedom, and a single trajectory from nudged elastic band will not necessarily be representative of the true energetics of the electron transfer reaction coordinate.

Nørskov's approach is particularly troublesome due to the tendency of DFT to over-stabilize delocalized electronic configurations. For electron-transfer reactions, this will manifest as a smooth, gradual transfer of electron density from one moiety to another over the course of the reaction coordinate, instead of the sudden electron transfer that would be expected. Indeed, based on the Bader analysis presented in Chan et. al., there does seem to be a gradual transition of electron density from the surface to the evolving H_2 molecule over the course of 5 NEB images. This will result in an artificial stabilization of the transition state relative to the true electronic configuration, and consequently an overestimated reaction rate.

In addition, their approach relies on an approximation to the capacitive energy based on surface charges obtained from Bader analysis. A more rigorous way of calculating the potential-dependent reaction energetics would be to perform NEB calculations with constant-potential DFT. This would entirely remove the electronic energy contribution to the NEB results, leaving only the chemical contribution to the energy. It would also be possible to perform NEB calculations at several different potentials to see how the reaction energetics depend on potential.

It is clear that the kinetics of electron transfer reactions are difficult to accurately predict. However, with a proper treatment of electron transfer energetics, it is possible to integrate electrochemical reactions into a microkinetic model using an approach similar to what we have used for the base-catalyzed esterification of propanol, outlined in section 3.5. Rather than including the number of electrons as a variable in the differential equations, electrocatalysis would imply a fixed concentration of excess electrons, and thereby a

fixed energetic cost for electron transfer to species in solution. This would be similar to the computational hydrogen electrode approach, however it would allow for explicit consideration of the voltage-dependent binding energy of adsorbates through lateral interactions between adsorbates and the excess electron concentration. This approach would require additional development of the capacitance model, which is discussed in section 8.1. Microkinetic modeling of electrocatalysis would be a powerful tool both for mechanistic studies and to aid in the development of new better-performing electrocatalytic materials.

9 CONCLUSION

This thesis presents a summary of our work to create improved theoretical models of heterogeneous catalysis. To this end, we have explicitly constructed a framework for first principles microkinetic modeling, and developed new methodology within this framework. Using these techniques, we have investigated a variety of industrially relevant heterogeneous catalyst systems.

In chapter 3, we construct a rigorous framework for first principles microkinetic modeling based on a statistical mechanical view of the mean field lattice approximation. Within this framework, we developed a thermodynamically consistent method for incorporating lateral interactions into any microkinetic model. We further incorporated solvent and solution-phase species into the microkinetic model. In chapter 4, we describe Micki, a tool written in Python to simplify the construction and solution of first principles microkinetic models.

In chapter 5, we investigate the role of support material in the heterogeneous catalysis of supported nanoparticles. We use reaction intermediates from the Fischer–Tropsch synthesis reaction to illustrate how support can not only modulate the catalytic properties of the metal it supports, but also directly participate in catalysis through adsorbate binding at the metal–support interface. In chapter 6, we use Micki to investigate the Pd-catalyzed esterification of 1-propanol to methyl propionate as a first step in understanding the role of main group promoter elements in accelerating this reaction. In chapter 7, we explain the observed activity of CoS_2 for the oxygen reduction reaction and its selectivity towards H_2O_2 through the thermodynamics of electrochemical steps using the computational hydrogen electrode and the observed kinetic barriers to O–O bond dissociation.

The development of Micki and its use in the investigation of Pd-catalyzed 1-propanol esterification are the latest and most significant contributions presented herein. The lack of existing high-quality applications for performing microkinetic modeling is what motivated the development of Micki, and is why the other projects discussed in this work do not include microkinetic modeling. Micki will play an important role in future studies of heterogeneous catalysis in this group, and hopefully in other research groups as well.

BIBLIOGRAPHY

[1] Haber, F.; van Oordt, G. *Z. Anorg. Chem.* **1905**, *44*, 341–378.

[2] Bosch, C.; Mittasch, A. (Badische Anilin- Und Soda-Fabrik). Catalytic production of ammonia. US Patent 1225755, 1917.

[3] Smil, V. *Nature* **1999**, *400*, 415.

[4] Smil, V. *Sci. Am.* **1997**, *277*, 76–81.

[5] Smil, V. *Ambio* **2002**, *31*, 126.

[6] Erisman, J. W.; Sutton, M. A.; Galloway, J.; Klimont, Z.; Winiwarter, W. *Nat. Geosci.* **2008**, *1*, 636–639.

[7] Fischer, F.; Tropsch, H. *Brennst.-Chem.* **1926**, *7*, 97–104.

[8] Fischer, F.; Tropsch, H. Process for the production of paraffin-hydrocarbons with more than one carbon atom. US Patent 1746464, 1930.

[9] Schulz, H. *Appl. Catal., A* **1999**, *186*, 3–12.

[10] Frenkel, M. *J. Soc. Chem. Ind.* **1909**, *28*, 692–693.

[11] Cohn, J. G. *Environ. Health Perspect.* **1975**, *10*, 159–164.

[12] Bailey, A. E. *Ind. Eng. Chem.* **1951**, *44*, 990–994.

[13] Ziegler, K.; Holzkamp, E.; Breil, H.; Martin, H. *Angew. Chem.* **1955**, *67*, 541–547.

[14] Natta, G. *Angew. Chem.* **1956**, *68*, 393–403.

[15] Cornils, B.; Herrmann, W. A. *J. Catal.* **2003**, *216*, 23–31.

[16] Cole-Hamilton, D. J. *Science* **2003**, *299*, 1702–1706.

[17] van Santen, R. A.; Neurock, M. *Molecular Heterogeneous Catalysis*; WILEY-VCH Verlag: Weinheim, Germany, 2006.

[18] Krebs, B. *Fresenius' Z. Anal. Chem.* **1987**, *328*, 388–389.

[19] Furimsky, E. *Catalysis Today* **1996**, *30*, 223–286.

[20] Hansen, T. W.; Delariva, A. T.; Challa, S. R.; Datye, A. K. *Acc. Chem. Res.* **2013**, *46*, 1720–1730.

[21] Tauster, S. J.; Fung, S. C.; Garten, R. L. *J. Am. Chem. Soc.* **1978**, *100*, 170–175.

[22] Tauster, S. J. *Acc. Chem. Res.* **1987**, *20*, 389–394.

[23] Whitaker, S. *Transp. Porous Media* **1987**, *2*, 269–299.

[24] Goodman, D. W.; Kelley, R. D.; Madey, T. E.; Yates, J. T. J. *J. Catal.* **1980**, *63*, 226–234.

[25] Greenler, R. G.; Burch, K. D.; Kretzschmar, K.; Klauser, R.; Bradshaw, A. M.; Hayden, B. E. *Surf. Sci.* **1985**, *152-153*, 338–345.

[26] Berlowitz, P. J.; Peden, C. H. F.; Goodman, D. W. *J. Phys. Chem.* **1988**, *92*, 5213–5221.

[27] Lee, M. B.; Yang, Q. Y.; Ceyer, S. T. *J. Chem. Phys.* **1987**, *87*, 2724–2741.

[28] Dellwig, T.; Hartmann, J.; Libuda, J.; Meusel, I.; Rupprechter, G.; Unterhalt, H.; Freund, H.-J. *J. Mol. Catal. A: Chem.* **2000**, *162*, 51.

[29] Andersson, M. P.; Bligaard, T.; Kustov, A.; Larsen, K. E.; Greeley, J.; Johannessen, T.; Christensen, C. H.; Nørskov, J. K. *J. Catal.* **2006**, *239*, 501–506.

[30] Greeley, J.; Jaramillo, T. F.; Bonde, J.; Chorkendorff, I.; Nørskov, J. K. *Nat. Mater.* **2006**, *5*, 909–913.

[31] Greeley, J.; Nørskov, J. K. *Surf. Sci.* **2007**, *601*, 1590–1598.

[32] Nørskov, J. K.; Bligaard, T.; Rossmeisl, J.; Christensen, C. H. *Nat. Chem.* **2009**, *1*, 37–46.

[33] Loffreda, D.; Delbecq, F.; Vigné, F.; Sautet, P. *Angew. Chem., Int. Ed.* **2009**, *48*, 8978–8980.

[34] Nørskov, J. K.; Abild-Pedersen, F.; Studt, F.; Bligaard, T. *Proc. Natl. Acad. Sci.* **2011**, *108*, 937–943.

[35] Sabbe, M. K.; Reyniers, M.-F.; Reuter, K. *Catal. Sci. Technol.* **2012**, *2*, 2010.

[36] Broadbelt, L. J.; Snurr, R. Q. *Appl. Catal., A* **2000**, *200*, 23–46.

[37] Ovesen, C. V.; Clausen, B. S.; Schiøtz, J.; Stoltze, P.; Topsøe, H.; Nørskov, J. K. *J. Catal.* **1997**, *168*, 133–142.

[38] Nørskov, J. K.; Bligaard, T.; Hvolbæk, B.; Abild-Pedersen, F.; Chorkendorff, I.; Christensen, C. H. *Chem. Soc. Rev.* **2008**, *37*, 2163.

[39] Molenbroek, A. M.; Helveg, S.; Topsøe, H.; Clausen, B. S. *Top. Catal.* **2009**, *52*, 1303–1311.

[40] Hibbitts, D. D.; Neurock, M. *J. Catal.* **2013**, *299*, 261–271.

[41] Behtash, S.; Lu, J.; Walker, E.; Mamun, O.; Heyden, A. *J. Catal.* **2016**, *333*, 171–183.

[42] Faheem, M.; Saleheen, M.; Lu, J.; Heyden, A. *Catal. Sci. Technol.* **2016**, *6*, 8242–8256.

[43] Sprowl, L. H.; Campbell, C. T.; Árnadóttir, L. *J. Phys. Chem. C* **2016**, acs.jpcc.5b11616.

[44] Campbell, C. T.; Sprowl, L. H.; Árnadóttir, L. *J. Phys. Chem. C* **2016**, acs.jpcc.5b11616.

[45] Jørgensen, M.; Grönbeck, H. *J. Phys. Chem. C* **2017**,

[46] Kunz, L.; Kuhn, F. M.; Deutschmann, O. *J. Chem. Phys.* **2015**, *143*, 044108.

[47] Liu, D.-J.; Zahariev, F.; Gordon, M. S.; Evans, J. W. *J. Phys. Chem. C* **2016**, *120*, 28639–28653.

[48] Pineda, M.; Stamatakis, M. *J. Chem. Phys.* **2017**, *147*, 024105.

[49] Alecu, I. M.; Zheng, J.; Papajak, E.; Yu, T.; Truhlar, D. G. *J. Phys. Chem. A* **2012**, *116*, 12206–12213.

[50] Kohn, W.; Sham, L. J. *Phys. Rev.* **1965**, *140*.

[51] Hohenberg, P.; Kohn, W. *Phys. Rev. B* **1964**, *136*, 864–871.

[52] Moruzzi, V. L.; Janak, J. F.; Schwarz, K. *Phys. Rev. B* **1988**, *37*, 790–799.

[53] Duffy, P.; Chong, D. P.; Dupuis, M. *J. Chem. Phys.* **1995**, *102*, 3312–3321.

[54] Perdew, J. P.; Yue, W. *Phys. Rev. B* **1986**, *33*, 8800–8802.

[55] Tao, J.; Perdew, J. P.; Staroverov, V. N.; Scuseria, G. E. *Phys. Rev. Lett.* **2003**, *91*, 146401.

[56] Gill, P. M. W.; Johnson, B. G.; Pople, J. A.; Frisch, M. J. *Int. J. Quantum Chem., Symp.* **1992**, *26*, 319–331.

[57] Dion, M.; Rydberg, H.; Schröder, E.; Langreth, D. C.; Lundqvist, B. I. *Phys. Rev. Lett.* **2004**, *92*, 22–25.

[58] Klimeš, J.; Bowler, D. R.; Michaelides, A. *Phys. Rev. B* **2011**, *83*, 1–13.

[59] Grimme, S. *J. Comput. Chem.* **2006**, *16*, 1787–1799.

[60] Tonigold, K.; Groß, A. *J. Chem. Phys.* **2010**, *132*, 224701.

[61] Perdew, J. P.; Burke, K.; Ernzerhof, M. *Phys. Rev. Lett.* **1996**, *77*, 3865–3868.

[62] Perdew, J. P.; Burke, K.; Ernzerhof, M. *Phys. Rev. Lett.* **1997**, *78*, 1396.

[63] Grimme, S.; Antony, J.; Ehrlich, S.; Krieg, H. *J. Chem. Phys.* **2010**, *132*, 154104.

[64] Grimme, S.; Ehrlich, S.; Goerigk, L. *J. Comput. Chem.* **2011**, 1456–1465.

[65] Reckien, W.; Janetzko, F.; Peintinger, M. F.; Bredow, T. *J. Comput. Chem.* **2012**, *33*, 2023–31.

[66] Heyd, J.; Scuseria, G. E. *J. Chem. Phys.* **2004**, *121*, 1187–1192.

[67] Heyd, J.; Peralta, J. E.; Scuseria, G. E.; Martin, R. L. *J. Chem. Phys.* **2005**, *123*, 174101.

[68] Heyd, J.; Scuseria, G. E.; Ernzerhof, M. *J. Chem. Phys.* **2006**, *124*, 219906.

[69] Krukau, A. V.; Vydrov, O. A.; Izmaylov, A. F.; Scuseria, G. E. *J. Chem. Phys.* **2006**, *125*, 224106.

[70] Moellmann, J.; Grimme, S. *J. Phys. Chem. C* **2014**, *118*, 7615–7621.

[71] Larsen, A. H.; Mortensen, J. J.; Blomqvist, J.; Castelli, I. E.; Christensen, R.; Dułak, M.; Friis, J.; Groves, M. N.; Hammer, B.; Hargus, C.; Hermes, E. D.; Jennings, P. C.; Jensen, P. B.; Kermode, J.; Kitchin, J. R.; Kolsbjerg, E. L.; Kubal, J.; Kaasbjerg, K.; Lysgaard, S.; Maronsson, J. B.; Maxson, T.; Olsen, T.; Pastewka, L.; Peterson, A.; Rostgaard, C.; Schiøtz, J.; Schütt, O.; Strange, M.; Thygesen, K.; Vegge, T.; Vilhelmsen, L.; Walter, M.; Zeng, Z.; Jacobsen, K. W. *J. Phys.: Condens. Matter* **2017**, *29*, 273002.

[72] Dumesic, J. A.; Rudd, D. F.; Aparicio, L. M.; Rekoske, J. E.; Treviño, A. L. *The Microkinetics of Heterogeneous Catalysis*; American Chemical Society: Salem, MA, 1993.

[73] Zhdanov, V. P.; Kasemo, B. *Phys. Rev. B* **1997**, *55*, 4105–4108.

[74] Bondi, A. *J. Phys. Chem.* **1964**, *68*, 441–451.

[75] Hansen, H. A.; Viswanathan, V.; Nørskov, J. K. *J. Phys. Chem. C* **2014**, *118*, 6706–6718.

[76] Medford, A. J.; Shi, C.; Hoffmann, M. J.; Lausche, A. C.; Fitzgibbon, S. R.; Bligaard, T.; Nørskov, J. K. *Catal. Lett.* **2015**, *145*, 794–807.

[77] Grabow, L. C.; Gokhale, A. A.; Evans, S. T.; Dumesic, J. A.; Mavrikakis, M. *J. Phys. Chem. C* **2008**, *112*, 4608–4617.

[78] Campbell, C. T. *Top. Catal.* **1994**, *1*, 353–366.

[79] Stegelmann, C.; Andreasen, A.; Campbell, C. T. *J. Am. Chem. Soc.* **2009**, *131*, 8077–8082.

[80] Campbell, C. T. *ACS Catal.* **2017**, *7*, 2770–2779.

[81] Hermes, E. D.; Jenness, G. R.; Schmidt, J. *Mol. Simul.* **2015**, *41*, 123–133.

[82] Campbell, C. T. *Nat. Chem.* **2012**, *4*, 597–598.

[83] Pacchioni, G. *Phys. Chem. Chem. Phys.* **2013**, *15*, 1737–1757.

[84] Metiu, H.; Chrétien, S.; Hu, Z.; Li, B.; Sun, X. *J. Phys. Chem. C* **2012**, *116*, 10439–10450.

[85] Cárdenas-Lizana, F.; Hao, Y.; Crespo-Quesada, M.; Yuranov, I.; Wang, X.; Keane, M. A.; Kiwi-Minsker, L. *ACS Catal.* **2013**, *3*, 1386–1396.

[86] Wörz, A. S.; Heiz, U.; Cinquini, F.; Pacchioni, G. *J. Phys. Chem. B* **2005**, *109*, 18418–18426.

[87] Carrasco, J.; Barrio, L.; Liu, P.; Rodriguez, J. A.; Ganduglia-Pirovano, M. V. *J. Phys. Chem. C* **2013**, *117*, 8241–8250.

[88] Mpourmpakis, G.; Vlachos, D. G. *J. Phys. Chem. C* **2009**, *113*, 7329–7335.

[89] Jung, J.; Shin, H.-J.; Kim, Y.; Kawai, M. *J. Am. Chem. Soc.* **2012**, *134*, 10554–10561.

[90] Kim, H. Y.; Lee, H. M.; Henkelman, G. *J. Am. Chem. Soc.* **2011**, *134*, 1560–1570.

[91] Larichev, Y. V.; Moroz, B. L.; Bukhtiyarov, V. I. *Appl. Surf. Sci.* **2011**, *258*, 1541–1550.

[92] Linsmeier, C.; Taglauer, E. *Appl. Catal., A* **2011**, *391*, 175–186.

[93] Talo, A.; Lahtinen, J.; Hautojärvi, P. *Appl. Catal., B* **1995**, *5*, 221–231.

[94] Labich, S.; Taglauer, E.; Knözinger, H. *Top. Catal.* **2000**, *14*, 153–161.

[95] Óvári, L.; Kiss, J. *Appl. Surf. Sci.* **2006**, *252*, 8624–8629.

[96] Kitchin, J. R.; Nørskov, J. K.; Barteau, M. A.; Chen, J. G. *J. Chem. Phys.* **2004**, *120*, 10240–10246.

[97] Kitchin, J. R.; Nørskov, J. K.; Barteau, M. A.; Chen, J. G. *Phys. Rev. Lett.* **2004**, *93*, 156801.

[98] Hayek, K.; Kramer, R.; Paál, Z. *Appl. Catal., A* **1997**, *162*, 1–15.

[99] Green, I. X.; Tang, W.; Neurock, M.; Yates, J. T. *Science* **2011**, *333*, 736–739.

[100] Green, I. X.; Tang, W.; Neurock, M.; Yates, J. T. *Faraday Discuss.* **2013**, *162*, 247–265.

[101] Kaden, W. E.; Kunkel, W. A.; Roberts, F. S.; Kane, M.; Anderson, S. L. *J. Chem. Phys.* **2012**, *136*, 204705.

[102] Kaden, W. E.; Kunkel, W. A.; Kane, M. D.; Roberts, F. S.; Anderson, S. L. *J. Am. Chem. Soc.* **2010**, *132*, 13097–13099.

[103] Fischer, F.; Tropsch, H. *Brennstoff-Chem.* **1930**, *11*, 489.

[104] Jenness, G. R.; Schmidt, J. R. *ACS Catal.* **2013**, *3*, 2881–2890.

[105] Beyer, H.; Emmerich, J.; Chatziapostolou, K.; Köhler, K. *Appl. Catal., A* **2011**, *391*, 411–416.

[106] Ligthart, D. A. J. M.; van Santen, R. A.; Hensen, E. J. M. *J. Catal.* **2011**, *280*, 206–220.

[107] Wang, Z.-J.; Yang, F.; Axnanda, S.; Liu, C.-J.; Goodman, D. W. *Appl. Catal., A* **2011**, *391*, 342–349.

[108] Gao, J.; Mo, X.; Chien, A. C.-Y.; Torres, W.; Goodwin Jr., J. G. *J. Catal.* **2009**, *262*, 119–126.

[109] Mo, X.; Gao, J.; Goodwin Jr., J. G. *Catal. Today* **2009**, *147*, 139–149.

[110] Mo, X.; Gao, J.; Umnajkaseam, N.; Goodwin Jr., J. G. *J. Catal.* **2009**, *267*, 167–176.

[111] Savastenko, N.; Volpp, H.-R.; Gerlach, O.; Strehlau, W. *J. Nanoparticle Res.* **2008**, *10*, 277–287.

[112] Ito, S.-i.; Chibana, C.; Nagashima, K.; Kameoka, S.; Tomishige, K.; Kunimori, K. *Appl. Catal., A* **2002**, *236*, 113–120.

[113] Barthe, L.; Hemati, M.; Philippot, K.; Chaudret, B.; Denicourt-Nowicki, A.; Roucoux, A. *Chem. Eng. J.* **2009**, *151*, 372–379.

[114] Wang, L.; Weller, C. L.; Jones, D. D.; Hanna, M. A. *Biomass and Bioenergy* **2008**, *32*, 573–581.

[115] Mei, D.; Rousseau, R.; Kathmann, S. M.; Glezakou, V.-A.; Engelhard, M. H.; Jiang, W.; Wang, C.; Gerber, M. A.; White, J. F.; Stevens, D. J. *J. Catal.* **2010**, *271*, 325–342.

[116] Liu, Y.; Murata, K.; Inaba, M.; Takahara, I.; Okabe, K. *Catal. Today* **2011**, *164*, 308–314.

[117] Gogate, M. R.; Davis, R. J. *ChemCatChem* **2009**, *1*, 295–303.

[118] Subramanian, N. D.; Gao, J.; Mo, X.; Goodwin Jr., J. G.; Torres, W.; Spivey, J. J. *J. Catal.* **2010**, *272*, 204–209.

[119] Gao, J.; Mo, X.; Goodwin Jr., J. G. *J. Catal.* **2009**, *268*, 142–149.

[120] Schwartz, V.; Campos, A.; Egbebi, A.; Spivey, J. J.; Overbury, S. H. *ACS Catal.* **2011**, *1*, 1298–1306.

[121] Haider, M.; Gogate, M.; Davis, R. *J. Catal.* **2009**, *261*, 9–16.

[122] Egbebi, A.; Schwartz, V.; Overbury, S. H.; Spivey, J. J. *Catal. Today* **2010**, *149*, 91–97.

[123] Gogate, M. R.; Davis, R. J. *Catal. Commun.* **2010**, *11*, 901–906.

[124] Boffa, A.; Bell, A. T.; Somorojai, G. A. *J. Catal.* **1994**, *149*, 149–158.

[125] Dalai, A. K.; Davis, B. H. *Appl. Catal., A* **2008**, *348*, 1–15.

[126] Yan, Z.; Bukur, D. B.; Goodman, D. W. *Catal. Today* **2011**, *160*, 39–43.

[127] Wang, J.; Zhang, Q.; Wang, Y. *Catal. Today* **2011**, *171*, 257–265.

[128] Li, P.; Liu, J.; Nag, N.; Crozier, P. A. *Surf. Sci.* **2006**, *600*, 693–702.

[129] Somorjai, G. A.; Aliaga, C. *Langmuir* **2010**, *26*, 16190–16203.

[130] van Santen, R. A.; Neurock, M.; Shetty, S. G. *Chem. Rev.* **2009**, *110*, 2005–2048.

[131] van Santen, R. A. *Acc. Chem. Res.* **2008**, *42*, 57–66.

[132] Beale, A. M.; Weckhuysen, B. M. *Phys. Chem. Chem. Phys.* **2010**, *12*, 5562–5574.

[133] Logan, A. D.; Braunschweig, E. J.; Datye, A. K.; Smith, D. J. *Langmuir* **1988**, *4*, 827–830.

[134] Murashov, V. V.; Demchuk, E. *Surf. Sci.* **2005**, *595*, 6–19.

[135] Goumans, T. P. M.; Wander, A.; Brown, W. A.; Catlow, C. R. A. *Phys. Chem. Chem. Phys.* **2007**, *9*, 2146–2152.

[136] Rignanese, G.-M.; De Vita, A.; Charlier, J.-C.; Gonze, X.; Car, R. *Phys. Rev. B* **2000**, *61*, 13250–13255.

[137] Chuang, S. S. C.; Stevens Jr., R. W.; Khatri, R. *Top. Catal.* **2005**, *32*, 225–232.

[138] Sneh, O.; George, S. M. *J. Phys. Chem.* **1995**, *99*, 4639–4647.

[139] Michalske, T. A.; Freiman, S. W. *Nature* **1982**, *295*, 511–512.

[140] Diebold, U. *Surf. Sci. Rep.* **2003**, *48*, 53–229.

[141] Kunat, M.; Burghaus, U.; Woll, C. *Phys. Chem. Chem. Phys.* **2004**, *6*, 4203–4207.

[142] Menetrey, M.; Markovits, A.; Minot, C. *Surf. Sci.* **2003**, *524*, 49–62.

[143] Suda, Y.; Morimoto, T. *Langmuir* **1987**, *3*, 786–788.

[144] Prins, R. *Chem. Rev.* **2012**, *112*, 2714–2738.

[145] Haller, G. L.; Resasco, D. E. In *Metal–Support Interaction: Group VIII Metals and Reducible Oxides*; Eley, D., Pines, H., Weisz, P. B., Eds.; Advances in Catalysis Supplement C; Academic Press, 1989; Vol. 36; pp 173 – 235.

[146] Finazzi, E.; Di Valentin, C.; Pacchioni, G.; Selloni, A. *J. Chem. Phys.* **2008**, *129*, 154113.

[147] Bahn, S. R.; Jacobsen, K. W. *Comput. Sci. Eng.* **2002**, 56–66.

[148] Kresse, G.; Hafner, J. *Phys. Rev. B* **1993**, *47*, 558–561.

[149] Kresse, G.; Hafner, J. *Phys. Rev. B* **1994**, *49*, 14251–14269.

[150] Kresse, G.; Furthmüller, J. *Phys. Rev. B* **1996**, *54*, 11169–11186.

[151] Kresse, G.; Furthmüller, J. *Comput. Mater. Sci.* **1996**, *6*, 15–50.

[152] Perdew, J. P.; Burke, K.; Ernzerhof, M. *Phys. Rev. Lett.* **1996**, *77*, 3865–3868.

[153] Perdew, J. P.; Burke, K.; Ernzerhof, M. *Phys. Rev. Lett.* **1997**, *78*, 1396.

[154] Blöchl, P. E. *Phys. Rev. B* **1994**, *50*, 17953–17979.

[155] Kresse, G.; Joubert, D. *Phys. Rev. B* **1999**, *59*, 1758–1775.

[156] Bitzek, E.; Koskinen, P.; Gähler, F.; Moseler, M.; Gumbsch, P. *Phys. Rev. Lett.* **2006**, *97*, 170201.

[157] Sheppard, D.; Terrell, R.; Henkelman, G. *J. Chem. Phys.* **2008**, *128*, 134106.

[158] Dudarev, S. L.; Botton, G. A.; Savrasov, S. Y.; Humphreys, C. J.; Sutton, A. P. *Phys. Rev. B* **1998**, *57*, 1505–1509.

[159] Hu, Z.; Metiu, H. *J. Phys. Chem. C* **2011**, *115*, 5841–5845.

[160] Bader, R. F. W. *Atoms in Molecules: A Quantum Theory*; International series of monographs on chemistry; Clarendon Press, 1990.

[161] Grant, A.; Campbell, C. *Phys. Rev. B* **1997**, *55*, 1844–1851.

[162] Chua, Y. G.; Gunasooriya, G. K. K.; Saeys, M.; Seebauer, E. G. *J. Catal.* **2014**, *311*, 306–313.

[163] Green, I. X.; Tang, W.; Neurock, M.; Yates, J. T. *Acc. Chem. Res.* **2013**, *47*, 805–815.

[164] Zhang, S.-T.; Li, C.-M.; Yan, H.; Wei, M.; Evans, D. G.; Duan, X. **2014**, *2*.

[165] Hermes, E. D.; Janes, A. N.; Schmidt, J. *ACS Catal.* **2018**, *8*, 272–282.

[166] Sheldon, R. *Metal-Catalyzed Oxidations of Organic Compounds: Mechanistic Principles and Synthetic Methodology Including Biochemical Processes*; Elsevier Science, 2012.

[167] Vinod, C. P.; Wilson, K.; Lee, A. F. *J. Chem. Technol. Biotechnol.* **2011**, *86*, 161–171.

[168] Parmeggiani, C.; Cardona, F. *Green Chem.* **2012**, *14*, 547.

[169] Mallat, T.; Baiker, A. *Chem. Rev.* **2004**, *104*, 3037–3058.

[170] Sheldon, R. A.; Arends, I.; Dijksman, A. *Catal. Today* **2000**, *57*, 157–166.

[171] Fiege, H.; Wedemeyer, K. *Angew. Chem.* **1981**, *93*, 812–813.

[172] Mallat, T.; Bodnar, Z.; Baiker, A. *Stud. Surf. Sci. Catal.* **1993**, *78*, 377–384.

[173] Mallat, T.; Bodnar, Z.; Baiker, A.; Greis, O.; Strübig, H.; Reller, A. *J. Catal.* **1993**, *142*, 237–253.

[174] Mannel, D. S.; Ahmed, M. S.; Root, T. W.; Stahl, S. S. *J. Am. Chem. Soc.* **2017**, *139*, 1690–1698.

[175] Mallat, T.; Baiker, A. *Catal. Today* **1994**, *19*, 247–284.

[176] Furuya, N.; Motoo, S. *J. Electroanal. Chem.* **1979**, *98*, 195–202.

[177] Smits, P. C. C.; Kuster, B. F. M.; van der Wiele, K.; van der Baan, S. *Appl. Catal.* **1987**, *33*, 83–96.

[178] Parsons, R.; VanderNoot, T. *J. Electroanal. Chem. Interfacial Electrochem.* **1988**, *257*, 9–45.

[179] Tsujino, T.; Ohigashi, S.; Sugiyama, S.; Kawashiro, K.; Hayashi, H. *J. Mol. Catal.* **1992**, *71*, 25–35.

[180] Kimura, H.; Tsuto, K.; Wakisaka, T.; Kazumi, Y.; Inaya, Y. *Appl. Catal., A* **1993**, *96*, 217–228.

[181] Mallat, T.; Bodnar, Z.; Baiker, A. *ACS Symp. Ser.* **1993**, *523*, 308–317.

[182] Horányi, G.; Vértes, G.; König, P. *Acta Chim. Acad. Sci. Hung.* **1972**, *72*, 179–187.

[183] Dirkx, J. M. H.; van der Baan, H. S.; van den Broek, J. M. A. J. J. *Carbohydr. Res.* **1977**, *59*, 63–72.

[184] Dirkx, J. M. H.; van der Baan, H. S. *J. Catal.* **1981**, *67*, 14–20.

[185] Dijkgraaf, P. J. M.; Duisters, H. A. M.; Kuster, B. F. M.; van der Wiele, K. *J. Catal.* **1988**, *112*, 337–344.

[186] Nicoletti, J. W.; Whitesides, G. M. *J. Phys. Chem.* **1989**, *93*, 759–767.

[187] Grunwaldt, J.-D.; Caravati, M.; Baiker, A. *J. Phys. Chem. B* **2006**, *110*, 25586–25589.

[188] Hoffman, A.; Kuhn, A. T. *Electrochim. Acta* **1964**, *9*, 835–839.

[189] Dijkgraaf, P. J. M.; Rijk, M. J. M.; Meuldijk, J.; van der Wiele, K. *J. Catal.* **1988**, *112*, 329–336.

[190] Dijkgraaf, P. J. M. Oxidation of Glucose to Glucaric Acid by Pt/C Catalysts. Ph.D. thesis, Technische Universiteit Eindhoven, 1989.

[191] Vinke, P.; de Wit, D.; de Goede, A. T. J. W.; van Bekkum, H. *Stud. Surf. Sci. Catal.* **1992**, *72*, 1–20.

[192] DiCosimo, R.; Whitesides, G. *J. Phys. Chem.* **1989**, *93*, 768–775.

[193] Schuurman, Y.; Kuster, B.; van der Wiele, K.; Marin, G. *Stud. Surf. Sci. Catal.* **1992**, *72*, 43–55.

[194] Vassilyev, Y. B.; Khazova, O. A.; Nikolaeva, N. N. *J. Electroanal. Chem.* **1985**, *196*, 127–144.

[195] Popović, K. D.; Marković, N. M.; Tripković, A. V.; Adžić, R. R. *J. Electroanal. Chem.* **1991**, *313*, 181–199.

[196] Adkins, H.; Broderick, A. E. *J. Am. Chem. Soc.* **1928**, *50*, 499–503.

[197] Lauder, I. *Trans. Faraday Soc.* **1948**, *44*, 729–735.

[198] McKenna, F. E.; Tartar, H. V.; Lingafelter, E. C. *J. Am. Chem. Soc.* **1953**, *75*, 604–607.

[199] Powell, A. B.; Stahl, S. S. *Org. Lett.* **2013**, *15*, 5072–5075.

[200] Kresse, G.; Hafner, J. *Phys. Rev. B* **1993**, *47*, 558–561.

[201] Kresse, G.; Hafner, J. *Phys. Rev. B* **1994**, *49*, 14251–14269.

[202] Kresse, G.; Furthmüller, J. *Phys. Rev. B* **1996**, *54*, 11169–11186.

[203] Heyden, A.; Bell, A. T.; Keil, F. J. *J. Chem. Phys.* **2005**, *123*, 224101.

[204] Izmaylov, A. F.; Scuseria, G. E.; Frisch, M. J. *J. Chem. Phys.* **2006**, *125*, 0–8.

[205] Gil, A.; Clotet, A.; Ricart, J. M.; Kresse, G.; García-Hernández, M.; Rösch, N.; Sautet, P. *Surf. Sci.* **2003**, *530*, 71–86.

[206] Zeng, Z.; Greeley, J. *Catal. Commun.* **2014**, *52*, 78–83.

[207] Zhao, Z. J.; Li, Z.; Cui, Y.; Zhu, H.; Schneider, W. F.; Delgass, W. N.; Ribeiro, F.; Greeley, J. *J. Catal.* **2017**, *345*, 157–169.

[208] Gale, W.; Totemeier, T. *Smithells Metals Reference Book*; Elsevier Science, 2003.

[209] Monkhorst, H. J.; Pack, J. D. *Phys. Rev. B* **1976**, *13*, 5188–5192.

[210] Gunceler, D.; Letchworth-Weaver, K.; Sundararaman, R.; Schwarz, K. A.; Arias, T. A. *Modell. Simul. Mater. Sci. Eng.* **2013**, *21*, 074005.

[211] Mathew, K.; Sundararaman, R.; Letchworth-Weaver, K.; Arias, T. A.; Hennig, R. G. *J. Chem. Phys.* **2014**, *140*.

[212] Mathew, K.; Hennig, R. G. Implicit self-consistent description of electrolyte in plane-wave density-functional theory. 2016; http://arxiv.org/abs/1601.03346, arXiv:1601.03346. arXiv.org e-Print archive.

[213] Jónsson, H.; Mills, G.; Jacobsen, K. W. In *Classical and Quantum Dynamics in Condensed Phase Simulations*; Berne, B. J., Ciccotti, G., Coker, D. F., Eds.; World Scientific, 1998; Chapter 16, pp 385–404.

[214] Henkelman, G.; Jónsson, H. *J. Chem. Phys.* **2000**, *113*, 9978–9985.

[215] Henkelman, G.; Jónsson, H. *J. Chem. Phys.* **1999**, *111*, 7010.

[216] Kästner, J.; Sherwood, P. *J. Chem. Phys.* **2008**, *128*, 014106.

[217] Frisch, M. J.; Trucks, G. W.; Schlegel, H. B.; Scuseria, G. E.; Robb, M. A.; Cheeseman, J. R.; Scalmani, G.; Barone, V.; Mennucci, B.; Petersson, G. A.; Nakatsuji, H.; Caricato, M.; Li, X.; Hratchian, H. P.; Izmaylov, A. F.; Bloino, J.; Zheng, G.; Sonnenberg, J. L.; Hada, M.; Ehara, M.; Toyota, K.; Fukuda, R.; Hasegawa, J.; Ishida, M.; Nakajima, T.; Honda, Y.; Kitao, O.; Nakai, H.; Vreven, T.; Montgomery Jr., J. A.; Peralta, J. E.; Ogliaro, F.; Bearpark, M.; Heyd, J. J.; Brothers, E.; Kudin, K. N.; Staroverov, V. N.; Keith, T.; Kobayashi, R.; Normand, J.; Raghavachari, K.; Rendell, A.; Burant, J. C.; Iyengar, S. S.; Tomasi, J.; Cossi, M.; Rega, N.; Millam, J. M.; Klene, M.; Knox, J. E.; Cross, J. B.; Bakken, V.; Adamo, C.; Jaramillo, J.; Gomperts, R.; Stratmann, R. E.; Yazyev, O.; Austin, A. J.; Cammi, R.; Pomelli, C.; Ochterski, J. W.; Martin, R. L.; Morokuma, K.; Zakrzewski, V. G.; Voth, G. A.; Salvador, P.; Dannenberg, J. J.; Dapprich, S.; Daniels, A. D.; Farkas, O.; Foresman, J. B.; Ortiz, J. V.; Cioslowski, J.; Fox, D. J. Gaussian~09 Revision D.01. Gaussian Inc. Wallingford CT 2016.

[218] Dunning Jr, T. H. *J. Chem. Phys.* **1989**, *90*, 1007.

[219] Marenich, A. V.; Cramer, C. J.; Truhlar, D. G. *J. Phys. Chem. B* **2009**, *113*, 6378–6396.

[220] Hermes, E. D.; Janes, A. N.; Schmidt, J. R. unpublished work.

[221] Fang, L.-l.; Tao, Q.; Li, M.-f.; Liao, L.-w.; Chen, D.; Chen, Y.-x. *Chin. J. Chem. Phys.* **2010**, *23*, 543.

[222] Silbaugh, T. L.; Campbell, C. T. *J. Phys. Chem. C* **2016**, 25161–25172.

[223] Yeager, E. *Electrochim. Acta* **1984**, *29*, 1527–1537.

[224] Acres, G. J. K.; Frost, J. C.; Hards, G. A.; Potter, R. J.; Ralph, T. R.; Thompsett, D.; Burstein, G. T.; Hutchings, G. J. *Catal. Today* **1997**, *38*, 393–400.

[225] Mukerjee, S.; Srinivasan, S. *J. Electroanal. Chem.* **1993**, *357*, 201–224.

[226] Liang, Y.; Li, Y.; Wang, H.; Zhou, J.; Wang, J.; Regier, T.; Dai, H. *Nat. Mater.* **2011**, *10*, 780–786.

[227] Wu, G.; More, K. L.; Johnston, C. M.; Zelenay, P. *Science* **2011**, *332*, 443–447.

[228] Kosaka, K.; Yamada, H.; Shishida, K.; Echigo, S.; Minear, R. A.; Tsuno, H.; Matsui, S. *Water Res.* **2001**, *35*, 3587–3594.

[229] Chidambara Raj, C. B.; Quen, L. H. *Chem. Eng. Sci.* **2005**, *60*, 5305–5311.

[230] Campos-Martin, J. M.; Blanco-Brieva, G.; Fierro, J. L. *Angew. Chem., Int. Ed.* **2006**, *45*, 6962–6984.

[231] Riedl, H.-J.; Pfleiderer, G. (Ludwigshafen-on-the-Rhine). Production of Hydrogen Peroxide. US Patent 2158525, 1939.

[232] Zhang, J.; Vukmirovic, M. B.; Sasaki, K.; Nilekar, A. U.; Mavrikakis, M.; Adzic, R. R. *J. Am. Chem. Soc.* **2005**, *127*, 12480–12481.

[233] Stamenkovic, V.; Mun, B. S.; Mayrhofer, K. J.; Ross, P. N.; Markovic, N. M.; Rossmeisl, J.; Greeley, J.; Nørskov, J. K. *Angew. Chem.* **2006**, *118*, 2963–2967.

[234] Greeley, J.; Nørskov, J. K.; Kibler, L. A.; El-Aziz, A. M.; Kolb, D. M. *ChemPhysChem* **2006**, *7*, 1032–1035.

[235] Strmcnik, D.; Kodama, K.; Van Der Vliet, D.; Greeley, J.; Stamenkovic, V. R.; Marković, N. M. *Nat. Chem.* **2009**, *1*, 466–472.

[236] Greeley, J.; Stephens, I. E. L.; Bondarenko, A. S.; Johansson, T. P.; Hansen, H. A.; Jaramillo, T. F.; Rossmeisl, J.; Chorkendorff, I.; Nørskov, J. K. *Nat. Chem.* **2009**, *1*, 552–556.

[237] Santos, E.; Lundin, A.; Pötting, K.; Quaino, P.; Schmickler, W. *Phys. Rev. B* **2009**, *79*, 1–10.

[238] Keith, J. A.; Jacob, T. *Angew. Chem., Int. Ed.* **2010**, *49*, 9521–9525.

[239] Nørskov, J. K.; Rossmeisl, J.; Logadottir, A.; Lindqvist, L.; Kitchin, J. R.; Bligaard, T.; Jónsson, H. *J. Phys. Chem. B* **2004**, *108*, 17886–17892.

[240] Letchworth-Weaver, K.; Arias, T. A. *Phys. Rev. B* **2012**, *86*, 1–16.

[241] Chan, K.; Nørskov, J. K. *J. Phys. Chem. Lett.* **2015**, 2663–2668.

[242] Chan, K.; Nørskov, J. K. *J. Phys. Chem. Lett.* **2016**, *1690*, 1686–1690.

[243] Ping, Y.; Nielsen, R. J.; Goddard, W. A. *J. Am. Chem. Soc.* **2017**, *139*, 149–155.

[244] Sundararaman, R.; Goddard, W. A.; Arias, T. A. *J. Chem. Phys.* **2017**, *146*, 114104.

[245] Siahrostami, S.; Verdaguer-Casadevall, A.; Karamad, M.; Deiana, D.; Malacrida, P.; Wickman, B.; Escudero-Escribano, M.; Paoli, E. a.; Frydendal, R.; Hansen, T. W.; Chorkendorff, I.; Stephens, I. E. L. S.; Stephens, I. E. L. S.; Rossmeisl, J. *Nat. Mater.* **2013**, *12*, 1137–43.

[246] Zhu, L.; Susac, D.; Teo, M.; Wong, K. C.; Wong, P. C.; Parsons, R. R.; Bizzotto, D.; Mitchell, K. A.; Campbell, S. A. *J. Catal.* **2008**, *258*, 235–242.

[247] Faber, M. S.; Lukowski, M. A.; Ding, Q.; Kaiser, N. S.; Jin, S. *J. Phys. Chem. C* **2014**, *118*, 21347–21356.

[248] Faber, M. S.; Dziedzic, R.; Lukowski, M. A.; Kaiser, N. S.; Ding, Q.; Jin, S. *J. Am. Chem. Soc.* **2014**, *136*, 10053–10061.

[249] Jirkovský, J. S.; Björling, A.; Ahlberg, E. *J. Phys. Chem. C* **2012**, *116*, 24436–24444.

[250] Ford, D. C.; Nilekar, A. U.; Xu, Y.; Mavrikakis, M. *Surf. Sci.* **2010**, *604*, 1565–1575.